

Development of a Five Degree-of-Freedom Robot for the Manipulation of Biological Cells

by

Kelly D. R. Sakaki

T.E.T, Northern Alberta Institute of Technology, 2001
B.Eng., University of Victoria, 2005

A Thesis Submitted in Partial Fulfillment of the
Requirements for the Degree of

Master of Applied Science

in the Department of Mechanical Engineering

© Kelly D. R. Sakaki, 2007

University of Victoria

All rights reserved. This thesis may not be reproduced in whole or in part by photocopy or other means, without the permission of the author.

Development of a Five Degree-of-Freedom Robot for the Manipulation of Biological Cells

by

Kelly D. R. Sakaki

T.E.T., Northern Alberta Institute of Technology, 2001
B.Eng., University of Victoria, 2005

Supervisory Committee

Dr. E. J. Park, Supervisor (Department of Mechanical Engineering)

Dr. N. Dechev, Supervisor (Department of Mechanical Engineering)

Dr. R. D. Burke, Outside Member (Departments of Biology and Biochemistry/Microbiology)

Dr. T. Fyles, External Examiner (Department of Chemistry)

Supervisory Committee

Dr. E. J. Park, Supervisor (Department of Mechanical Engineering)

Dr. N. Dechev, Supervisor (Department of Mechanical Engineering)

Dr. R. D. Burke, Outside Member (Departments of Biology and Biochemistry/Microbiology)

Dr. T. Fyles, External Examiner (Department of Chemistry)

Abstract

Studies of individual cells via microscopy and microinjection are a key component in research on gene functions, cancer, stem cells, and reproductive technology. As biomedical experiments become more complex, there is an urgent need for robotic systems to: improve cell manipulation, increase throughput, reduce lost cells, and improve reaction detection. Automation of these tasks using visual servoing creates significant benefits for biomedical laboratories including repeatability of experiments, higher throughput, and a controlled environment capable of operating 24 hours a day. In this work the design and development of a new five degree-of-freedom biomanipulator designed for single-cell microinjection, is described. The biomanipulator employs three degrees of linear motion and two degrees of rotation. This provides the ability to manipulate/micro-inject cells at varying orientations, thereby increasing flexibility in dealing with complex operations such as injecting clustered cells. The capability of the biomanipulator is shown with preliminary experimental results using mouse myeloma cells.

Table of Contents

Supervisory Committee	ii
Abstract	iii
Table of Contents	iv
List of Tables	vii
List of Figures	viii
Nomenclature	x
Acknowledgements	xi
1 Introduction	1
1.1 Research Background and Objectives	1
1.2 The State-of-the-Art	6
1.2.1 Motion Control and Devices	7
1.2.2 Optics	8
1.2.3 Microinjection Devices	9
1.2.4 Current Biomanipulation Devices	10
1.3 Present Work and Contributions	13
1.4 Outline of Thesis	14
2 System and Methodology Overview	16
2.1 Proposed Biomanipulator System and Methodology	16
2.2 Overview of the Automated Tasks	17
2.2.1 Localization and Segmentation	17
2.2.2 Tracking	19
2.2.3 Single-cell Electroporation	19
2.3 Biomanipulator Subsystems	21
2.3.1 Mechanical Subsystem	21
2.3.2 Optical Train and Vision Subsystem	22
2.3.3 Control Subsystem: Visual Servoing of Biological Cells	22
2.3.4 Injection Subsystem: Single-cell Electroporation	24

3	Design Procedure	25
3.1	Background	25
3.2	Operational and Design Requirements	26
3.3	Configuration of System Axes	27
3.4	Optical Assembly	29
3.4.1	Phase Contrast Illumination	32
3.4.2	Hoffman Modulation Contrast	34
3.4.3	Differential Interference Contrast	34
3.4.4	Comparison of Phase Contrast, DIC, and HMC	35
3.4.5	Digital Sensors	37
3.4.6	Optical Component Selection and Validation	39
3.5	Electro-Mechanical Assembly	41
3.5.1	Mechanical Stage Selection	41
3.6	Cantilever Beam	43
3.6.1	Computer-Aided Modeling of Cantilever Beam	44
3.7	Motor Controller Sub-assembly	49
3.8	Summary	51
4	Electroporation	52
4.1	Overview	52
4.1.1	Electroporation Theory	53
4.2	Single-cell Electroporation	55
4.2.1	Applied use of the Single-cell Electroporator	58
5	Biomanipulator Control	62
5.1	Biomanipulator Control Problem Definition	62
5.2	Image Based Control: Visual Servoing	62
5.3	Camera Model	64
5.4	Control Method Error Function	67
5.5	Computer Vision	68
5.5.1	Problem Realization	68
5.5.2	Background Information	69
5.5.3	Localization Methods Used	70
5.5.4	Binary Shape Detection	70
5.5.5	Greyscale Template Matching	72
5.5.6	Segmentation	74
5.5.7	Autofocusing	77
5.5.8	Summary	78
6	Results	79
6.1	Overview	79
6.2	Mechanical Design	79
6.3	Computer Vision	80
6.3.1	Localization using Canny and LOG Algorithms	80
6.3.2	Segmentation	89

Table of Contents	vi
6.4 Single-cell Electroporation	89
7 Conclusions	95
8 Future Research Proposed	99

List of Tables

3.1	Microscope Specifications	40
3.2	Digital Camera	40
3.3	Cantilever Beam Design Limitations	43
3.4	Dimension Values for Cantilever Beam	48
3.5	Cantilever Constraints and Optimized Values	49
3.6	Specifications of the Biomanipulator Cantilever Beam	49
4.1	Settings for the Sutter P-87™ Automated Pipette Puller	59
5.1	Guassian Kernel	71
5.2	Laplacian Kernel	72
5.3	Sobel Horizontal Gradient Kernel	75
5.4	Sobel Vertical Gradient Kernel	75
6.1	Settings for Bulk Electroporation	90

List of Figures

2.1	Image of the biomanipulator assembly	17
2.2	Biomanipulator task sequence: starting position	18
2.3	Biomanipulator task sequence: cell localization	18
2.4	Biomanipulator task sequence: injection preparation	19
2.5	SCE Routine: motion of cell with respect to the micropipette tip. . .	20
2.6	Biomanipulator task sequence: cell indentation by micropipette . . .	21
2.7	Biomanipulator task sequence: SCE	22
3.1	Operational flow chart	26
3.2	Conceptual representation of the proposed biomanipulator	27
3.3	Conceptual representation of the proposed biomanipulator	28
3.4	Depth-of-field	32
3.5	ALS1000 cantilevered load capability	44
3.6	CAD model of the biomanipulator.	45
3.7	CAD model of biomanipulator: front clearance	46
3.8	C channel dimensions	47
3.9	Obstruction zones for cantilever beam	47
3.10	CAD solid model used for FEM analysis	48
3.11	Final cantilever assembly	49
3.12	Cantilever beam assembly	50
4.1	Electroporator voltage clamp circuit	57
4.2	Voltage divider created between the SCE electrodes	58
4.3	Axon Axoporator 800A™ single-cell electroporator	59
4.4	Micropipette Side View	60
4.5	Comparison between micropipette	60
5.1	Algorithms for binary shape recognition	71
5.2	DIC image of mouse myeloma prior to the Hough transform	76
5.3	DIC Image of mouse myeloma after the Hough transform	77
5.4	Simulated Mouse Myeloma and the Hough Transform	77
6.1	Image of a cell cluster	81
6.2	Thresholding problems	82
6.3	LOG algorithm: cells localized per image	83
6.4	Canny algorithm: cells localized per image	83
6.5	Cell viability in images	84

6.6	Adhered spherical cell	85
6.7	Greyscale mouse myeloma template image	86
6.8	Normal distributions of all cells located by greyscale template matching	87
6.9	Healthy cells identified within image using a high threshold	87
6.10	Cells identified within image using low threshold	88
6.11	Bulk electroporation of mouse myeloma cells	91
6.12	Bulk electroporation viewed by the biomanipulator	92
8.1	Successful SCE of mouse myeloma cells using Alexa Fluor 568 TM	100

Nomenclature

Acronyms

CAD	Computer Aided Design
SCE	Single-cell electroporation
DOF	Degrees-of-freedom
DIC	Differential interference contrast
MEMS	Micro-electromechanical systems
HMC	Hoffman-modulation contrast
CCD	Charge-coupled device
ROI	Region-of-interest
DC	Direct current
API	Application programming interface
VI	Visual interface
MOS	Metal-oxide semiconductors
CMOS	Complimentary Metal Oxide Semiconductor
CAD	Computer aided design
PBS	Phosphate buffered saline
PBVS	Position-based visual servo
IBVS	Image-based visual servo
DIBLM	Dynamic image-based look-and-move structure
FEM	Finite Element Model
SCM	Single Cell Micromanipulation

Acknowledgements

Words on paper cannot alone express my gratitude to my supervisors Dr. Edward Park and Dr. Nick Dechev, for providing me with the opportunity to be involved in such a fascinating project. It truly has opened up a new path in my life and has provided me with a new inspiration and focus for my technical background, creative abilities, and fascination with the life sciences.

I also express infinite thanks to Dr. Robert Burke and Dr. Diana Wang for providing expert advice in cell biology and biochemistry, and for providing the mouse myeloma and other essential ingredients for the operation and analysis of the biomaniipulator. Furthermore, I would also like express thanks to Dr. Robert Burke and Dr. Kerry Delaney for the use of their facilities and delicate equipment.

Finally, this large undertaking would not have been possible without the support, love, friendship, and devotion of my best friend and fiancé Sarah Cameron.

Chapter 1

Introduction

1.1 Research Background and Objectives

Biomedical laboratories are injecting biological cells with exogenous (*i.e.* foreign, *etc.*) molecules more routinely than ever before. Various means of inserting these molecules are currently available, but at the same time, biomedical experiments are becoming increasingly complex. Presently, routine experiments involving the biomanipulation of thousands of cells can be extremely labour intensive and require highly trained technicians. Furthermore, processing rare cells using batch processing and rapid techniques of biomanipulation are not suitable due to low throughput and poor yield.

Single-cell micromanipulation (SCM) via microscopy and microinjection is a key component in research on stem cells, transgenics, cancer and reproductive technology. State-of-the-art technology is available to optically image single cells, the processes occurring inside, and to move micron-sized end-effectors with nano-scale resolution. However, biomanipulation tasks such as microinjection still rely on manual capturing and positioning of a cell, followed by manual microinjection of molecules such as DNA, RNA, dyes, and proteins. Consequently, the success rates of these manual processes are usually low due to the high variability that accompanies a manual process. Another disadvantage of conventional single-cell microinjection is that the operator is required to pierce the cell membrane with a thin and fragile glass micropipette

causing temporary or irreparable damage to the cell wall which often leads to the cell's destruction.

Clearly, there exists a need for more efficient and precise methods of micromanipulation for the advancement of research in cell biology and biochemistry, and for higher throughput of routine laboratory experiments in single-cell analysis. It is the author's belief that a fully automated solution is able to supersede the abilities of human operators by performing highly-repeatable, high-throughput experiments. Currently, low-level devices assisting human operators exist for single-cell injection and are commercially available, but a fully automated solution does not exist. Using state-of-the-art technology, a fully automated solution is realizable using high-resolution motors, microscopes for biological specimens, and modern single-cell injection devices. It is the author's intention to develop a biomanipulator for the localized microinjection of cells. This will be accomplished by combining these modern devices with current image processing algorithms and control theory based on interpreting dynamic information in images known as visual servoing.

A biomanipulator that is capable of manipulating biological specimens requires sufficient resolution to be able to maneuver within a micron-scale environment. The cells used in this work are mouse myeloma cells, which are approximately spherical and between 10 μm and 20 μm in diameter. This size is consistent with many other mammalian cells, and will serve as a suitable starting point before attempting irregular shaped or rare cells. Cells of this physical scale require high-resolution positioning of the robotic manipulator. In order to manipulate mammalian sized cells, a resolution far less than the overall diameter of a mammalian cell is required. For example, a motor with a resolution of 2 μm moving a micropipette tip to a point next to a cell with a diameter of 20 μm will provide only 10 possible positions of placement over a length comparable to the size of the cell. Therefore the resolution of motion must be relatively small to allow the ability to selectively and smoothly

place an object near a 20 μm mammalian cell. Not only is the resolution important, but so are the motion characteristics of the electro-mechanical machine responsible for moving the system. In this work, direct-drive linear motors were selected since they have better performance than standard motors. Minimizing vibrations and unwanted deflection of the biomanipulator requires consistency throughout the entire design. This is achieved through careful component selection such as a vibration isolation table, and through component design using finite-element modelling (FEM) for mobile components. In particular, the biomanipulator implemented in this work required a cantilever beam supporting a Petri-dish over a microscope objective and extensive use of FEM was performed to ensure adequate rigidity was maintained.

The minimum mobility of biomanipulation devices to perform tasks such as microinjection typically requires a minimum of 2 DOF to move an end-effector to a cell, and 1 DOF to bring the specimen and end-effector into focus. A new, flexible biomanipulator configuration, developed in this work, is achieved by moving a platform holding the Petri-dish relative to the image-sensor using three linear axes. Keeping the end-effector (a micropipette tip) calibrated and in focus with the image sensor, the design is simplified since it eliminates the need to provide additional electro-mechanical resources to bring the micropipette tip into focus. Furthermore, biomanipulation tasks are not restricted to one field of view only. Scanning an entire Petri dish of cells is achievable using this configuration. Additionally, this configuration of the biomanipulator provides two rotation axes capable of changing the orientation of the cells, and adjusting the injection angle of the micropipette tip.

The optical system necessary to image thin, transparent cells and high resolution motion requires sufficient optical resolution. Achieving high resolution and high contrast images of cells is required to facilitate more accurate computer image processing. In addition, special optics are required to see these thin, and nearly transparent cells. Differential interference contrast (DIC) is widely used to provide high-contrast images

of thin, transparent biological specimens, and has a small depth of field providing a thin cross-section of the image for computer vision analysis. The optics in this work use DIC, situated on an inverted microscope. This inverted configuration is better suited for biomanipulation tasks, and provides more room to manipulate cells.

To facilitate a general purpose mode of delivery of foreign material into cells, a method known as single-cell electroporation (SCE) [1] [2] [3] is implemented with the biomanipulator. This method of molecular delivery is an adaptation of a more conventional method for mass cell injection that is widely used by both industrial and academic laboratories. The term bulk-electroporation will be used to differentiate between SCE and large scale electroporation. Bulk electroporation is deemed a non-contact method of microinjection. It involves placing many cells in a small container known as a cuvette. The cuvette also contains the desired foreign material to permeate the cell membrane. Once the cells are immersed in the foreign material, the cuvette is placed between two electrodes, and electric field pulses on the order of kilo-Volts are applied for a short duration. The electric field causes temporary openings in the cell membrane allowing the foreign material to permeate the cell membrane. A short period of time after the electric field is turned off, the openings in the cell membrane close, thereby trapping the foreign material inside the cell. The cells are then washed and placed in fresh medium, and a trained operator determines which cells have been successfully electroporated. Unfortunately, the success rate of this bulk electroporation is low.

SCE offers the same benefits as bulk electroporation, but more importantly, operates on a much smaller scale than bulk-electroporation. SCE allows for localized analysis during electroporation, and reduces the voltage required for a successful electroporation from kilo-Volts to tens-of-Volts [4]. In addition to these benefits, SCE has no toxic effect on cells from the use of the electrode and microcapillary combination [5]. SCE works as follows: first the microcapillary tip is placed against the cell

membrane. Upon applying an electric potential to an electrode, contained within the glass micropipette, temporary openings are created in the cell membrane allowing the exogenous material to enter the cell by electrophoresis and electro-osmosis. SCE does not require the cell membrane to be mechanically pierced, which may reduce the chances of rupturing the cell membrane. The benefits of SCE over conventional methods including *(i)* a less invasive method of injection, *(ii)* a reduced consumption of expensive reagents or DNA, and *(iii)* a lower electroporation voltage that is applied locally [4].

Incorporating computer vision into automated systems for visual feedback has many advantages. It can increase the efficiency and flexibility far beyond what can be achieved from regular motor encoders. Previously developed systems with integrated computer vision suffered due to slow processors and slow image sensors, potentially leading to unstable systems. New advances in processor-architecture has increased the speed and quality of image sensor (camera) technology. The increase in performance makes it possible to use computationally intensive techniques such as visual servoing. Visual servoing, in this work, will allow a computer to control the relative motion between an end-effector and a cell, and adjust for change that may occur during the motion. This work takes advantage of one of the four types of visual servoing, as classified by [6] [7], known as dynamic image-based look-and-move structure (DIBLM). DIBLM eliminates error in kinematic calibration by utilizing image processed feature data. Furthermore, DIBLM exploits the benefits of modern motion controllers by allowing simple velocity based commands to be passed through a commercial interface.

The goal of this work is to develop an automated robotic biomanipulator using SCE as the method of microinjection of exogenous material. The following objectives are defined:

1. Design and implement a mechanical system capable of accurately placing a

- micropipette tip near a cell membrane with minimal mechanical disturbances.
2. Develop a 5 DOF biomanipulator capable of moving the cells in the three orthogonal directions \hat{x} , \hat{y} , and \hat{z} , change cell orientation about the $\hat{\alpha}$ axis, and modify the injection angle of the micropipette tip about the $\hat{\beta}$ axis.
 3. Design and implement an optical system capable of imaging thin, nearly transparent, spherical mammalian cells of approximately 10 μm to 20 μm in diameter.
 4. Develop a vision-based control algorithm to automate the integrated mechanical and optical system, which is capable of identifying a target and moving an end-effector to that target using closed-loop control.
 5. Design and implement an injection sub-system capable of injecting foreign material into cells by single-cell electroporation (SCE).

1.2 The State-of-the-Art

Biomanipulation requires several key areas in technology such as photonics (digital imagery and microscopy), computer vision, motion control, and injection mechanisms. Capturing images of biological specimens requires special optical techniques to resolve thin, nearly transparent specimens. The image provided by the microscope optics must be transferred to an image sensor (camera) adequate resolution to discern details. The image sensor must also provide a fast enough frame rate to avoid bottlenecks in data processing. Furthermore, in order to provide accurate motion from observed changes, a suitable image processing technique is required combined with sufficient accuracy in motion control.

Presently, there exists various biomanipulation technologies from purely human operated biomanipulation devices, to partially automated biomanipulators. These include: human teleoperated end-effectors, haptic devices providing force feedback

during biomanipulation, and semi-automated biomanipulators ranging from micro-capillary microinjection biomanipulators to integrated microfluidic biomanipulators.

This section provides an overview of these areas in technology that have been integrated into industrial and research biomanipulators.

1.2.1 Motion Control and Devices

Previous biomanipulator designs are composed of either commercially available or custom designed components. Details such as equipment specifications used in the design on previous work are not always specified. In 2001, [8] used a 2 DOF piezo actuator with 10 nm resolution for capillary microinjection of oocytes. A 3 DOF Narishige Micromanipulator was also used for large movements with a dSPACE™ DS1102 interface. In 2002, [9] used a Sutter MP-285™ micromanipulator with a precision worm-gear providing 40 nm resolution (manufacturer specification). The end-effector was a custom lasso used to loop protein of less than 100 μm . Also in 2002, [10] used a 3 DOF micromanipulator with 40 nm resolution for capillary microinjection of mouse embryo. In 2004, [11] used a linear motor and a rotation stepper motor to position a capillary microinjection pipette and force sensor with respect to a fish embryo. The manual translation stage on a Meiji microscope was also used to assist with positioning. In 2005, [12] used a 3 DOF piezoelectric micromanipulator to position the pressurized capillary microinjection of human breast cancer cells. Reference [13], in 2006, used an enhanced single-cell electroporator to inject bovine aortic endothelial cells. The end-effector was positioned by a Sutter MP-286™ micromanipulator and NI LabVIEW was used to provide an interface for an operator. In this work, a 3 DOF, direct-drive, linear motor assembly provide 40 nm resolution (manufacturer specified), backlash free motion. Two precision worm-drive rotation stages provide angular motion.

1.2.2 Optics

Resolving detail in biological specimens often requires special optical techniques. Conventional brightfield illumination relies on differences in reflected light. When used for imaging the thin, nearly transparent biological cells such as mouse myeloma, brightfield illumination provides poor contrast. For this reason several specialized methods including phase contrast, Hoffman modulation contrast (HMC), and differential interference contrast (DIC) have evolved and are used in daily practice in both industry and research. The evolution of these illumination methods has further motivated researchers to find methods of digitally post-processing the captured image. A significant, but far from exhaustive amount of research has been completed over the last two decades in image processing techniques. This is likely due to recent developments over the last two decades in both processor speed and improved fabrication techniques of image sensors and integrated technology.

Recently, there has been considerable investigation in methods of analysing differential interference contrast images of biological cells. DIC provides high contrast images at the expense of what appears to be a shadow being cast over the observed specimen. This shadow-effect is known as an optical artifact. Reference [14] developed a method for localizing and segmenting yeast cells using template matching using DIC microscopy. Reference [15] improved on this work by developing a high-level, Bayesian statistical approach when encountering clustering or overlapping groups of cells. In an attempt to overcome the directional, shadow-like appearance of DIC images, [16] used a variance filter as well as shear-directional integration. Reference [17] used the Hilbert transform to pre-process DIC images for 3D visualization of chromosomes from orchid roots. A comparison of brightfield, DIC, and phase-contrast illumination was done using autofocusing algorithms [18]. HMC provides a similar, but slightly less flexible illumination compared to to DIC (further discussed in Section 3.4). HMC was used to segment zona pellucida in human embryos [19].

Phase contrast is another popular method of viewing biological specimens. Its performance, similar to DIC, is degraded by an optical artifact. In phase contrast, a bright halo can be seen surrounding some areas of the illuminated specimen. The halo reduces the abilities of localization and segmentation algorithms by causing false edges to be detected. Relevant research includes the development of a computer vision algorithm that automatically detected cells in phase contrast images and then normalized the image with respect to the background intensity followed by background subtraction [20]. Phase contrast was also used in tracking migrating breast carcinoma, astrocytoma, melanoma [21] as well as endothelial cells [21] [22].

Post-processing these images requires a digital image sensor to capture the transmitted light modified by the biological specimen. Two types of image sensors available are: charged coupled device (CCD) sensors and complimentary metal oxide semiconductor (CMOS) sensors. CCD image sensors presently dominate the market. After examining previous literature in biomanipulation devices, it was found that many researchers developing biomanipulators who listed the type of image sensor, from 2001 to the present, only listed the use of a CCD digital image sensor [9] [10] [11] [13]. The author was unable to locate any sources claiming to use CMOS sensors for biomanipulation of cells. This is likely due to two reasons: the higher sensitivity of CCD image sensors compared to CMOS image sensors, as well as the novelty of CMOS sensors.

1.2.3 Microinjection Devices

Introduction of foreign molecules or DNA into cells can be accomplished using various methods. SCE as described in Section 1.1, is one method that provides localized delivery through electroporation. Manual microinjection by micropipette is a conventional method still widely used for delivery, and was used as the primary method for delivery in automated biomanipulation [10] and semi-automated biomanipulation [12]. This involves inserting a micropipette tip through the cell membrane; however

requires highly-skilled technicians and frequently results in rupturing the cell membrane. Another method for introduction of molecules, developed in the 70's [23], to deliver foreign material uses viral vectors. Viral vectors have specialized molecular mechanisms for transporation into another cell. They essentially infect a cell and the DNA within the viral vector is transferred to the infected cell. Another device known as a gene gun, developed by [24], attaches recombinant DNA to micron size tungsten, gold, or silver spheres. These spheres are then propelled at a very high velocity into cells at which point the foreign DNA is integrated into the cells that haven't been destroyed. The gene gun was originally designed to transfer DNA to other plant cells, but has since been used for animal tissue [25].

1.2.4 Current Biomanipulation Devices

In literature and industry, the following two research areas are of direct relevance to our work: *(i)* single-cell micro-manipulation, and *(ii)* single-cell visual servoing. Single-cell micro-manipulation refers to methods of manipulating the physical characteristics of cells such as location, intra-cellular contents, and manipulation of cell systems. Visual servoing is a term that first appeared in published works by [26]. Visual servoing involves capturing an image of the desired scene. Within the image, the orientation or position of objects are identified with respect to the camera. These orientations or positions are then compared to the desired orientation or position of either the robot or end-effector within the scene. This difference between the desired position and current position are compared to generate signals, which result in a command to the mechanical system to reduce this error term to zero. This routine continues until the resulting error between the desired and current position of either the robot or end-effector becomes zero.

The intention of this thesis is to develop an autonomous robot that utilizes single-cell visual servoing for the purposes of performing single-cell micro-manipulation. Present devices, using similar technology and similar intentions, used for bioma-

nipulation tasks such as microinjection can be divided into three areas including (i) operator driven, mechanical systems, (ii) haptic devices which provide force-feedback or a sense of touch to the operator within the working environment, and (iii) systems with varying degrees of automation. Significant research has been completed in visual servoing and a thorough literature review and tutorial was completed by [27], whose nomenclature and terminology is adopted and used by the author in this thesis.

Typical human operated mechanical systems for biomanipulation, with two or three degrees-of-freedom are widely available on the market. Some examples include the InjectMan™ and PatchMan™ by Eppendorf used for microinjection and electrophysiology, and the piezoelectric PM-20™ by myNeuroLab. Systems such as these include a microscope and possibly a digital camera for easy viewing plus a mechanical stage that may be motorized or stationary. The end-effector, which carries the main instrument for applications such as microinjection, is typically mounted to motorized stages that provide multi-degrees of freedom. An operator observes the cells and micropipette by watching the computer monitor display or observing the cells through an analog port. The operator will typically use a joystick to control the motion of the micropipette and a hand-dial to control the location of the microscope stage. These systems require the skills of a highly trained operator, and the tasks tend to be laborious and fatiguing due to eye-strain and long periods of high operator concentration.

Haptic biomanipulator devices, allow an operator to gain a perception of how a robot end-effector is physically interacting with an object. Haptic technology combines mechanical precision, resolution, and force-feedback with the flexible skill-set of a human operator, and was investigated by several research organizations. Recently, [28] developed a system that recreates a three-dimensional, visual representation of a cell for more accurate positioning of the end-effector and also provides force-feedback to stabilize the operator's end-effector velocity while piercing the cell membrane.

Other researchers have created similar devices primarily using force-feedback to increase the accuracy of the microinjection and to reduce damage to the cell membrane [11] [29].

Researchers are aggressively pursuing the goal of creating a fully autonomous manipulator capable of providing repeatable, continuous, and accurate results in the field of single-cell manipulation without the aid of an operator other than for logistical replenishment of reagents and target cells. Presently, tools such as operator controlled, multi-degree-of-freedom manipulators and sub-micron resolution microscopes are widely available for academic and industrial use. However, a fully integrated system that combines such precision tools for automating microinjection does not exist. Several devices achieved success in biomanipulation tasks with various amounts of operator intervention. Reference [30] developed a robot for microinjection of cells, and provides force-feedback to an operator while a microinjection pipette achieves contact with the cell membrane. Another example demonstrating the use of visual servoing is a robot implemented by [9] which uses visual servoing techniques to position a micro-loop to manipulate protein crystals that are 100 μm in size. Similarly, [12] developed an operator assisted, three DOF, capillary-pressure microinjection robot for adhered cells which uses an impedance-based measurement system used to detect the presence of a cell or detect faulty micropipette conditions. Reference [8] developed an operator controlled micromanipulator that optimizes the mechanical motion of the insertion of a micropipette into oocytes. Both [8] and [10] developed a system that autonomously identifies the nucleus of a pre-selected mouse embryo and performs a microinjection using computer vision. Recently, [13] created a semi-automated tool for cell microinjection by single-cell electroporation. In their device, using a computer mouse, an operator first identifies the location of the micropipette tip and the desired destination point above a cell. The micropipette tip is then commanded to move in a predefined path and the resistance between the micropipette tip and the

cell membrane is measured. The micropipette tip is then slowly moved further toward the cell center, indenting the cell membrane and thereby reducing the voltage requirement for electroporation. At the resistance level where injection by single-cell electroporation can be achieved the cell is automatically electroporated (injected) with foreign material.

A competing technology, with a similar goal of microinjection, are devices combining micro-fluidics and microelectromechanical structures (MEMS), which use fluid to move the cell to a location or compartment that will perform the injection. Exogenous material is often delivered to the cell by either single-cell electroporation or batch or bulk electroporation. Reference [31] passed cells through a micro-fluidic channel and applied an electric field to all cells inside the channel. A more localized version was developed by [32], which passes cells through a micro-fluidic channel to a monitoring point that measures the change in impedance due to the cell passing through two electrodes. The cell size is estimated using lookup tables from previous tests, and then an operator initiates the electroporation. A similar device, created by [33], uses a micro-fluidic channel to queue the cells toward a micro-hole suction port, to trap a cell temporarily at which time single-cell electroporation occurs.

1.3 Present Work and Contributions

The current methods and devices outlined in Section 1.2 describe many methods of micromanipulation and microinjection, as well as several works supporting the growth of automating the biomanipulation of cells. The goal of this work is to create an autonomous multi-degree of freedom robot which will provide an efficient, repeatable, less invasive technique of injecting exogenous materials into cells. Intended academic contributions include:

- The implementation of a novel 5 DOF robot capable of the visual servoing of mammalian cells, and microinjection of cells less than 20 μm by electroporation,

- Localization and segmentation techniques of mouse myeloma cells,
- Single-cell electroporation parameter acquisition.

Previous systems developed, outlined in Section 1.3, provide varying degrees of automation; however, a fully automated solution has yet to be developed. The proposed system is intended to provide a fully autonomous solution including cell localization followed by injection by single-cell electroporation. Furthermore, with the addition of two rotation stages, a novel configuration for a biomanipulator is obtained and can potentially achieve more difficult tasks including the injection of clustered cells. The inclusion of linear, direct-drive, servo-motors will provide this biomanipulator with additional speed and acceleration over conventional systems. Furthermore, proposed vision algorithms will take into account the viability of cell, an important factor for successful electroporation, and perform single-cell electroporation based on a suitable cell located.

1.4 Outline of Thesis

This thesis contains 8 chapters, which are outlined in the order described below.

In Chapter 1, the objective of the project is defined followed by a literature survey of the state-of-the-art in biomanipulation with a focus on the microinjection of mammalian cells. Finally, a brief outline of the structure of this thesis is presented.

Chapter 2 provides a task description of the automated microinjection process the biomanipulator will carry out. An overview of the subsystems are provided, and section numbers are provided to the reader for quick reference.

Chapter 3 covers the problem formulation, the conceptual models investigated for biomanipulation, and a description of the physical hardware subsystems that were implemented to satisfy the objectives. These include *(i)* the optical system composed of the microscope, and digital camera, *(ii)* the electromechanical system consisting of the robotic stages and mounted components, and finally *(iii)* the controller module

and software used to monitor the kinematics of the system components and provide closed loop control. Chapter 3 also explains the need for custom designed mechanical structures to overcome mechanical disturbances such as vibration and backlash in conventional motors.

In Chapter 4, the fundamentals of electroporation is described. An understanding of the differences between bulk-electroporation and single-cell electroporation is given, and an explanation of how single-cell electroporation was implemented on the biomanipulator.

Chapter 5 provides an explanation of what visual servoing is, and how it is implemented in the control design. Additional control subsystems and methods including: the camera model, optical vision configuration, computer vision algorithms, and the error function used during visual servoing are presented.

Results are discussed in Chapter 6, and are broken up into three sections, and include the results of: *(i)* the mechanical design, *(ii)* localization and segmentation of mouse myeloma, and *(iii)* single-cell electroporation.

In Chapter 7, conclusions are drawn regarding the research presented in this thesis and future work is described in Chapter 8.

Chapter 2

System and Methodology Overview

2.1 Proposed Biomanipulator System and Methodology

The goal of biomanipulator was to create a multi-axis, automated tool capable of performing biomanipulation tasks such as localized microinjection on cells within a Petri dish. This required several subsystems to be completed including: a multi-degree-of-freedom mechanical subsystem, optical subsystem, computer vision subsystem, and an end-effector for microinjection. Concluding the integration of these subsystems, the biomanipulator was required to:

1. Scan a Petri dish for suitable mammalian cells,
2. Automatically locate a cell (10 μm to 20 μm) using computer vision,
3. Use visual servoing to bring a cell near the tip of a stationary micropipette,
and
4. Inject the cell with a foreign material by single-cell electroporation.

Chapter 2 provides a high-level overview of the system starting with a description of the automated tasks required to be completed by the biomanipulator, followed by a description of each subsystem. References to other portions are provided to the reader, throughout this Chapter, for quick indexing.

2.2 Overview of the Automated Tasks

The 5 DOF autonomous biomanipulator, shown in Figure 2.1, is required to complete localized injection of foreign material into single cells situated in a cell culture. This task required the completion of several milestones including the localization of cell, determining the approximate radius of the cell, tracking the position of the cell as it is moved toward the end-effector, and then single-cell electroporation.

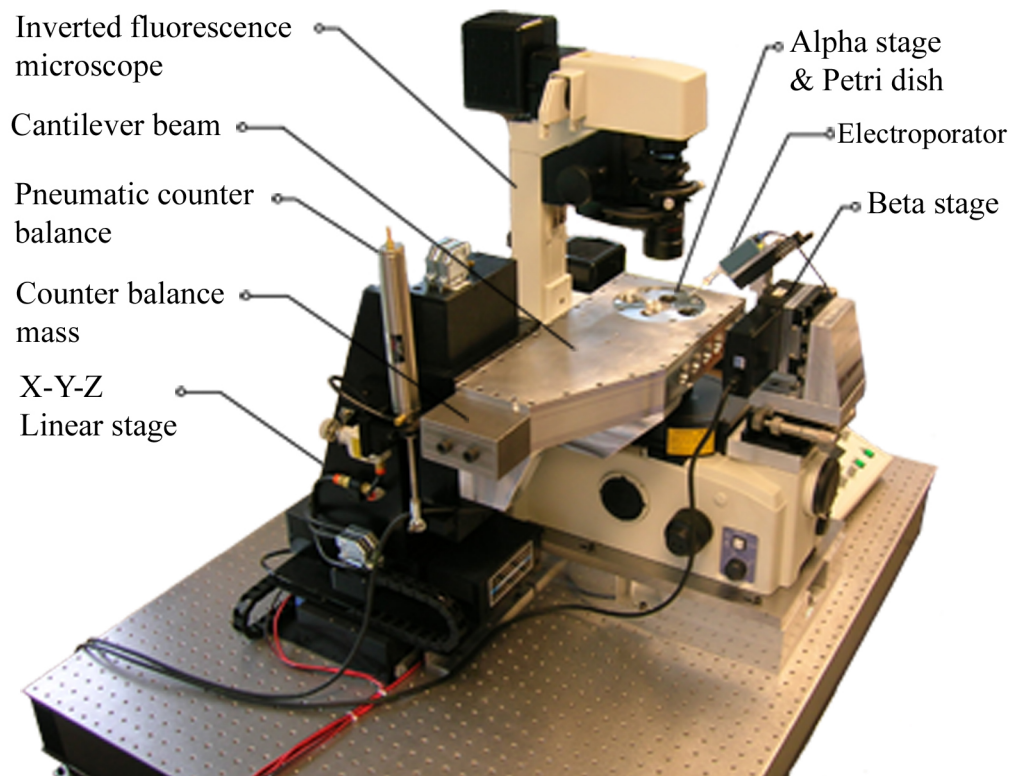


Figure 2.1: Image of the biomanipulator assembly

2.2.1 Localization and Segmentation

Upon initialization, the Petri dish is scanned moving the cell culture from left to right. Using greyscale template matching, described in Section 5.5.3, a cell is located (Figure 2.2). An image of the identified cell is stored in computer memory in order to track the cell as it is brought close to the tip of the micropipette (Figure 2.3).

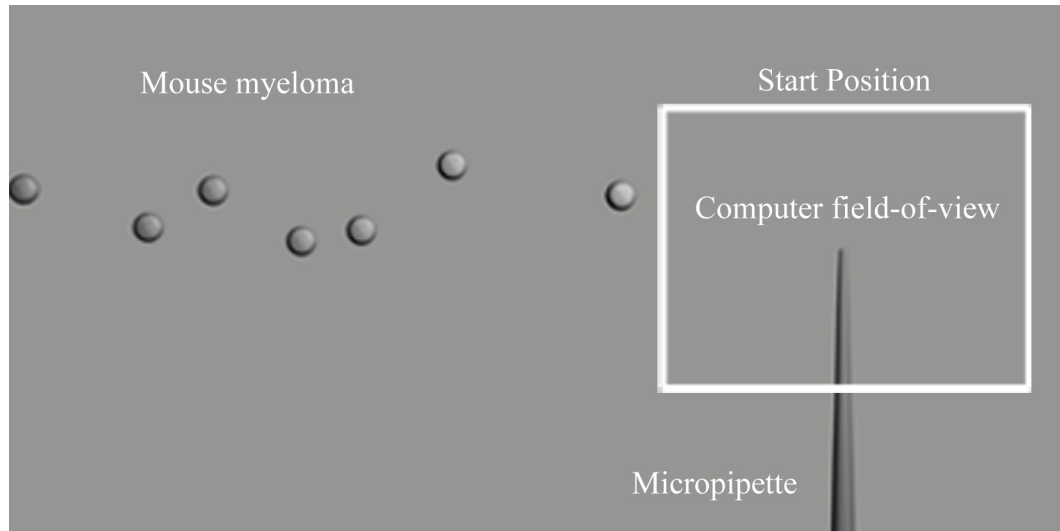


Figure 2.2: Starting position: The white square frame represents the area that is within the field-of-view of the image sensor and subsequently post-processed.

Using computer vision autofocus techniques (described in Section 5.5.7), the cell is brought into focus.

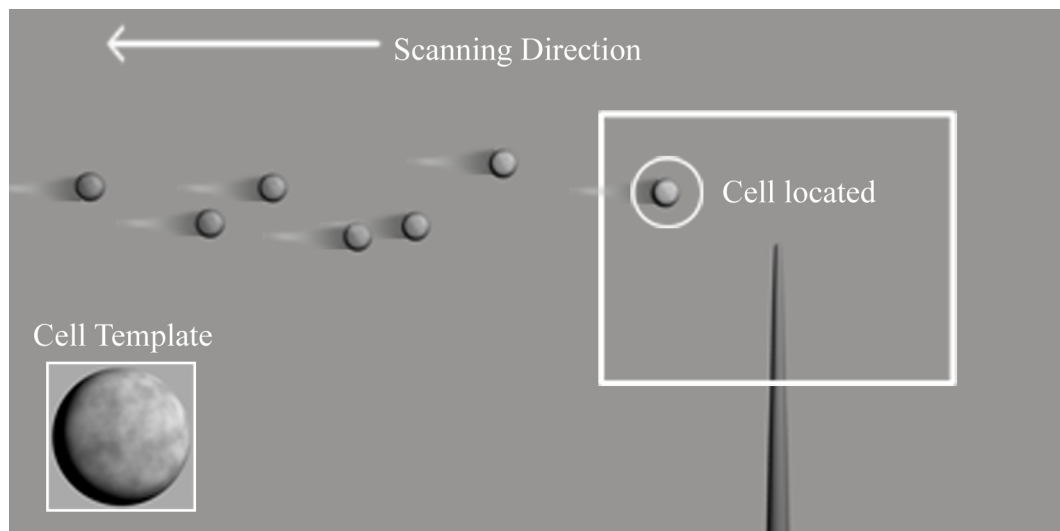


Figure 2.3: Cell localization: The biomanipulator scans the cell culture for potential cell targets. The localized cell requires a high correlation value, in comparison with the template (inset), to be considered a suitable match. The circled cell represents the localized target.

2.2.2 Tracking

Using the acquired template image of the cell during localization, and the sum of squared differences (discussed in Section 5.5.5) the cell motion is tracked. The distance between the cell and the micropipette tip, which defines the error function (described in Section 5.4), is reduced until the cell is brought sufficiently close to the end-effector tip (Figure 2.4).

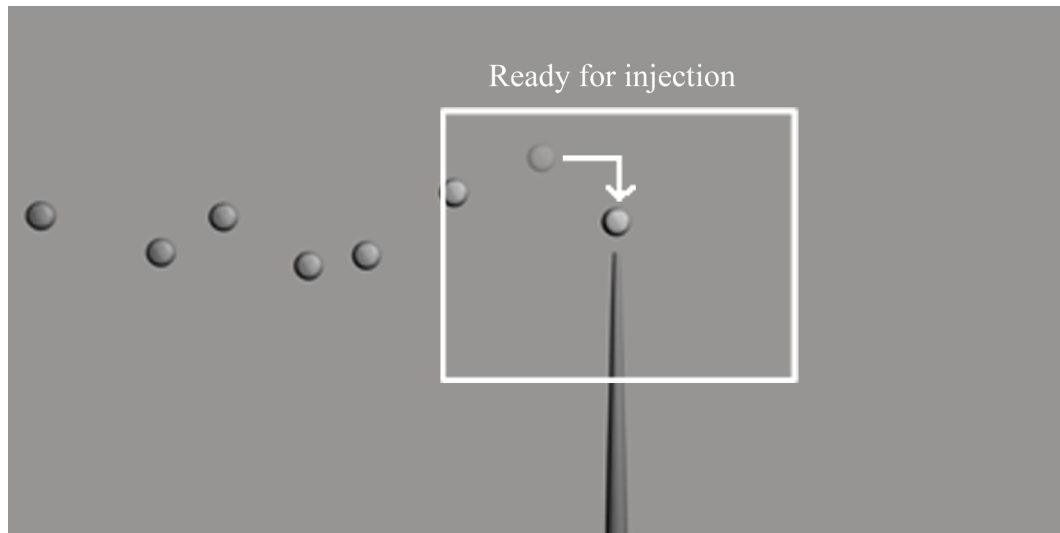


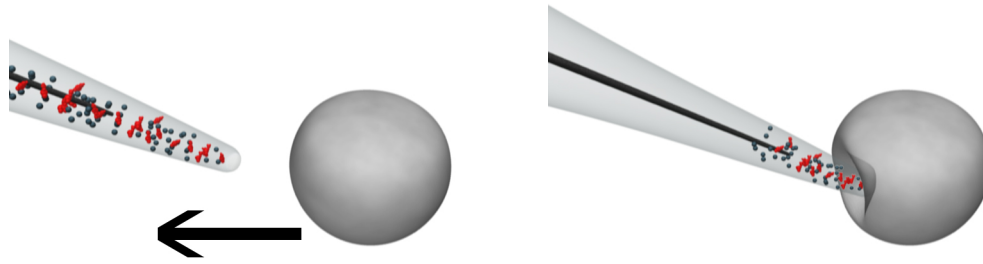
Figure 2.4: Injection preparation: The biomanipulator moves the cell to be inline with the current orientation of the micropipette. The top portion of the cell has been removed in this illustration.

2.2.3 Single-cell Electroporation

Single-cell electroporation is the process for introducing material into single cells. In this work, an Axon Axoporation 800A™, a commercially available SCE device, is used for injection and measuring impedance in the Petri-dish. The end-effector or injection device is a micropipette which contains molecules to inject into the cell. These molecules contain a net electrical charge, and applying a potential to the electrode forces the similarly charged material out of the micropipette (see Section 4.2).

After the cell has been brought to rest near the tip of the micropipette, control

is switched from visual control to control based on cleft resistant measurement. The micropipette tip is slowly advanced toward the cell and indents the cell membrane with the micropipette tip as shown in Figures 2.5(a) and Figure 2.5(b) respectively. An sharp increase in the resistance measured by the Axoporation 800A™.



(a) Cell approaching micropipette tip (b) Cell indented against micropipette tip

Figure 2.5: SCE Routine: motion of cell with respect to the micropipette tip.

The resistance increases when the tip of the micropipette is pressed up against the cell membrane due to an increase in surface tension between the tip and the cell membrane (Figure 2.6). This is known as the cleft resistance, or the resistance between the micropipette tip and the cell membrane. Once an approximate 33% increase in resistance is obtained, approximately 25% of the input voltage is applied at the cell membrane and temporary openings in the cell membrane allow material to enter and be trapped within (Figure 2.6).

The molecules that were preloaded into the micropipette tip are forced out of the opening of the tip into the openings created in the cell membrane (Figure 2.7) using electrophoresis and electro-osmosis (described in Chapter 4).

After a preset amount of time, the electric field is halted and the biomanipulator begins to scan for its next target. Injecting Alexa 568 allows manual verification of successful electroporation by temporarily illuminating the cell by epi-fluorescent light. Successfully injected cells will appear evenly bright compared to cells not

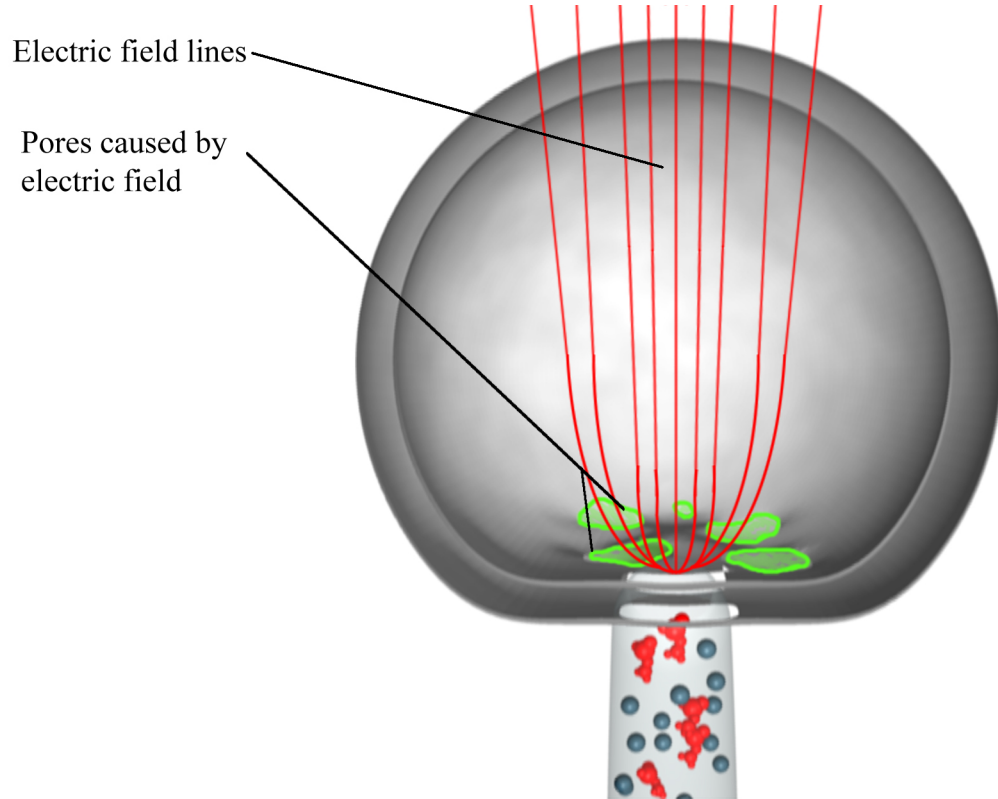


Figure 2.6: Cell indentation: the biomanipulator moves the micropipette against the cell membrane causing the cell membrane to deform. This causes the cleft resistance to increase due to increased surface tension.

electroporated or unsuccessfully electroporated cells.

2.3 Biomanipulator Subsystems

2.3.1 Mechanical Subsystem

The biomanipulator is a 5-DOF system, shown in Figure 2.1 and consists of 3 linear stages for translating the end-effector in \hat{x} , \hat{y} , and \hat{z} directions, and 2 rotation stage to rotate the end-effector about $\hat{\alpha}$, and $\hat{\beta}$ (see Section 3.3). The biomanipulator provides vibration control through isolation mechanisms and careful design of critical components such as the cantilever beam structure holding the cells (see Section 3.6), and the backlash free motors (See Section 3.5.1). The system is deemed a hierarchical system [7], which means that a joint controller is used to stabilize joints and will

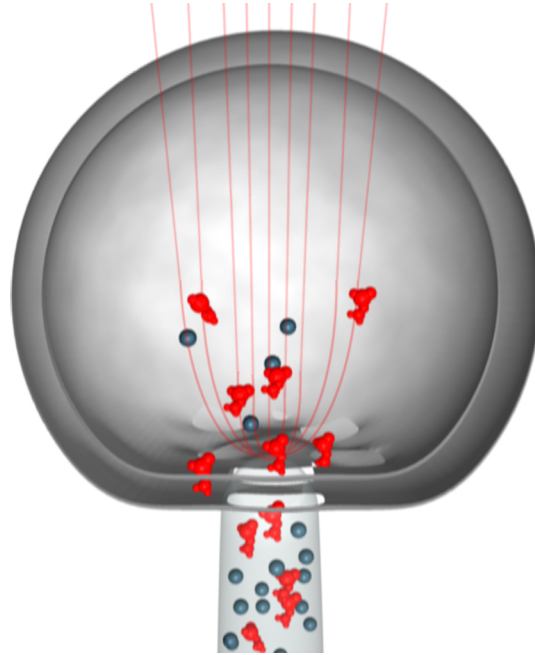


Figure 2.7: SCE: induced electric field pulses move charged particles through temporary openings in the cell membrane.

accept positional or velocity commands from algorithms (see Section 3.7).

2.3.2 Optical Train and Vision Subsystem

The optical system was chosen to capture sequential images of biological cells, while supply ample room to manipulate cells in an open environment such as a Petri dish. Therefore, a Nikon Eclipse™ inverted microscope with an ultra long working distance, differential interference contrast (DIC) objective was selected to image cells (described in Section 3.4.3). Images were then digitized for post-processing using a complimentary metal-oxide semiconductor image sensor which was capable of providing a relatively high number of frames-per-second in comparison with charge coupled device image sensors (discussed in Section 3.4.5).

2.3.3 Control Subsystem: Visual Servoing of Biological Cells

Visual servoing [26], a term that appeared in literature less than three decades ago, provides a dynamic response to observed changes in captured image data. The ben-

efit, is a system that provides dynamic visual information of environments that are loosely structured. This information can be used to correct the alignment of tools or determine a course of action depending on observed visual features. The biomaniipulator developed in this work uses visual servoing, and is further classified as a dynamic image-based look-and-move structure (DIBLM) [7]. DIBLM is a classification of visual servoing that is hierarchical and takes advantage of commercial motion controllers that accept velocity commands. This reduces the non-linear effects of a pure image-based visual servoing system (IBVS). Furthermore, in comparison to position-based visual servoing systems, which rely heavily on the kinematic calibration of components, the DIBLM structure relies on observed image features reducing the error and precision required from the mechanical structure (described in Section 5.2).

Visual servoing is close-loop control utilizing visual feedback and error based on observed changes in image features (*i.e.* the distance between two points, *etc*). There are different classification of visual servoing (see Section 5.2); however, in this work control is based on the DIBLM structure described by [7]. This involves the following tasks:

1. Capture an image,
2. Extract features from the image (such as the centroid of a cell),
3. Calculating the error based on an error function (such as desired and current position),
4. Subject the error value to the feature base control law,
5. Pass control values (such as velocity) to the motion controller, and
6. Reiterate until the error term is zero.

The error function (described in Section 5.4) is responsible for determining the point at which a cell moves from its current position to the desired position. The desired position is directly in line with the orientation of the tip of the micropipette several microns away. The function used is based on the implementation of [34], and used in a similar application by [10] who used a microinjection micropipette to inject oocytes. The error function reduces the error to zero by providing joint velocities to minimize the error of the position of the cell with respect to the desired position and the weight of the control input.

2.3.4 Injection Subsystem: Single-cell Electroporation

Injecting cells in an automated system should be fast and efficient. Single-cell electroporation (SCE) [35] [3] [36], a technique that evolved from bulk-electroporation [37] (described in Chapter 4), is a less invasive solution to microinjection. SCE uses a micropipette electrode assembly that is loaded with the foreign material to inject into a cell. The electrode is capable of inducing an electric field (discussed in Section 4.2) causing oppositely charged molecules to flow out of the tip by electrophoresis. Pressing the tip of the micropipette against a cell membrane, and activating the electric field creates temporary openings in the cell membrane. The electric field also causes the similar charged molecules to flow out of the micropipette. Oppositely charged molecules also flow through the pipette tip by electro-osmosis through the cell membrane openings, and are trapped upon stopping the electric field. This method allows the uptake of many foreign molecules, including DNA.

Chapter 3

Design Procedure

3.1 Background

Traditional cell micro-injection is done by a human operator using an inverted microscope and requires a 3-DOF motion stage allowing the operator to position the micropipette tip anywhere in the \hat{x} , \hat{y} , or \hat{z} directions. The system works as follows: adjustments of a 2-DOF stage modifies the \mathbf{x} , and \mathbf{y} position of the stage on the horizontal plane, and the other DOF changes the \mathbf{z} position of the stage relative to the microscope objective. To design an automated system to achieve these same tasks, the conceptual design for the hardware implementation can be broken into three partitions: *(i)* the optical system, *(ii)* the electromechanical system, and *(iii)* the end-effector. This chapter provides details the operational and design requirements for the optical and electromechanical system, a description of the two configurations considered for the biomanipulator, and a description of the hardware chosen to implement the biomanipulator. The end-effector is described in Chapter 4, which is dedicated to providing the background information and a description of the science of the microinjection device known as the single-cell electroporator.

3.2 Operational and Design Requirements

Currently, biomanipulation is a manual process that is tedious, laborious, and lacks the desired throughput and repeatability. Automating tasks such as microinjection requires the successful integration of state-of-the-art technologies. This is done by creating a conceptual model, analysis of a working design, construction of a proof-of-concept, and re-assessment of the design. During the development of each stage it was necessary to retain sight of the goal throughout the process which is to exceed the performance of the human operator during a manual microinjection. With the objectives outlined in Section 1.1 and the goals in Section 1.4, a set of operations were defined, shown in 3.1 in order to achieve the task of automated cell microinjection.

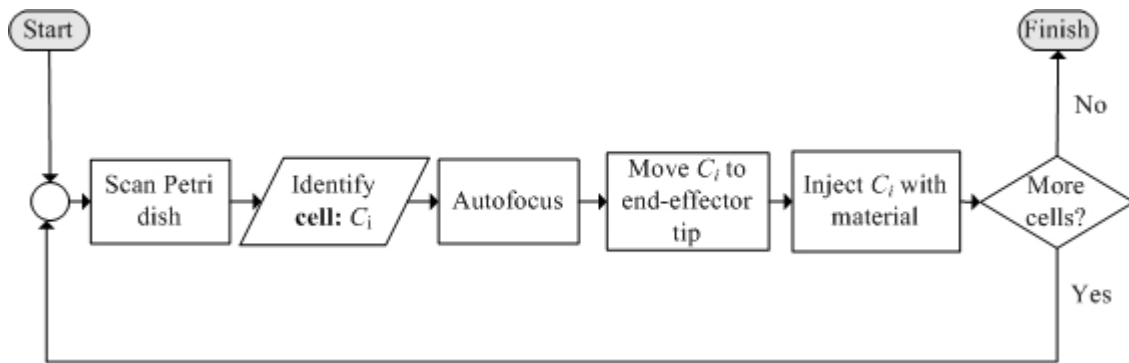


Figure 3.1: Operational flow chart

The system design required the integration of multiple motion stages with a commercial off-the-shelf microscope. It was also decided to ensure that the linear motion provided a minimum of 1.0 μm resolution while moving the end-effector about the diameter of a mammalian cell, that is on the order of 10 μm . Furthermore, the optical resolution of the microscope was selected to match, as closely possible, the minimum requirement for the mechanical resolution of the stages to allow precise control in positioning the end-effector next to the cell membrane. The maximum travel range of the biomanipulator is based on the approximate diameter of the glass bottom of a 35 mm inspection Petri-dish. Finally, in addition to the operational requirements,

two additional design requirements were outlined including a unrestricted horizontal workspace of no less than 15 mm in any direction, and the ability to orientate the end-effector about the z-axis.

3.3 Configuration of System Axes

The end-goal for the configuration of the biomanipulator is to provide the following: (i) provide relative motion of the micro-injector with respect to the cells, and (ii) provide relative motion of the cells in respect to the microscope objective. Two configurations for the autonomous biomanipulator were considered as possible solutions. *Configuration 1* involved 8-DOF, which included six linear actuators and two rotation stages. *Configuration 2* involved 5-DOF, which included only three linear actuators and two rotation stages.

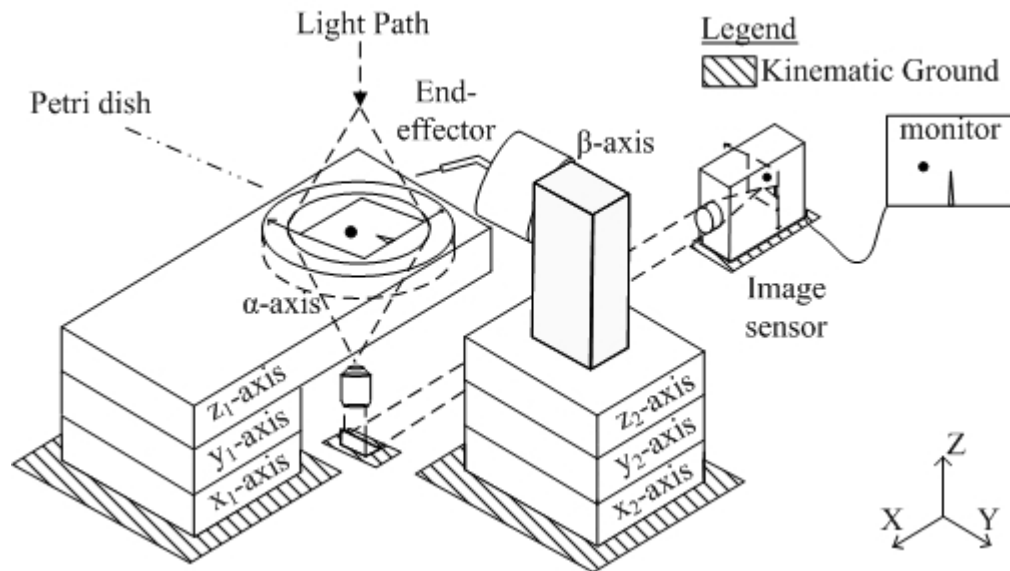


Figure 3.2: *Configuration 1* conceptual representation of the biomanipulator

Configuration 1, shown in Figure 3.2 involved a horizontal stage holding the Petri-dish and a rotation stage to vary the angle of the Petri-dish moving relative to kinematic ground allowing the biomanipulator to scan through the Petri-dish for cells. *Configuration 1* also required an end-effector moving relative to kinematic

ground allowing the end-effector to be positioned anywhere within the field-of-view. This concept's advantages included the freedom to move the end-effector relative to the stage with minimal disturbances to the stage platform, and removing the end-effector from the injection area to avoid steering about obstructions. This concept was eliminated due to several disadvantages including: (i) requiring 8-DOF to control both the end-effector and the stage supporting the observation platform, (ii) increased complexity due to the coordination of both the stage and end-effector motion, (iii) increased system cost, and (iv) redundant axes.

Configuration 2 involved five axes including x , y , z , α , and β and is illustrated in Figure 3.3. *Configuration 2* maintains a static end-effector tip with respect

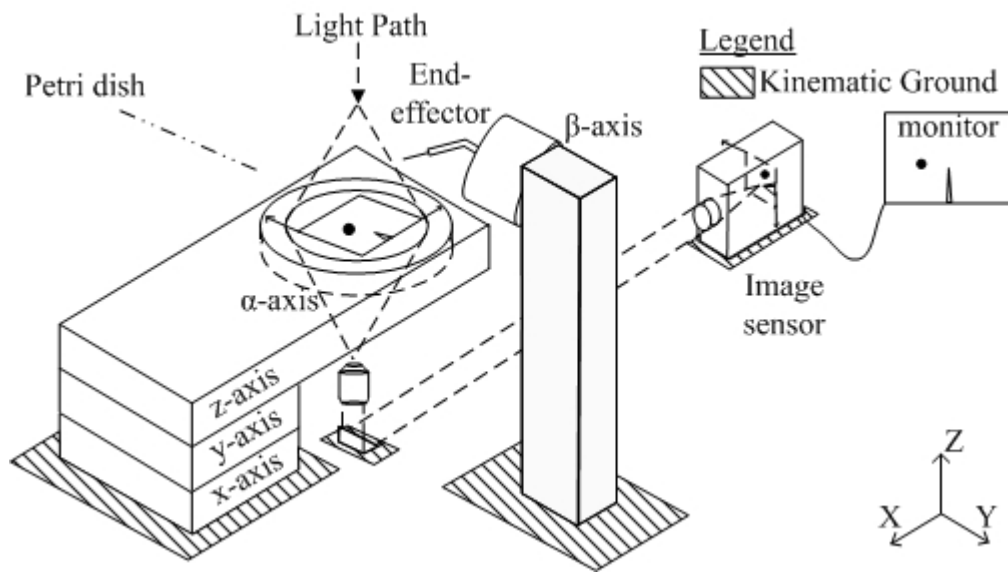


Figure 3.3: *Configuration 2* conceptual representation of the biomanipulator

to the camera, while the platform holding the Petri dish moves with respect to the camera. This is done by mounting the end-effector onto the beta axis whose motion does not move the end-effector tip out of the field of view. This can be further exploited by calibrating the end-effector to be in focus with the microscope objective prior to operation. Secondly, the control system required to monitor five axes instead of eight reduces the computational load of the robotic controller, and reduces the

need to track the position of a mobile end-effector using computer vision.

This 5-DOF system is capable of positioning an end-effector tip in any position in three-dimensional space since the tip is symmetrical about its own axis. It also satisfies the additional design requirement of varying the orientation of two axes. This increases the flexibility for more difficult tasks which may include the manipulation of clustered cells or changing the orientation of the end-effector with respect to a position on a non-spherical cell. Administration tasks such as auto-focusing can still be achieved through *Configuration 2* by adjusting the vertical position of the platform holding the Petri dish to the objective focal point on the inverted microscope. The end-effector will be mounted at a fixed 45 degree angle-of-attack with respect to the target cell, and rotates about the beta-axis which is in contact with the kinematic ground, and common to the x -axis. The intended optical path in *Configuration 2* starts from the top of the Figure 3.3, passes through the target cells and onto the camera sensor located at the bottom or the side of the inverted-microscope housing. In either configuration, one unavoidable disadvantage is the need to create a cantilever beam to support the rotation stage and Petri dish over the microscope objective which is further discussed in Section 3.6.

3.4 Optical Assembly

The optical system required a careful analysis and selection of optical components to view thin and nearly transparent cells 10-20 μm in diameter, and to resolve detail greater than 1 μm . Other requirements that were considered included the desire to observe the detail of internal cell activity, provide high contrast between the cell and the surrounding medium, and to have a high enough frame rate to avoid delays between frame captures and the image processing algorithm. It is necessary to provide some background details regarding microscopy and digital imaging techniques such as resolving power and several current methods of illumination. Further resources are

readily available to the reader at Michael W. Davidson's online Microscopy library at <http://www.microscopyu.com>, which is a thorough free online resource on microscopy and optics in general.

Firstly, an understanding of the relationship between numerical aperture and optical resolution is required to assist the reader in understanding the limitations on viewing small objects not discernable by the human eye. The numerical aperture, or the light gathering ability of an objective, plays a critical role in resolving detail. Resolving power, or resolution, can be defined as the ability to clearly distinguish the distance between two points on an object by a camera or observer. Resolution can be described by the following,

$$resolution = \frac{1.22\lambda}{NA_{OBJ} + NA_{COND}} \quad (3.1)$$

where λ is the wavelength of the emitted light (generally midband of the visible spectrum, 550 nm, is used for calculations), and NA_{OBJ} and NA_{COND} is the numerical apertures of the objective and condenser respectively. To achieve a resolution of no less than 1 μm using eq. (3.1) and the mid-band wavelength for visible light, 550 nm, the combined numerical aperture must be greater or equal to 0.34. Therefore, the optical train, including the objective and condenser, must provide optical components that satisfy this limitation. It is important to note the performance tradeoff in varying the combined NA of the system, and is apparent in the following according to Abbe diffraction theory,

$$NA = n \cdot \sin\phi_i \quad (3.2)$$

where n is the index of refraction of the material, and ϕ_i is the angle-of-incidence which is the angle between the optical axis of the objective and the perimeter of the lens. Increasing the NA of the optical components, specifically the objective, is proportional to the angle of incidence. In practice, as the NA of an objective increases

the objective lens diameter is required to become sufficiently wide or moved closer to the specimen in order to capture the light. Another method of overcoming this hurdle is to increase the refractive index of the interface between the objective and the surface of the Petri dish. One method that accomplishes this is to use special objectives designed to provide a layer of oil between the lens and the observation slide or inspection dish. The oil provides a higher NA than would air; however, the use of the oil and glass interface is believed to complicate the mechanical design of the biomanipulator.

The depth-of-field, calculated by eq. (3.3) [38], also plays an important role in microscopy and computer vision techniques,

$$DF = \frac{\lambda n}{NA^2} + \frac{n}{MNA}e \quad (3.3)$$

where DF is the depth-of-field, n is the refractive index between the medium existing between the coverslip and the objective front lens ($n_{air} = 1.0$), M is the magnification of the objective, and e is the smallest distance that can be resolved by the image sensor. Using the combined efforts of a high NA objective and condenser, a shallow focal plane of the image sensor, and a high magnification from the objective a thin depth-of-field is obtained. A thin depth-of-field allows a method of viewing thin optical sections of the specimens. Furthermore, this provides a method of aligning the micropipette tip with the visible section of the cell if the depth-of-field is much smaller than the specimen being viewed as illustrated in Figure 3.4.

After the determination of the minimum NA and the decision to use a glass-air interface objective, the desired method of microscopy illumination was investigated. Three common methods of microscopy illumination, used both in industry and academic research, were considered for viewing live, thin, and nearly transparent biological cells. These include (i) phase contrast, (ii) differential interference

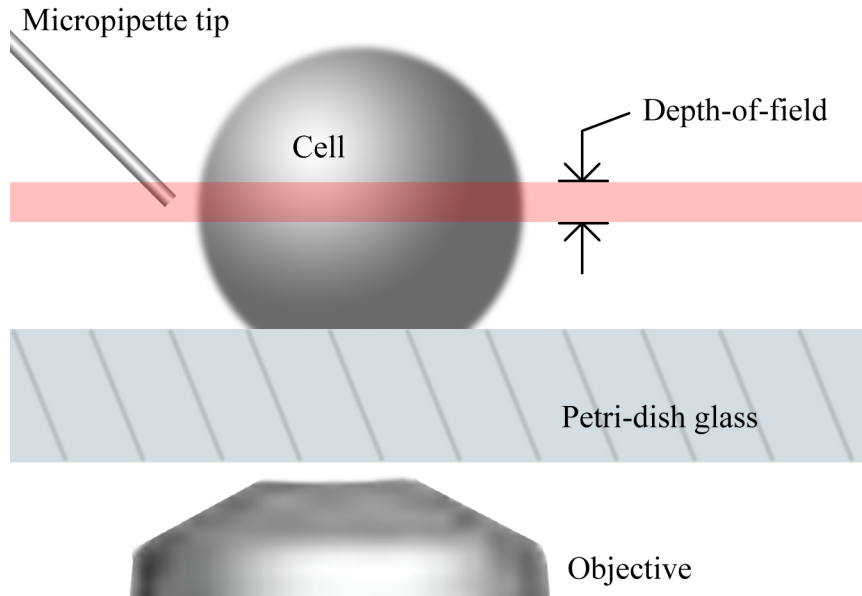


Figure 3.4: Depth-of-field

contrast (DIC), and *(iii)* Hoffman modulation contrast (HMC). Several other methods of microscopy were explored and rejected for various reasons. Scanning electron microscopy (SEM) provides a very high resolution image at high magnifications; however, specimens must be bombarded with gold particles and placed in a vacuum for optimal viewing. Dark-field illumination provides an image with a dark background and specimen edges with high-contrast. This effect is created by scattered light and discontinuities in refractive index in the specimen. If too many features are present in the field of view, using dark-field illumination, the image quality deteriorates [39]. Therefore, dark-field illumination was rejected.

3.4.1 Phase Contrast Illumination

Phase contrast was developed during the 30's and provided an alternative to transmitted brightfield illumination. It is capable of viewing thin and nearly transparent biological specimens and the contrast of the specimen remains consistent with changes in orientation. Phase contrast illumination uses a special annulus to create what can be conceptualized as a cone of light. This cone of light is focused on and around the

specimen. Light that passes around the specimen is unaltered. Light passing through the specimen is diffracted due to a change in optical path length. The optical path length is defined to be,

$$\text{OpticalPathLength} = n \cdot t_s \quad (3.4)$$

where t_s is the thickness of the specimen that the light is traveling through, and n is the index of refraction. When a parallel wavefront enters materials with a different thickness or different index of refraction they will exit with a change in phase due to a difference in velocity through the different mediums, and can be described as,

$$\text{PhaseShift} = 2\pi \cdot \frac{\delta}{\lambda} \quad (3.5)$$

where the phase shift is in radians. δ is the difference in optical path lengths between the two materials and is defined as,

$$\delta = n_2 \cdot t - n_1 \cdot t \quad (3.6)$$

where n_1 is the index of refraction for material one and n_2 is the index of refraction for material two.

The diffracted light passing through the the specimen is usually retarded by approximately one-quarter of a wavelength of light [40], and is lower in amplitude than the surrounding wave due to fewer photons interacting at that point in the image in comparison to the surrounding or background light. The wavefront that passes unaltered by the specimen is advanced by another quarter wavelength and is also reduced in amplitude by a special coating on an annulus. The two wavefronts are recombined and due to constructive interference differences in optical path lengths, are represented as varying changes in amplitudes that are interpreted by human or

computer vision as changes in contrast.

Phase contrast possesses a unique optical artifact known as the halo effect predominant in all phase contrast images. The halo-effect is usually observed as an intense halo appearing at the boundaries between the perimeter of the specimen and the background. This is caused by a small amount of light being refracted by the specimen and is transmitted by the circular phase-retarding ring located in the objective.

3.4.2 Hoffman Modulation Contrast

Hoffman modulation contrast is another method of viewing thin and nearly transparent specimens, and was developed in the 70's by Dr. Robert Wollaston, who holds a patent on the technology. HMC differs from phase contrast such that the light does not undergo a phase shift. This is especially important and useful when observing specimens through plastic dishes where birefringence effects are more likely to take place. The operation of HMC occurs such that light emitted from the condenser passes through a specimen and is refracted at varying angles. The light then passes through a special optical mechanism known as a modulator plate and is absorbed at different intensities depending on the angle of refraction. The light that is strongly refracted will appear either very dark or very light in contrast with the less refracted background light. This procedure creates a shadow-like optical artifact that is present in some other methods of illumination such as DIC (see Section 3.4.3). Unlike DIC the front focal plane of the condenser is not fully illuminated thereby reducing the amount of transmitted light and reducing the image quality [38].

3.4.3 Differential Interference Contrast

De Senarmont differential interference contrast is another widely used method for viewing specimens that are poorly visible using normal brightfield illumination. Light from a non-polarized light source such as a tungsten bulb passes through a polarizer

and is then split into two beams by a quarter-wave retardation plate. A slider on the quarter-wave retardation plate controls the relationship between the wavefronts, and in turn controls the optical path difference. These wavefronts are then separated by a distance much smaller than the resolution of the microscope optics by a Wollaston prism and then focused onto the specimen by the condenser. The light enters the specimen and any difference in optical path length between the two wavefronts result in a phase change difference or a noticeable retardation between the two wavefronts. The wavefronts exit the specimen, and are magnified by the objective. Following magnification, they are recombined by a second Wollaston prism and summed by an analyzer upon exit. Any differences in phase, caused by varying optical path lengths, result in interference changing the resultant amplitude of the light, which is visually interpreted by changes in contrast.

Nomarski DIC produces similar results; however, does not use an adjustable quarter-wavelength retardation plate after the polarizer. The two wavefronts propagate orthogonally with respect to each other. Normarski DIC allows a user to vary the contrast similar to De Senarmont by a sliding Wollaston prism. Differential interference contrast also has an artifact similar to HMC. The interference caused by the combined wavefronts causes an apparent directional shadow effect. This shadow effect is also known to cause difficulties in computer vision in localization and segmentation and has been investigated within the last decade [17] [41] [16].

3.4.4 Comparison of Phase Contrast, DIC, and HMC

Viewing thin and nearly transparent biological cells requires a microscopy method that is able to enhance the image such that our human eyes or computer vision technology are able to detect changes in contrast to provide information about the acquired image. Three methods of microscopy were considered for implementation with the design of the biomanipulator: *(i)* phase contrast, *(ii)* Hoffman modulation contrast, and *(iii)* differential interference contrast.

Phase contrast provides a method of illumination unaffected by orientation dependent artifacts such as the shadow effect produced by DIC. This is direct advantage in terms of processing sequential images since one of the tasks will be to repetitively locate the same cell in sequential images. Differences between images increase the potential in losing the relationship of an item between one frame to the next. This is problematic, given the configuration of the biomanipulator, since it has a rotation stage for changing the orientation of a cell. Under phase contrast, while rotating a cell on the rotation stage, the contrast of the specimen in sequential images will be consistent. In contrast, using DIC, the specimen will rotate while the shadow will appear to be cast in the same orientation. Therefore, large rotations will produce significantly different images. However, the drastic changes in spatial frequencies (the change from light to dark regions) caused by the halo effect will cause false edge detections to occur. The biomanipulator is required to determine the approximate location of the edge of a cell so that a micropipette tip can be maneuvered near the cell membrane. DIC provides sharp contrast changes where edges occur allowing a more accurate representation of the relative position between the pipette tip and the cell membrane.

HMC produces a similar image to DIC and is also less expensive than DIC. This is primarily due to the absence of the expensive Wollaston filters required in de Senarmont DIC. HMC is less influenced by interference fringes when viewing specimens through plastic bottom Petri dishes [42]. The images produced by HMC are very similar to DIC images such that a shadow-like optical artifact is present. However, in comparison to DIC, the amount of illumination is comparatively less, thereby reducing the amount of transmitted light. This effectively reduces the image quality [38]. Furthermore, with DIC, the contrast is adjustable over a wide range allowing varying lighting conditions to be adjusted while HMC presently lacks this ability.

Given three options for selection of the main method for microscopy illumination,

DIC was chosen as the preferred method. This choice was based on minimizing false edge detection by maximizing high spatial frequencies. This characteristic was believed to be much more important than the non-orientation dependant characteristic of phase contrast. Furthermore, the ability to maximize the quality of the image and the amount of illumination eliminated HMC. A further benefit that may prove useful with DIC is the ability to obtain section images of specimens for three-dimension image reconstruction [43] [44]; however, is not explored in this work.

3.4.5 Digital Sensors

The digital sensor (camera) is the final component of the optical train and converts the light passing through the objective into a digital representation. The resolution of the image sensor must be consistent or better than the performance of the optics preceding it. Image sensors are common to computer vision projects and include several benefits inherent to digital processes including discrete site manipulation, digital signal filtering, speed, and less sensitivity to the influences of noise. Current digital imaging technology is produced commonly in two forms: charged-coupled device (CCD) sensors and complimentary metal oxide semi-conductor (CMOS) sensors. The two devices differ in several ways including fabrication technique, operation, performance, and physical layout. Currently the market is dominated by CCD imaging devices likely due to the superior image quality [45].

CCD image sensors can be conceptualized as an array of millions of microscopic wells, known as photosites, which are metal-oxide semiconductors (MOS) that collect photons of light and convert them to electrical signals. The sensor array collects a sample of light. Each row of photosites passes the collected charge to the next row closer to the edge of the array. Once the charge is passed to the row that resides at edge of the array, the charge from each photosite is passed to a voltage converter and amplifier resulting in a low noise signal. This sequential nature of this operation is complex and suffers from a high latency in producing frames. At the

user's discretion, the CCD camera can be programmed to use a technique known as binning. Binning is a process that decreases latency at the cost of lower spatial resolution. It is achieved by summing pixels over a larger area. These areas are read as one super pixel which further increases the signal-to-noise ratio. The reduction in time is proportional to the square of the super-pixel area; however, is limited by the capacity of the accumulator (*i.e.* well containing the accumulated charge).

CCD image sensors also have several other problems such as blooming, fading, and smearing. Blooming is a condition where some charge leaks to neighboring sites. Fading occurs when sites lose their charge during the transmission of one row's charge to the next. The last condition, known as smearing, occurs when a photosite absorbs photons prior to delivery to the amplifier for readout. The complexity of this timed sequence also requires special bias voltages and higher voltage timing circuitry resulting in high-heat dissipation and a larger footprint.

CMOS image sensors are an evolving technology and the image quality is increasingly approaching that of CCD technology [46]. Although the image quality of a CMOS image sensor does not have the same quality as a CCD image sensor, it has several unique features that rival the performance of a CCD sensor. Therefore, it was necessary to review the characteristics of CMOS sensors for the purposes of using this technology as the image collecting device for the biomanipulator.

The CMOS grid, unlike the CCD sensor, consists of an integrated photosite commonly including a voltage converter, dedicated select and reset circuitry, and an onsite amplifier. On-site, dedicated components increase the functionality and the speed of the sensor; however, reduce the overall ratio of light collecting area per site. CMOS sensors can be further classified into two variations including passive and active pixel sensors. Active pixel sensors have two stages of amplification providing a higher signal-to-noise ratio as opposed to passive pixel sensors.

A primary advantage of CMOS sensors is the ability to dynamically select a

region-of-interest (ROI), or a subsection of the entire sensor for processing allowing a reduction in pixel-processing latency without a loss in image window resolution. This is highly advantageous for post-processing images in real-time applications such as biomanipulation. ROIs can be reduced to only the area of concentration such as the micropipette tip moving near the cell membrane. Other areas of the image are not captured by the CMOS image sensor, and the number of pixels require processing can be highly reduced. In addition to performance gains, since CMOS fabrication techniques are not restricted to creating image sensors, the efficiency of such techniques allow these sensors to be manufactured at a fraction of the cost in comparison with CCD sensors [46].

The CMOS sensor has known faults including fixed-pattern and random, reset noise which becomes apparent in post processing. Furthermore a degradation of image quality is caused by the large capacitances in the input of the output amplifier causing a lower signal-to-noise ratio reducing the sensor sensitivity. Optical equipment manufacturers, such as Canon, provide methods to reduce and eliminate such noise by introducing a two-step process. This involves measuring the noise prior to collecting the photons and then subtracting them off the summed noise and actual light measured.

A CMOS sensor was selected as the sensor to provide digital imagery for the biomanipulator. This decision was heavily weighted on the ability to capture frames at a much higher rate than CCD sensors, as well as provide its unique ability to select regions-of-interest on-the-fly which will reduce both the image transfer latency as well as the image post-processing latency.

3.4.6 Optical Component Selection and Validation

Concluding the selection of optical component criteria the microscope and camera were selected. Table 3.1 and Table 3.2 provide a summary of the microscope and image sensor devices respectively to meet the objectives for the biomanipulator.

Table 3.1: Microscope Specifications

Microscope	
Configuration	Inverted
Illumination Method	DIC
Model	Nikon TE-2000U
Microscope Objective	
Objective Numerical Aperture	0.7
Magnification	42 to 60 X
Condenser Numerical Aperture	0.5 (Ultra-long working distance)
Theoretical System Resolution	0.56 μm
Depth-of-field ($e = 4 \mu\text{m}$)	1.2 μm

Table 3.2: Digital Camera

Sensor Type	CMOS, mono
Pixel sensor array size	1280 X 1024 maximum
Model	Pixelink A741™
Camera mount	2/3" diameter, 0.7X Magnification
Pixel-pitch	6.7 μm
Typical frame rates	27 fps at 1280 X 1024
	105 fps at 640 X 480 (Ultra-long working distance)
	8000 fps at 472 X 8

The minimum theoretical resolution, using eq. 3.1 of the Nikon TE-2000U Eclipse including the numerical apertures of both the ultra-long working distance condenser and the objective was found to be 0.56 μm satisfying the 1.0 μm desired optical resolution. A higher NA was not considered to avoid the reduction in workspace and converting to high NA oil objectives.

To determine whether the Pixelink A741™ CMOS sensor satisfies the minimum sampling frequency requires the knowledge of the lowest magnification and the minimum resolution possible of the microscope optical train. Using the 60X magnification of the objective, setting the optional magnification on the side of the microscope to 1.0X, and the optical coupler is 0.7X the total magnification not including screen magnification is 42X. The minimum resolution of the microscope, 0.56 μm , is magnified onto the CMOS sensor at the minimum magnification is 42X. Consequently, the

resolution magnified by the minimum magnification on the microscope is 23.5 μm . A minimum of two pixels at the manufacturer specified pixel pitch of 6.7 μm per pixel satisfies this requirement; however, it is common practice to ensure that a minimum of three pixels satisfy this requirement which is also met by this sensor.

3.5 Electro-Mechanical Assembly

The mechanical system's function in the autonomous biomanipulator is to accept commands from a high-level algorithm and control the motion of the stage with respect to the microscope. The motion controller provides the interpretation of the signals generated by the high-level algorithm and provides signals to amplification devices, which in turn provide a driving voltage for the motors. Positional feedback from the motion devices is measured by the motion controller and is used for stabilization and decision making. The biomanipulator sub-assembly has three sub-sections which required a significant understanding to ensure the entire system provided seamless motion. These include the mechanical stages, the cantilever beam which supported the rotation stage, and the motion controller.

3.5.1 Mechanical Stage Selection

Satisfying the mechanical requirements of the conceptual model in Figure 3.3 required three linear stages (x , y , and z axes) and two rotational stages (α , and β). One basic requirements of these elements involved minimizing or completely eliminating backlash caused by the non-ideal translation of mechanical components in the micron-scale environment. Backlash, is caused by imperfect matching of gear teeth which causes lost motion and is commonly found in mechanical actuators such as worm-gear drives and stepper motors. Direct-drive linear motors eliminate backlash since the load is rigidly attached to the motor, therefore, transmission error is eliminated. The operation of a direct drive linear motor is similar to a conventional rotary motor, but the configuration of the motor can be thought of being unwrapped. The forcer, which

is analogous to the rotor, consists of coils packed in epoxy, the Hall-effect board, the stage platform, and the cables within a flexible cable management track. The forcer translates on a powerful rare earth-magnet track on steel, which in combination with the current loops provides the same electromagnetic force as would a regular servo motor. DC linear motors provide very accurate positioning capability and high-acceleration [47]. The speed, reliability, and precision are not affected by a rotary-to-linear coupler [48]. Position tracking is achieved using a linear encoder instead of a rotary encoder, and voltage delivery is stabilized using Hall-effect sensors.

Linear motors were chosen to implement the three linear axes for several reasons including *(i)* eliminating the effects of backlash, *(ii)* providing accurate linear motion with high repeatability, and *(iii)* to test the performance of biomanipulation with an unconventional motor. The linear stages chosen were Aerotech ALS-1000 stages hosting the BLMC-142 direct-drive, linear motor. These stages provide a manufacturer specified repeatability of 1.0 μm , an accuracy of 4.0 μm over its 100 mm range of travel, and a peak force of 422 N. Each three linear stages were configured to represent the x , y , and z -axis, and the z -axis was fitted with a pneumatic counter-balance to null the applied load and provide a braking mechanism in the event of a power loss.

The α -stage, used to rotate the Petri dish allowing the biomanipulator to vary the angle of the end-effector about the vertical z -axis, required a large aperture to allow the 32 mm diameter objective 15 mm of motion along x , y , and z axes. Secondly, a further design requirement was specified to minimize the amount of mass supported by the z -axis to 15 kg. During the component selection stage, few rotation stages satisfied the large aperture requirement and many stages including direct drive stages were too large and too heavy which reduced the ability to provide a rigid structure to support the stage. Newport Corporation, provided the URS-150, a large 90 mm aperture, worm drive, low profile, 3.4 kg, DC servo brush motor that was housed

in a very low height 38 mm package. This manufacturer states their worm-gear on this style of rotation stages is an improved design providing limited backlash-free operation over the span of 20,000 hours before mechanical failure.

The β -stage, required to rotate the end-effector about the y-axis did not have strict weight or size restrictions, therefore, a smaller version of the α -axis rotation stage, the URS-75, was chosen to ease integration of components.

3.6 Cantilever Beam

In order to interface the mechanical system to the optical system, a cantilever beam was required to provide a rigid support structure to hold the α -stage and Petri dish over the optical axis of the microscope assembly. The cantilever beam had several design limitations imposed by the selection of the Aerotech ALS1000 stage and the BLMC-142 linear direct-drive motors, the microscope assembly, and the design goals of the system. These are specified in Table 3.3. The resultant center of gravity of the

Table 3.3: Cantilever Beam Design Limitations

Device	Limitation
Linear stage assembly	Resultant center of gravity
Microscope assembly	Physical obstruction
Design requirement	Maximum deflection $\leq 3 \mu\text{m}$
Design requirement	z -axis maximum payload less than 15 kg

cantilever beam was required to satisfy the manufacturer cantilevered load capability shown in Figure 3.5 including vertical and horizontal cantilever loading restrictions. L_{SC} is the distance from the stage center when the stage face normal is coaxial with the gravity vector, and L_{VC} is the distance from the stage center when the stage face normal is perpendicular to gravity vector. Both L_{SC} and L_{VC} display working operational limits recommended by Aerotech Inc. when using a cantilevered load and the aim in the construction of the beam was to restrict the value of both L_{SC} and L_{VC} to within the range of 50 to 75 mm in Figure 3.5. This ensured minimal wear

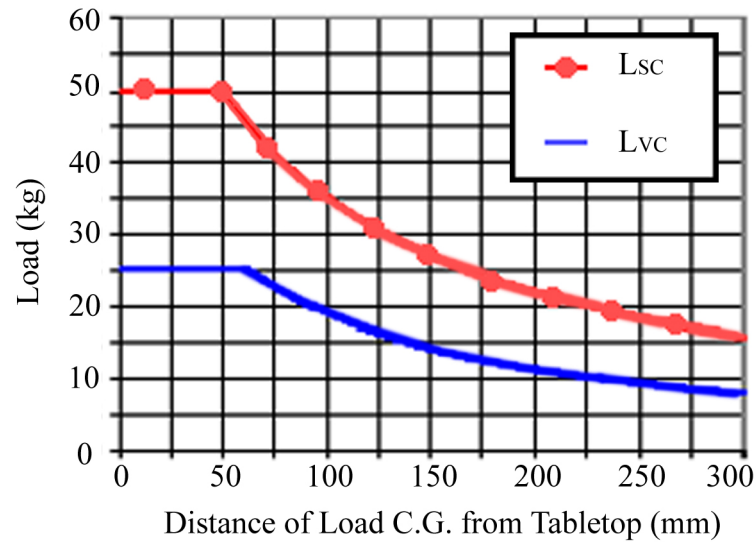


Figure 3.5: ALS1000 cantilevered load capability (Image adopted from [49])

on the linear stage bearings and allowed some flexibility in the addition of mass, or moving the cantilever beam further out from the center of the stages.

A third design goal was to provide a rigid cantilever beam structure assembly with a mass of less than 15 kg and to limit the maximum deflection obtained in finite-element modeling to 3 μm under the assumption of relatively low stage acceleration.

3.6.1 Computer-Aided Modeling of Cantilever Beam

A computer-aided model (CAD), shown in Figure 3.6, was created in Pro/ENGINEER to aid the placement of system components and exploit the finite element analysis (FEA) tools in Pro/MECHANICA™ to obtain a 3 μm or less beam deflection. The linear stages were required to be placed in such a manner to allow 15 mm of motion in any direction. Using this placement the distance from the center of the linear stage assembly to the optical axis was 242 mm as seen in 3.7. The minimum beam length to support the α -stage was 242 mm plus an additional 82.5 mm to support the remainder of the rotation stage housing. The beam was decided to be modeled as a solid Aluminum alloy 6061 C-channel with a top cover. Several performance

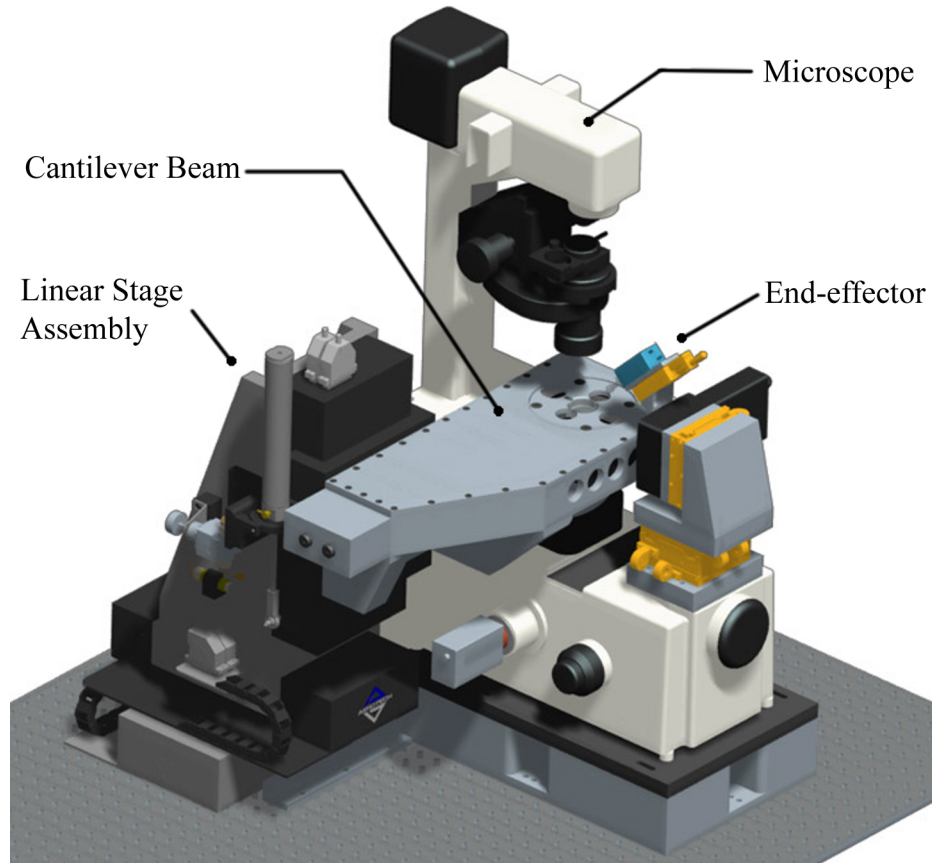


Figure 3.6: CAD model of the biomanipulator.

trade-off existed in the development of the model, and can be identified using the simple equation for the displacement of an intermediate load on a cantilever beam,

$$displacement = -\frac{Px^2}{6EI} \cdot (3x - a), \quad (3.7)$$

where P is the load on the beam, x is the length of the beam, E is Young's Modulus, a is the location of the load P on the beam, and I is the moment of inertia. The moment of inertia of the beam can be approximated as a square channel,

$$I_y = \frac{2sb^3 + ht^3}{3} - AC_x^2, \quad (3.8)$$

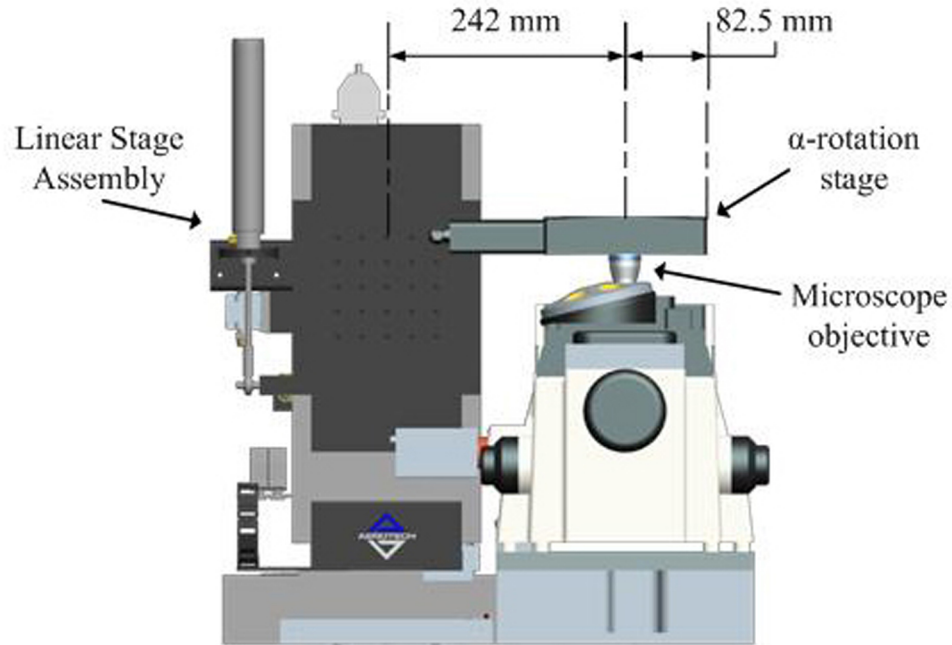


Figure 3.7: Linear stage assembly placement: front view.

where the area A is,

$$A = 2sb + ht, \quad (3.9)$$

and b , s , C_x , and t are defined in Figure 3.8. Noting eq. (3.7), eq. (3.8), and eq. (3.9) it is apparent that keeping the height of the side-walls, b , and thickness of the floor of the beam, t , is more effective than increasing the thickness of the side walls of the C-channel. Figure 3.9 shows the obstruction between the cantilever beam walls and the microscope housing, as well as between the cantilever beam base and the objective turret assembly. This limited the total freedom of design which limited the thickness of the cantilever beam wall. The respective values are listed in Table 3.4, where d_{sy} is the allotment for motion and a working clearance between obstructions, d_{max} is the maximum width possible for the cantilever beam, d_{sx} is the desired working clearance between the top and bottom surface of the cantilever beam and the microscope structure, d_{obj} is the height of the objective, and h_{tc} is the maximum clearance between the base of the objective and the bottom

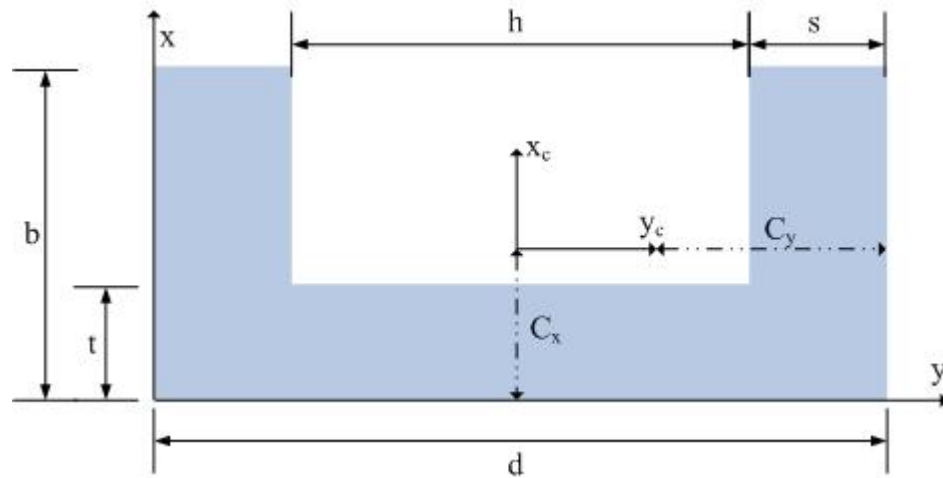


Figure 3.8: C channel dimensions

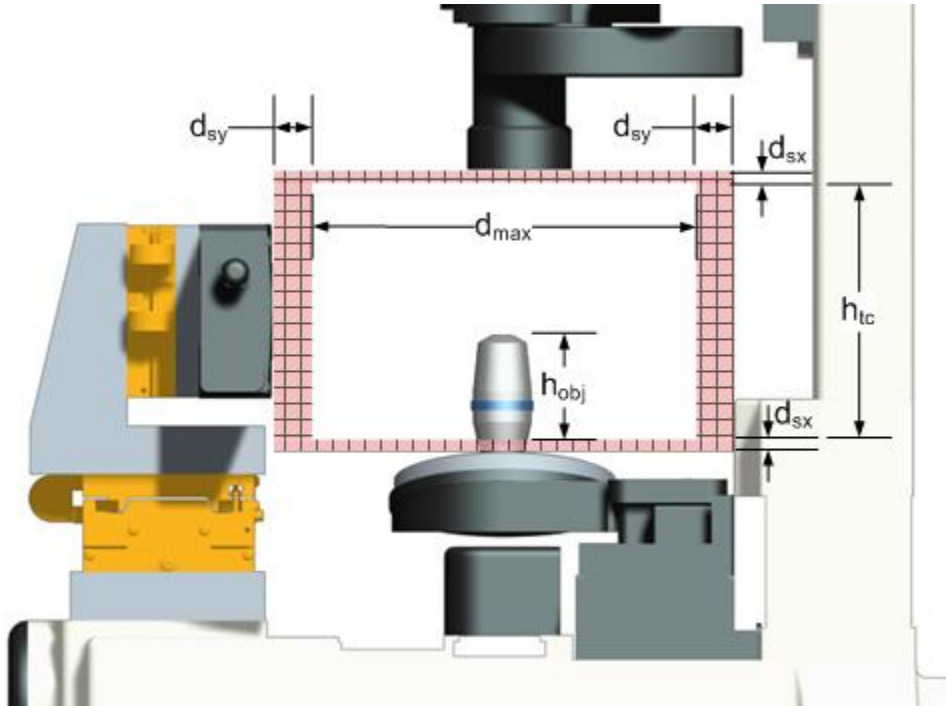
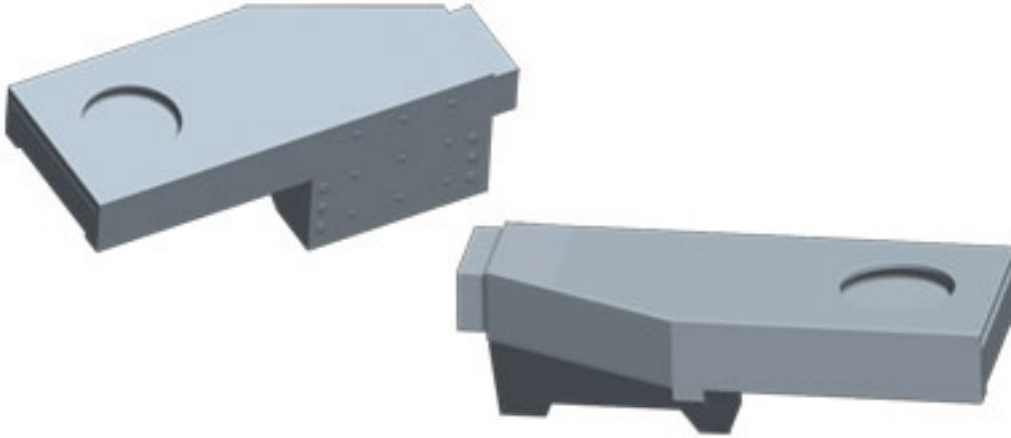


Figure 3.9: Obstruction zones for cantilever beam

surface of the condenser. Therefore, Pro/MECHANICA™, a Pro/ENGINEER™ finite element analysis tool was used to obtain an approximation for the deflection and the location of the resultant center-of-gravity through the use of solid modeling. The solid model was influenced by several factors including obtaining a deflection of less than 3 μm , ensuring the resultant center-of-gravity was within the manufacturer's

Table 3.4: Dimension Values for 3.9

Dimension	Value
d_{sy}	20 mm
d_{max}	191.5 mm
d_{sx}	5 mm
d_{obj}	57 mm
h_{tc}	160 mm

**Figure 3.10:** CAD solid model used for FEM analysis

specified tolerance (L_{SC} and L_{VC}), and mass less than 15 kg. The solid model of the cantilever can be seen in Figure 3.10, and is constrained at the interface between the z-axis linear stage face and the mating section of the cantilever beam (back side of model shown). The solid model was optimized using Pro/MECHANICA™ Wildfire 2.0. The height of the C-beam, b , was maximized to 60 mm ensuring no contact with the microscope assembly during routine operation. This height also ensured access for the operator to place Petri dishes on the inspection table without damaging the valuable contents. Table 3.5 shows the limits and the optimized values obtained. Table 3.6 displays the specifications chosen for the 5-DOF biomanipulator and the specifications achieved after the optimization converged to the following values.

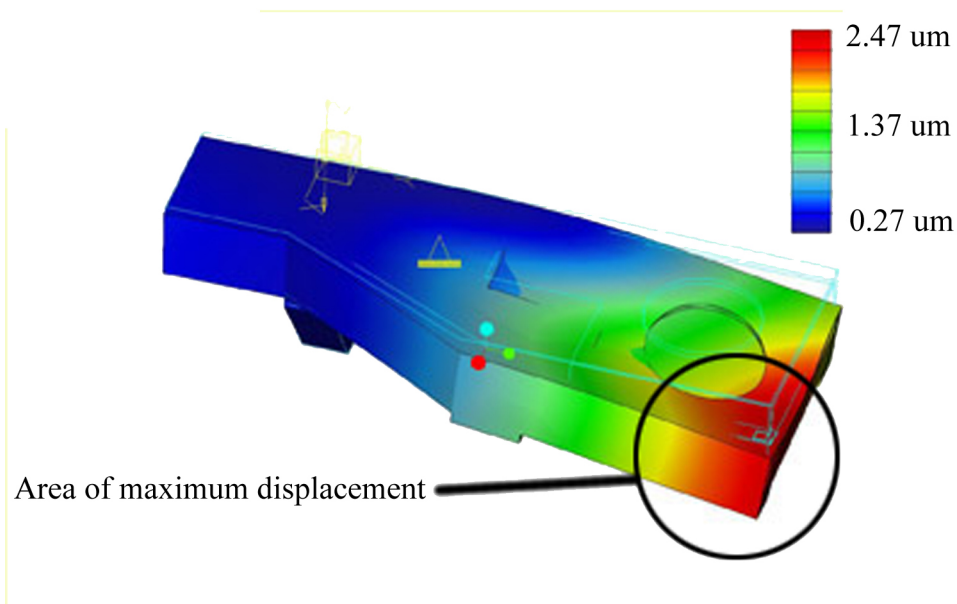
The optimization converged on the limits above and provided the desired values. Pro/MECHANICA™, provided a $2.75 \mu\text{m}$ maximum displacement and the deformed model is shown in Figure 3.11 indicating the regions of greatest displacement. Figure

Table 3.5: Cantilever Constraints and Optimized Values

Constraint	Min	Max	Optimized
$s(\text{sidewallthickness})$	6.35 mm	14.75 mm	7.77 mm
$t(\text{floorthickness})$	6.35 mm	15 mm	14.7 mm
$\text{CounterBalanceLength}$	10 mm	300 mm	300 mm
$\text{FloorApertureDiameter}$	90 mm	130 mm	130 mm

Table 3.6: Specifications of the Biomanipulator Cantilever Beam

Device	Required	Achieved
x - y -axis workspace	15 mm x 15 mm	16.5 mm x 16.5 mm
z -axis total load	≤ 15 kg	14.7 kg
Cantilever Beam Deflection	≤ 3 μm	2.74 μm
CoG _X center of stage on \hat{x} axis	≤ 75 mm	68 mm
CoG _Y center of stage on y -axis	≤ 75 mm	31 mm

**Figure 3.11:** Final cantilever assembly - the corner closest to the lower right corner of the image experiences a maximum displacement of 2.74 μm .

3.12 provides the final implemented version in exploded view.

3.7 Motor Controller Sub-assembly

The motor controller is the hub of the mechanical control system and is necessary to interpret signals from the motors that provide information regarding position,

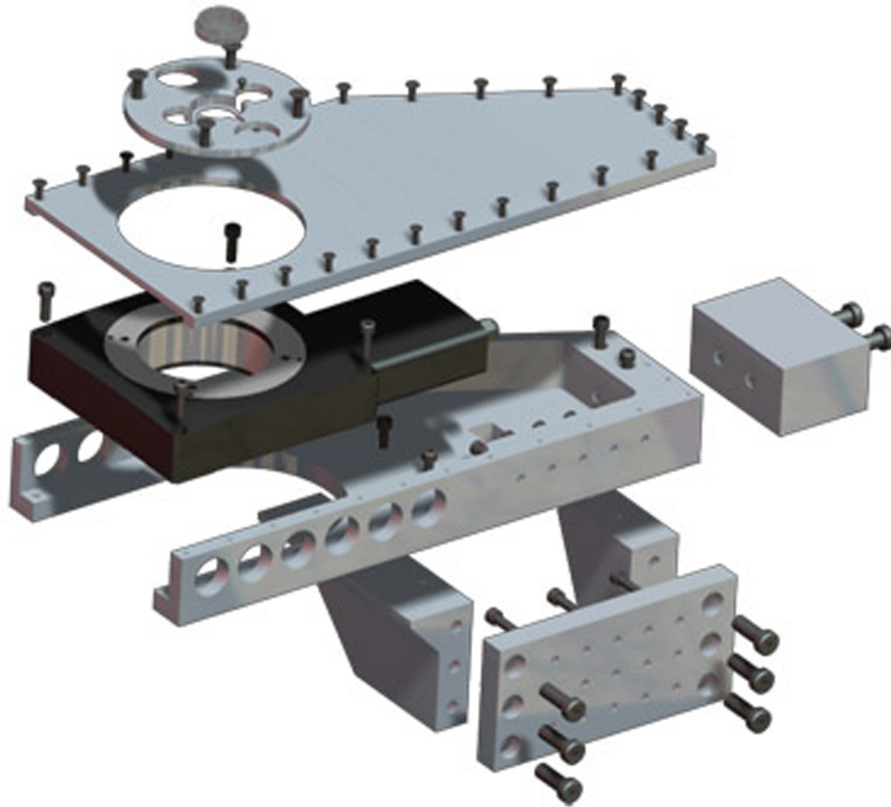


Figure 3.12: Cantilever beam assembly

fault conditions, and to provide closed-loop feedback to ensure stability. The motor controller's other key responsibility is to accept a command signal from a user or computer and provide signals to second-stage equipment such as amplifiers which provide the voltage to drive the motor.

The biomanipulator required a flexible controller such that it was not bound to only five degrees-of-freedom and allowed multiple vendor's equipment to be integrated into the system. Therefore National Instrument's PCI-7350™ line of motor controllers was chosen as the controller for the biomanipulator. The PCI-7358™ series of controllers offered a wide range of flexibility and provided interfaces for up to 8 axes of motion control for either DC brush or brushless motors, and provides closed-loop PID control at 125 μ s update intervals. Furthermore, National Instruments provides a full application programming interface (API) in National Instrument's native Lab-

VIEW™ Visual Interface (VI) programming language which has been evolving for the past two decades.

3.8 Summary

The first iteration of the design process for the physical framework of the biomaniipulator was completed. A 5-DOF conceptual model was created for the purposes of single-cell microinjection using three high-precision linear direct drive stages for linear translation (x , y , and z axes), and two rotation stages providing changes in end-effector orientation (α , and β axes). A custom designed aluminum 6061 cantilever beam was created to hold the α -stage over the microscope base and was modeled in Pro/ENGINEER™. To ensure the displacement of the cantilever beam conforms to the maximum 3 μm displacement, the mechanical assembly provided a maximum displacement of less than 3 μm , which was verified using the finite element analysis package in Pro/MECHANICA™. Sub-micron mechanical resolution for the linear stages is rated by the motor manufacturers at 0.04 μm and optical resolution is theoretically determined to be 0.56 μm . Consequently both optical and mechanical resolution criteria outlined in Section 3.2 were satisfied. The ability to observe thin and transparent biological specimens is achieved by using a differential interference contrast microscope and a high-speed CMOS image sensor. Images are then sent via firewire to a personal computer running NI LabVIEW™ and are processed by computer vision algorithms. Output responses are then passed to a high-performance National Instruments PCI-7308 motion controller. The motion controller tracks positional data from the motor encoders, provides the drivers with the correct velocity commands, and features closed loop PID feedback occurring at an update rate of 125 μs .

Chapter 4

Electroporation

4.1 Overview

State-of-the-art research in cell biology, biochemistry and genetics require a fast and effective means of inserting foreign materials into cells. Electroporation, used in academic and industrial applications achieves a fast uptake of macromolecules into cells and eliminates the need to pierce the cell membrane with a microcapillary. This is accomplished by creating small temporary openings in the cell membrane by applying an electric field. Successful electroporation has been documented for more than two decades [37] [50] [51], and success rates of up to 80 percent have been achieved [36] [52]. Electroporation has been used in the treatment of cancer cells (electrochemotherapy) [53] [54], insertion of genes (electrogenetherapy) [55], cell morphology [3] [36], and delivery of other substances such as amino acids and fluorescent dyes. Successful electroporation has been achieved on and not limited to cell types including mouse and rat neuronal blastoma x glioma hybrid [56], Chinese hamster ovarian cells [50] [57], mouse embryonic stem cells [58], human cervical cancer cells [59], and mouse lyoma cells [55].

Single-cell electroporation (SCE) is a technique that was created for single-cell microinjection and applies the same principles of conventional electroporation techniques on a much smaller scale. This involves restricting the electric field with a

microcapillary to affect the membrane of only one cell, allows visual analysis of the cell during the procedure, and potentially uses the reagents more efficiently. In this chapter an overview of electroporation is described. A description of the commercial single-cell electroporator Axoporation 800A™, created by Axon Instruments, is described in operation and how it was implemented into the biomanipulator.

4.1.1 Electroporation Theory

Electroporation is a method that uses an electric field to temporarily modify the structure of the cell membrane. It is less invasive than conventional methods such as microcapillary injection; however, the science of electroporation is not fully understood.

The cell membrane is the key to the mechanism of ionic and molecular transportation into and out of the cell. It consists of a double layer of phospholipids that provide structural integrity and a permeability barrier. A phospholipid consists of a glycerol core containing two adjoining molecular structures. One side is linked to two hydrophobic (water-disliking) fatty acid-derived tails and on the other side is linked to a hydrophilic (water-liking) phosphate ester link. In an aqueous solution the hydrophilic heads are orientated towards the aqueous solution while the hydrophobic tails minimize contact by orientating away from the aqueous solution. These two thin shells of phospholipids group together forming the bilayer. The cell membrane is permeable to some molecules including oxygen, carbon dioxide, and water; however, other molecules must pass through the protein channels that are dispersed throughout the cell membrane or use techniques such as electroporation.

In the presence of an electric field, the lipids undergo a temporary reconfiguration and temporary openings in the membrane occur [60] causing water to be displaced into the openings. The phospholipids adjacent to the channel change the orientation of the hydrophilic head in the direction of the displaced water creating a temporary stable opening. Once the electric field is removed, the phospholipid bilayer returns

to the original configuration. It has been demonstrated that if the electric potential is too high or the electric field is kept on for too long the cell membrane integrity collapses and the cell is destroyed.

A spherical cell is subjected to an external electric field, a potential difference exists across the membrane. At low-frequency electric fields the solution of the Laplace equation provides the potential difference across the cell membrane in the direction of the electric field \mathbf{E} [61] [51],

$$\Delta V = 1.5RE|\cos\theta|, \quad (4.1)$$

where ΔV is the difference in potential, R is the radius of the cell, E is the electric field, and θ is the polar angle between the cell radial vector and the electric field vector.

Reference [50], adds further detail by taking into account the conductivities of the cell and its environment. The modified induced electric potential V_{ind} is defined as,

$$\Delta V_{ind} = -1.5Rf(\lambda_m)E|\cos\theta|. \quad (4.2)$$

The additional function term $f(\lambda_m)$ can be expressed in terms of the membrane thickness, cell radius and the conductivities of the membrane, cell interior, and the surrounding solution. The relevance for eq. (4.1) and eq. (4.2) for this work suggests the smaller the radius of the cell the greater the electric field required to achieve permeabilization. Furthermore, the strength of the electric potential is strongest at the location where the radial vector is parallel with the electric field lines, or directly between the electrodes. Therefore, at specific intensities of electric field strength, the cell membrane will be permeabilized first in the locations directly between the two electrodes or when $\cos\theta = 1$. Reference [62] has shown the permeabilization occurs to a greater extent on the side of the cell facing the negative electrode, and [62] [63]

has shown that the extent and degree of permeabilization is controlled by the amplitude and duration of the applied pulse. Furthermore, even large molecules such as antibodies and dextrans have been successfully injected into cells by electroporation [52].

4.2 Single-cell Electroporation

Single-cell electroporation is an efficient adaptation of large-scale electroporation. Some of the main differences from large-scale electroporation include a lower level of applied electric potential, the distance between the electrode and the cell membrane, and the ability to observe the effects on cells while electroporation takes place. Furthermore, in some situations it is possible to verify the success shortly after the procedure, and the cell viability. There have been several variations of devices that have been built for single cell electroporation and can be classified into two types including static cell and moving electrode, or mobile cell, static electrode. The first method involves moving one or both electrodes to the cell for electroporation and allows flexible access to both cell position and orientation.

In literature, [64] developed one of the earliest known single-cell electroporators that uses two carbon-fiber electrodes placed opposite to each other far enough to allow a single cell in between them. An electrolyte filled capillary, similar to the one used in this work, was developed by [35] [3] [36] for the purposes of replacing methods that combined the biomolecules to be delivered within the surrounding medium. The second method involves moving a cell to two stationary electrodes that are placed very close together. Reference [33] developed an integrated single-cell electroporator on a chip using standard silicon fabrication techniques. A similar device using integrated perfusion channels to trap cells in one channel and deliver material from a second channel was implemented by [59].

Electroporation by micropipettes and an electrolytic solution is an effective method

in delivering material to single cells. They are now commercially available and are similar to patch-clamp devices used in physiology. The commercially available, Axoporation 800A™ by Axon Instruments, is used in this work and based on experimental techniques by [35]. This method achieves localized electroporation by filling a microcapillary with an electrolyte solution and the molecules to deliver through the cell membrane. The electrode used in the microcapillary is created by coating a thin 0.25 mm silver wire by placing it in bleach for approximately 20 minutes. The coated wire is placed in a single barrel microcapillary that has been loaded with PBS and the molecules desired to be injected into the cell. The second electrode, known as the bath ground, is similarly coated and placed within the same solution the cells exist in. The electrode, in single-cell electroporation, serves two purposes. As in conventional electroporation, the first purpose is to induce an electric field to create temporary permeations in the cell membrane. The second purpose is to drive the molecules in the electrolytic solution away from the electrode inside the microcapillary toward the temporarily permeable membrane.

The microcapillary tip, which is approximately 1 μm to 3 μm in diameter, is pressed up against the cell membrane which creates membrane tension lowering the voltage required for electroporation [4]. At that time the electric field pulses are activated causing a reconfiguration of the phospholipid bilayer creating the temporary openings in the cell membrane. Like charges within the micropipette are repelled from the electrode through the membranes by Coulomb force. This effect is known as electrophoresis, and involves the motion of electrically charged particles in a fluid due to an induced electric field as follows,

$$\mathbf{F} = q\mathbf{E}, \quad (4.3)$$

where \mathbf{F} is the Coulomb force that is applied to a charge of quantity q in a directional

electric field \mathbf{E} .

Electro-osmosis is responsible for moving the remaining particles of lesser or opposite charge of the electrode towards the cell membrane for delivery, and can be described by Fick's First law [50],

$$\frac{dn_c}{dt} = -D_m S_m \frac{dc_m}{dx} \quad (4.4)$$

where n_c is the molar amount of the transported molecules in an enclosed volume, c_m is the concentration of the deliverable molecule, and D_m is the diffusion coefficient. S_m is the surface of the membrane that is permeabilized.

The Axoprotator 800A consists of the circuit in Figure 4.1. R_e is the resistance of

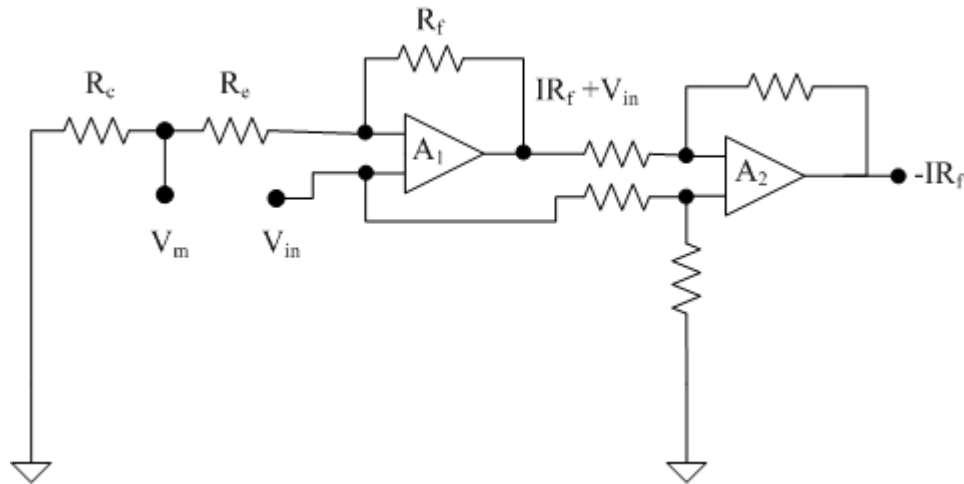


Figure 4.1: Electroporator voltage clamp circuit

the electrode, and R_c is the cleft resistance. The input voltage V_{in} exists at both the positive and negative inputs of the operational amplifiers, and the voltage delivered to R_c can be calculated based on the equation for a voltage divider as shown in eq. (4.5). R_c is increased as the micropipette tip further indents the cell as shown in Figure 4.2.

$$V_c = V_{in} \frac{R_c}{R_c + R_e} \quad (4.5)$$

The second amplifier in the circuit diagram subtracts the command voltage and the

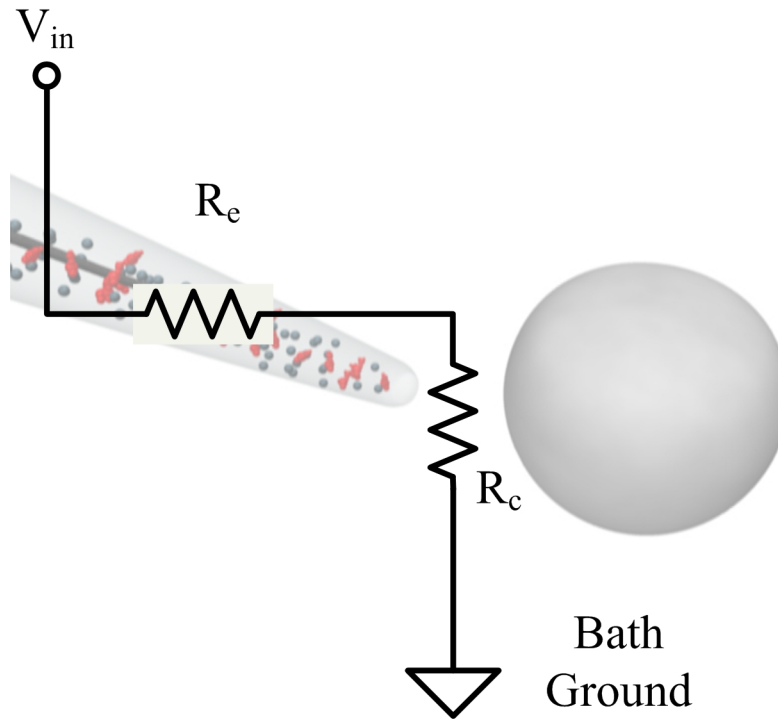


Figure 4.2: Voltage divider created between the SCE electrodes

result is a measure of the current flowing through the micropipette. The Axoprotector 800A™ provides a measurement of the current (1V per A) and voltage (0.1 Volts per 1 Volt) which allows the increase in resistance to be determined. At the instant when the correct increase in resistance is achieved a transistor-transistor-level (TTL) high signal is automatically generated and activates the electric field pulses. It is important to note that the location of the opposite electrode (the bath ground) is not important. Reference [5] has demonstrated that the electric field lines are highly concentrated at the tip of the electrode and therefore require the tip to be placed against the cell membrane.

4.2.1 Applied use of the Single-cell Electroporator

Single-cell electroporation will commence by adhering mouse myeloma to the bottom of a high-quality 35mm, 0.17 mm glass bottom Petri-dish with poly-L-lysine

(WillCo-Dish™, Model GWSt-3522). SCE was carried out using the Axon Axopora-
tor 800A™, a commercially available single-cell electroporator shown in Figure 4.3.
The micropipette, shown in Figure 4.4 consists of a thick wall microcapillary pipette



Figure 4.3: Axon Axopora 800A™ single-cell electroporator: headstage and micropipette assembly (left), and the digital console display (right).

with outside diameter of 1.5 μm , an inside diameter of 1.12 μm , and tip size is approximately 1 μm in diameter. Micropipettes were fabricated using a Sutter P-87™ automated pipette puller with settings according to Table 4.1.

Table 4.1: Settings for the Sutter P-87™ Automated Pipette Puller

Line	Heat	Pull	Velocity	time
1	Ramp + 7	0	28	255
2	Ramp + 7	0	28	255
3	Ramp - 4	0	31	255
4	Ramp - 58	0	31	255

The shape of the pipettes used during SCE were identical to those used for patch-clamp experiments, and is shown in Figure 4.4. A micropipette tip used for piercing the membrane is shown in Figure 4.5 (left), and the micropipette tip used for SCE in Figure 4.5 (right). The shape of the micropipettes used for SCE provide additional structural strength eliminating visible tip motion during visual servoing. The images

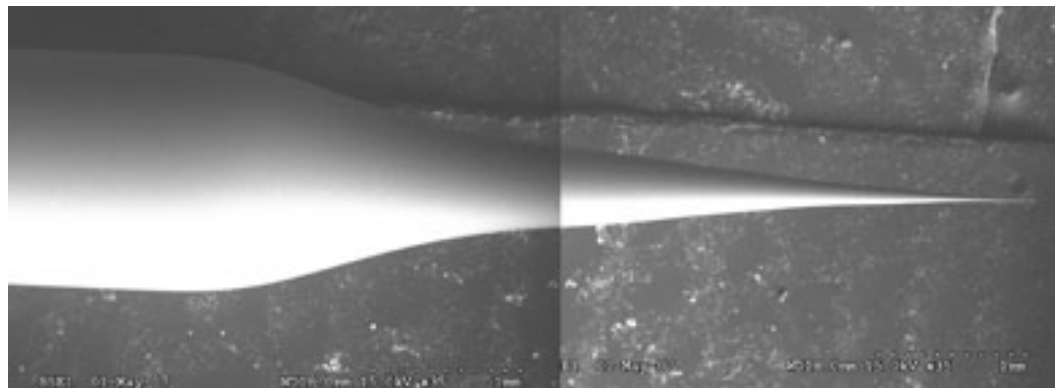


Figure 4.4: A side view of the micropipette shape at 35 times on the SEM.

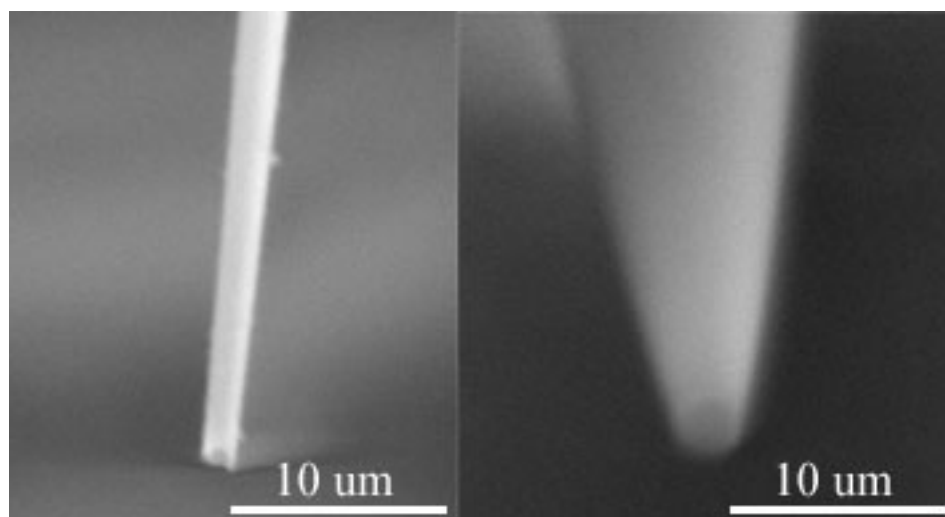


Figure 4.5: A comparison of tip shapes between microinjection pipettes (left), and SCE pipettes (right).

in Figures 4.4 and 4.5 were taken by the author using a SEM. The microcapillary is loaded with phosphate buffered saline and 1 g per L of a fluorescent dye known as Alexa Fluor 488™. The micropipette tip is positioned within several microns of the cell membrane using computer vision and robotic motion. Once this position is obtained the combination of the resistances, R_e and R_c is measured and the pipette is slowly advanced toward the center of the cell. Once a 33 percent increase is obtained in the resistance measurement the electric field will be applied, and the fluorophore will enter the permeated cell membrane. Successful verification will be done manually and confirmed by visual inspection using epi-fluorescence illumination. If the electroporation is successful the fluorophore will appear as an evenly distributed bright illumination within the cell membrane and the membrane will appear intact (see Figure 1.1).

Due to the unique nature of cells, individual parameters pertaining to the single-cell electroporator such as pulse train frequency, duty cycle, voltage level will be obtained through experimentation first.

Chapter 5

Biomanipulator Control

5.1 Biomanipulator Control Problem Definition

An autonomous biomanipulator must be able to replicate human actions in order to complete biomanipulation tasks such as microinjection of mammalian cells. In this work, using computer control, it is necessary to visually identify a cell while scanning a Petri dish, track the changes the target undergoes from commanded motion of the stage, and move the cell within several micrometers of the end-effector tip. This requires a well known technique called visual servoing [26] which surfaced in literature less than three decades ago. Visual servoing provides a dynamic response to observed changes in captured image data.

5.2 Image Based Control: Visual Servoing

A taxonomy of visual servoing was outlined by [6], and systems are classified into four categories including (i) dynamic position-based, look-and-move structure (DIBLM), (ii) position-based look-and-move structure (PBLM), (iii) position based-visual servoing (PBVS), and (iv) image-based visual servoing (IBVS). The biomanipulator in this work, according to [6], can be described as a DIBLM system. The biomanipulator uses a joint-level controller, the NI-7350™, to accept set-point commands. This is classified as a hierarchical system which accepts position and or velocity com-

mands as opposed to a direct-visual servo system [27] which provides an error output signal only. Furthermore, the biomanipulator computes error according to image features only, as opposed to defining the errors in task-space according to a physical representation. This system has several advantages to systems that are defined as position-based visual servo control (PBVS), and image-based visual servoing system (IBVS). Firstly, calculating the error in feature space eliminates errors due to calibration. Secondly, using a joint-level controller removes the need to contend with low sampling rates due to the vision system and creates an ideal axis-interface for vision control. Therefore, using the DIBLM structure, feature points of the cell $f(u, v)$ in the current captured image are moved with respect to the end-effector which is calibrated to the center of the image plane. The objective of the main task is to bring these feature points to a desired location, the end-effector or other location in the image. This task is defined as the error function \mathbf{e} , which is a function of the image features but defined in terms of joint space variables.

Two criteria required in this process is to drive \mathbf{e} to zero by defining motion with respect to joint coordinates and issuing commands to the joint controller. To accomplish this task, it is necessary to define the image Jacobian which is a linear transformation of coordinates of r , in task space, to f in feature space [27],

$$\dot{f} = J_v(r) \cdot \dot{r} \quad (5.1)$$

where \dot{f} is the rate of change of the image features, \dot{r} is the velocity of the cell moving with respect to the end-effector, and $J_v(r)$ is the image Jacobian. In the

biomanipulator the joint space vector $\dot{\mathbf{r}}$ is defined as,

$$\dot{\mathbf{f}} = \begin{bmatrix} \dot{x} \\ \dot{y} \\ \dot{z} \\ \dot{\theta}_\alpha \\ \dot{\theta}_\beta \end{bmatrix} \quad (5.2)$$

The image Jacobian relates the rate of change of the features in image space with the rate of change in task space which is typically joint space. Therefore, a change task space causes a change in image space,

$$\Delta \mathbf{f} = J_v \cdot \Delta^c x_t, \quad (5.3)$$

or in terms of the Jacobian,

$$J_v = \frac{\Delta^c x_t}{\Delta \mathbf{f}}. \quad (5.4)$$

As a function of the joint space vectors,

$$J_v(\mathbf{r}) = \frac{\partial \mathbf{f}}{\partial \mathbf{r}} = \begin{bmatrix} \frac{\partial f_1(\mathbf{r})}{\partial r_1} & \frac{\partial f_1(\mathbf{r})}{\partial r_2} & \cdots & \frac{\partial f_1(\mathbf{r})}{\partial r_m} \\ \frac{\partial f_2(\mathbf{r})}{\partial r_1} & \frac{\partial f_2(\mathbf{r})}{\partial r_2} & \cdots & \frac{\partial f_2(\mathbf{r})}{\partial r_m} \\ \vdots & \vdots & \ddots & \vdots \\ \frac{\partial f_k(\mathbf{r})}{\partial r_1} & \frac{\partial f_k(\mathbf{r})}{\partial r_2} & \cdots & \frac{\partial f_k(\mathbf{r})}{\partial r_m} \end{bmatrix} \quad (5.5)$$

where m is the dimension of the task space, and k is the number of image features.

5.3 Camera Model

In order to relate the image space to task space it is necessary to define a suitable camera model. The camera model is the interface between the physical hardware and the interpretation of the digital image. Its purpose is to provide spatial information

using prior knowledge about the environment to interpret the image captured by the photo sensor. The following is the nonlinear perspective projection equation describing a point $P(x, y)$ with respect to the camera coordinate frame that is projected onto the image plane,

$$\begin{bmatrix} u \\ v \end{bmatrix} = \frac{L_{focal}}{z} \begin{bmatrix} x \\ y \end{bmatrix}, \quad (5.6)$$

where u and v represent the coordinates of the point on the two-dimensional image representation. This relationship between image space and task space can also be related to the velocity of a point P attached to a target cell t about the camera frame

$${}^C \dot{\mathbf{P}} = {}^C \omega_t {}^t \mathbf{P} + {}^C \mathbf{T}_t, \quad (5.7)$$

where ${}^C \dot{\mathbf{P}}$ is the velocity of point P with respect to the camera frame, ${}^C \omega_t$ is the angular velocity of the target with respect to the camera frame, ${}^t \mathbf{P}$ is the point that is fixed to the cell and ${}^C \mathbf{T}_t$ is the velocity of the target with respect to the camera frame. Expanding eq. 5.7 in the case of 6-DOF give,

$$\dot{x} = z \cdot \omega_y - \frac{z}{L_{focal}} \cdot v \cdot \omega_x + T_x, \quad (5.8)$$

$$\dot{y} = \frac{z}{L_{focal}} \cdot u \cdot \omega_z - z \cdot \omega_x + T_y, \quad (5.9)$$

$$\dot{z} = \frac{z}{L_{focal}} \cdot (v \cdot \omega_x - u \cdot \omega_y) + T_z. \quad (5.10)$$

Taking the derivative of eq. (5.6) with respect to u and v , and rewriting in matrix form gives,

$$\begin{bmatrix} \dot{u} \\ \dot{v} \end{bmatrix} = \begin{bmatrix} \frac{L_{focal}}{z} & 0 & \frac{u}{z} & \frac{u \cdot v}{L_{focal}} & \frac{L_{focal}^2 + v^2}{L_{focal}} & -v \\ 0 & \frac{L_{focal}}{z} & -\frac{v}{z} & \frac{-L_{focal}^2 - v^2}{L_{focal}} & \frac{u \cdot v}{L_{focal}} & -u \end{bmatrix} \begin{bmatrix} T_x \\ T_y \\ T_z \\ \omega_x \\ \omega_y \\ \omega_z \end{bmatrix}. \quad (5.11)$$

Eq. (5.11) provides provides the general case for 6-DOF. Several simplifications can be made given the configuration of the 5-DOF biomanipulator, the differences in required DOF in several tasks, and the relationship between the camera placement with respect to the image scene. Firstly, the camera is mounted such that the camera focal axis can be approximated as being collinear with the normal of the surface of the Petri dish. Furthermore, since the field-of-view of the image is quite small in comparison to the distance from the camera to the scene a simplification to perspective projection known or orthographic projection can be made as follows,

$$\begin{bmatrix} u \\ v \end{bmatrix} = s \begin{bmatrix} x \\ y \end{bmatrix}. \quad (5.12)$$

Where s represents the constant distance from the image sensor to the image plane.

In this work, the depth of the scene (cell culture) is shallow compared to the distance from the scene to the objective lens. This is approximately on the order of 1000 times greater in magnitude. Considering only linear motion on the horizontal

plane with a rotation about the z -axis, eq. (5.11) simplifies to

$$\begin{bmatrix} \dot{u} \\ \dot{v} \end{bmatrix} = \begin{bmatrix} s & 0 & -v \\ 0 & s & -u \end{bmatrix} \begin{bmatrix} T_x \\ T_y \\ \omega_z \end{bmatrix}, \quad (5.13)$$

which is used for general motion of the biomanipulator.

5.4 Control Method Error Function

The control method used is based on reducing the error term e , or the difference in the set-point position from the current position of the cell. The control method used is based on the implementation of [34, 10], and entails a minimization of the error function which places a weight on the difference in desired position and the control input with respect to the state equation,

$$x(k+1) = x(k) + \frac{1}{f_s} J_v(k) r(k), \quad (5.14)$$

where $x(k)$ is the current state, $x(k+1)$ is the next state, $r(k)$ is the velocity, in task space coordinates, of the target moving toward the desired position, and f_s is the sampling frequency of the control loop. The error e function is defined as,

$$e(k+1) = [x(k+1) - x^*]^T Q [x(k+1) - x^*] + r^T(k) L r(k), \quad (5.15)$$

where x^* is the desired location for the cell to move, Q and L are weighting functions for the positional error and the commanded input respectively. This function is minimized and solved with respect to $r(k)$ giving [10],

$$r(k) = - \left[\frac{1}{f} J_v(k) Q \frac{1}{f} J_v(k) Q + L \right]^{-1} \frac{1}{f} J_v^T(k) Q [x(k) - x^*]. \quad (5.16)$$

Upon driving the error term to zero, resulting in movement stopping, control will be changed from vision control to control based on impedance measurements from the electroporator. Velocity will be kept constant slowly increasing the impedance measurement due to the increase in resistance due to contact between the cell membrane and the micropipette tip. The control method will follow a sequential procedure resulting in one of several conditions,

1. The electroporation resistance is obtained,
2. The micropipette tip malfunctions, or
3. The micropipette tip overshoots the target.

If the required measurement is obtained, the electric field pulses will commence for only predetermined time according to previous manually obtained experimental results. The micropipette tip may malfunction during this procedure or during routine operation. Experimental results, obtained in [12], are used as a guideline. These observations indicated that an increase in resistance well beyond the required resistance for threshold indicates a clogged or dirty tip and dramatic reduction in measured resistance indicates a broken tip. Both conditions will flag an immediate response, and an operator will be alerted to inspect the tip conditions.

5.5 Computer Vision

5.5.1 Problem Realization

Detecting objects in images using digital sensors and computer algorithms is a difficult and usually computationally intensive. Adding further difficulty, pertaining to this work, is the need to detect thin and nearly transparent mammalian cells that are on the order of 10 to 20 μm in diameter with optics that present unique challenges. Some of these challenges arise from optical limitations such as artifacts or distortions

that are caused by the method of microscopy illumination such as differential interference contrast which causes the appearance of a shadow. Other hurdles are due to the limitations of achievable optical resolution, or the result of a busy environment causing cluttered images such as cell clusters. The intent of this section is to provide the methodology behind localization of cells, which refers to positively identifying a cell within the field-of-view. Secondly to provide an understanding on how to autofocus and track the motion of cells with respect to a point in the field-of-view. Finally the means by which to segment the cells which provides structure to objects or the environment located within the image.

5.5.2 Background Information

Differential interference contrast is a method of microscopy illumination used by human operators to perform single-cell microinjection. It exploits the difference in optical path lengths between two orthogonally, polarized wavefronts of light that are separated by a distance much smaller than the resolution of the microscope. These differences, caused by several stages of optical mechanisms, are converted into differences in contrast levels necessary to see cells. This illumination method provides a human operator an image that provides a three-dimensional like appearance providing some relief to discern small details. However, this solution is far from optimal for simple computer vision techniques to handle. The directional shadow-like effect reduces the ability to thresholding cells from their background, and border details are lost. In computer vision, localizing objects is defined as the ability to locate a particular object or objects within the field-of-view. Segmentation, refers to the ability of extracting edge information with respect to that object giving it physical structure.

In this work, several tasks required the use of computer vision for routine operations. These include the following,

1. Localization of a target cell,
2. Target tracking, while the target is moving, and
3. Determining the approximate boundary of the target with respect to end-effector location.

5.5.3 Localization Methods Used

Localization of mouse myeloma cells is accomplished through the trial of three different algorithms involving several steps. Firstly, the Laplacian of a Gaussian (LOG) is applied to a greyscale image. Automatic thresholding is applied to the pronounced edges located during the LOG using a well known auto-threshold operator developed by [65]. This step will reduce grey intensity values to binary pixel values and eliminate much of the background from the image. A morphological operator known as *close* is applied to fill in located boundaries. Shape matching using a simple image of a circle is then applied to locate cells.

The second method replaces the LOG function with one of the *de facto* standards in the computer vision community known as the Canny Edge detector [66], otherwise known as the optimal edge detector.

Finally, in contrast to the above edge detection methods, the last operation uses a simple greyscale template matching technique that applies a Gaussian filter in order to reduce noise and then searches the entire image for a high-correlation between a greyscale template of a cell and similar looking cells in the image.

5.5.4 Binary Shape Detection

Localization of cells was attempted using two different schemes, shown in 5.1 for comparison and selection of the most suitable method. The first algorithm uses mathematical operators and is known as the Laplacian of a Gaussian which is a linear operator, or meaning the image is convolved with a kernel. Initially a Gaussian filter

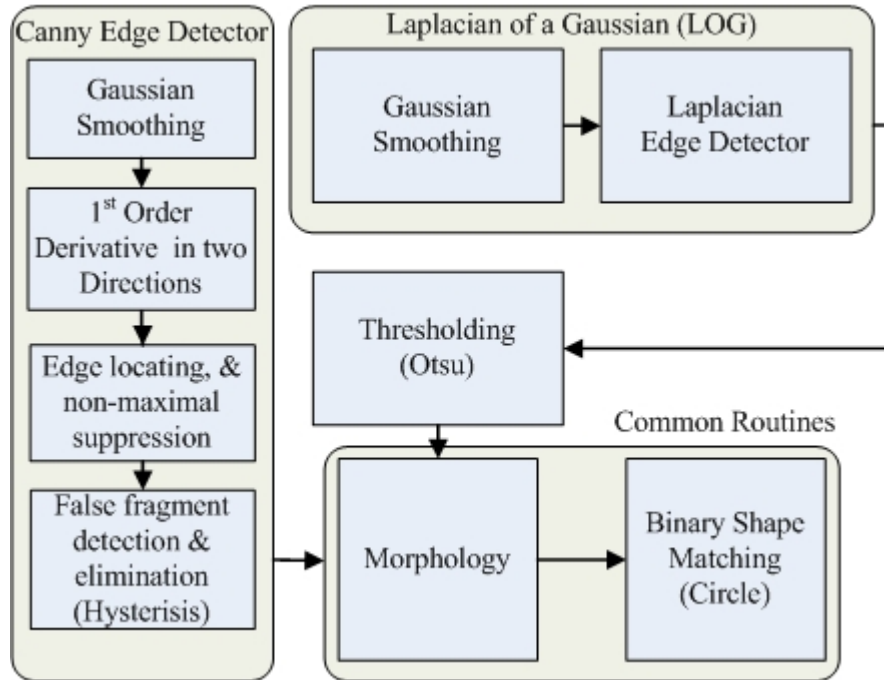


Figure 5.1: Algorithms for binary shape recognition

is convolved with the image resulting in smoothing. The Gaussian can be represented mathematically as [67],

$$G(u, v) = \frac{1}{2\pi\sigma^2} e^{-\frac{x^2+y^2}{2\sigma^2}}. \quad (5.17)$$

Table 5.1, is the image kernel representing eq. (5.17) which is convolved with the image. A Laplacian kernel is used to detect the edges by detecting zero crossing

Table 5.1: Guassian Kernel

1	4	7	4	1
4	16	26	16	4
7	26	41	26	7
4	16	26	16	4
1	4	7	4	1

points using the second derivative of the gradient intensities. The Laplacian can be represented mathematically by the following [67],

$$\nabla^2 f(x, y) = \frac{\partial^2 f}{\partial u^2} + \frac{\partial^2 f}{\partial v^2}, \quad (5.18)$$

and is represented by the kernel in Table 5.2.

Table 5.2: Laplacian Kernel

-1	-1	-1	-1	-1
-1	-1	-1	-1	-1
-1	-1	24	-1	-1
-1	-1	-1	-1	-1
-1	-1	-1	-1	-1

Automatic thresholding is applied using a well known auto-threshold operator developed by [65] which will change pixel values to either a one or a zero. This will leave a binary mapping of the image for analysis and will ensure a majority of the background is ignored. Several known issues exist with this method including discontinuous or fragmented boundaries about the cell. This is caused by similar intensities shared between cell borders and the background. The resulting discontinuities can be improved by using a morphological operator such as *close* followed by hole filling.

The second algorithm attempted uses the Canny edge detector, known as the optimal edge detector to locate the edges of the cells. Canny edge detection is based on three criteria (*i*) no edges are missed, (*ii*) edge points are well localized, and (*iii*) no edge is duplicated. Similar to the LOG, images are first smoothed using Gaussian smoothing to reduce the effects of noise. Edges are located by calculating the image gradient at each located edge site in two dimensions to locate areas at pixel sites with high spatial derivatives. Pixels that are not edges are eliminated using non-maximal suppression, and finally edge fragments are then eliminated using hysteresis.

5.5.5 Greyscale Template Matching

Our task makes the initial assumption there is some loosely structured arrangement of cells that are adequately spaced to avoid issues when dealing with cell clusters. Computation time is focused on relevant areas of interest by specifying a region-of-interest (ROI) limiting computations to a subset of the image captured. The initial localization of a target cell is done by template matching using a previously

acquired square image of a typical mouse myeloma cell (up to 128 by 128 pixels). The template image is passed over a search window in the most recent acquired image and a correlation score is determined. The score is based on the normalized correlation coefficient [68] and is described by,

$$C(m, n) = \frac{\sum_u \sum_v [f(u, v) - \bar{f}] [w(u - m, v - n) - \bar{w}]}{\left[\sum_u \sum_v [f(u, v) - \bar{f}]^2 \sum_u \sum_v [w(u - m, v - n) - \bar{w}]^2 \right]^{\frac{1}{2}}}, \quad (5.19)$$

where $C(m, n)$ is the score of the template located at image position (m, n) , $f(u, v)$ represents the image pixel intensity, $w(u - m, v - n)$ represents the template pixel intensity, \bar{f} and \bar{w} is the average intensity in the image search window and template respectively. High correlation scores indicate the location of the template object. This method is limited by real-time computational limitations such as size of the template and the search window.

A further benefit of template matching is the approximate centroid location is provided. The method is limited by real-time computational limitations such as size of the template and the search window. The second service that template matching provides is the ability to track an image based on these correlation values. An image of the localized cell is captured on the fly for this purpose. The distance the cell has traveled can be monitored through a method known as sum-of-squared differences (SSD). The basic premise behind SSD makes use of the fact that differences between sequential images are small, therefore, correlation can be done between the acquired template and the area about the last known location of the cell. The mathematical operation is defined as,

$$SSD = \sum_{i, j \in N} [g(u_1 + dv + i, v_1 + dv + j) - w(u_1 + du + i, v_1 + dv + j)]^2 \quad (5.20)$$

where g represents the image and w represents the template image. The distance, (du, dv) , chosen that scores the least value represents the best match and therefore

provides the best estimate for the distance the cell has moved.

5.5.6 Segmentation

Segmentation is required to approximate the initial distance from the cell membrane to the tip of the pipette, to allow the pipette to be positioned within a reasonable distance prior to switching to fine position control based on electrode resistance. The Hough transform was developed by [69] to detect lines and then generalized by [70] to find arbitrary shapes. With respect to biomanipulator devices, [10] used the Hough transform to locate the nucleus of a mouse oocyte.

The Hough transform is a method of locating straight lines, circles, and even arbitrary shapes in images. This differs from localization techniques, such that spatial information or geometry is provided by the segmentation algorithm. This information provides physical structure to the image data.

In this work, segmentation of the cell membrane needs only to be accurate enough to avoid collision with a suitable cell target and place the cell membrane within several μm of the micropipette tip (*i.e.* within 5 μm). The Hough transform is a suitable method for determining the approximate location of the perimeter of the cell membrane. This algorithm involves several image post-processing techniques seen before in Section 5.5.3. These steps include using the Canny edge detector to obtain an edge of pixels. It should be noted that the Canny edge detector consists of several image post-processing steps including: Gaussian smoothing to reduce noise, edge localization, non-maximal suppression to reduce thick edges to thin edges, and false fragment detection which eliminate false detected edges.

In order to determine the approximate radius of the cell three variables must be satisfied in eq. 5.21

$$(u - a)^2 + (v - b)^2 = r^2, \quad (5.21)$$

where a and b represent the image coordinates of the approximated center, and r

represents the radius of the circle.

The Sobel gradient operator convolution kernels shown in Table 5.3 and Table 5.4, is then applied to the image.

Table 5.3: Sobel Horizontal Gradient Kernel

-1	0	1
-2	0	2
-1	0	1

Table 5.4: Sobel Vertical Gradient Kernel

-1	-2	-1
0	0	0
1	2	1

The gradients provide the approximate orientation of the edge direction in eq. 5.22.

$$\theta = \arctan \left(\frac{G_y}{G_x} \right) \quad (5.22)$$

Furthermore, given that two directions exist for each value of θ ; however prior knowledge of the approximate location of the centroid of the cell from the template match during tracking eliminates one direction from the orientation calculation.

Once the orientation information is found, a space with dimensions the size of the search is assigned. Each pixel is processed and then using the orientation and the direction of the center a ray is drawn from the pixel location in the orientation θ a maximum radius R_{max} or until it reaches the border of the image. In this work the radius is limited to 12.5 μm to accomodate cells up to 25 μm in size. Each ray can be thought of as placing a chip in a pixel bin. The number with the most bins represents the center of the approximated circle with radius R .

An example of a subset of a DIC image with mouse myeloma cell is shown in Figure 5.2. The output of the Hough transform is shown in Figure 5.3. Notice the located center of the circle is not ideal; however, it is sufficient to approximate the

boundary location. Also, the lack of rays emanating from the top right corner of the cell are caused by thresholded pixels from the DIC shadow effect during thresholding.

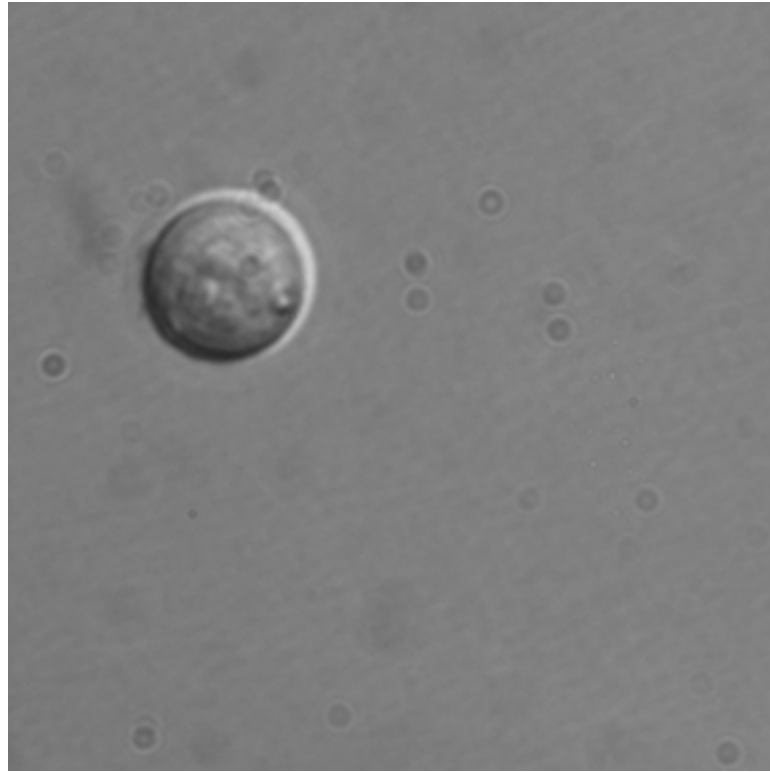


Figure 5.2: DIC image of mouse myeloma prior to the Hough transform

For comparison Figure 5.4(a) shows an ideal circle placed in the background of a DIC image. One can observe that the results are far less affected by noise.

This technique provided a suitable method of approximating the boundary in low noise and well spaced cell populations. The flexibility of the mechanical design of the system allowed the tip to be orientated in the direction of the maximum gradient of the DIC shadow existing in the middle of the pie shape boundary. The need to precisely locate the boundary was not necessary as the intent of the final stage of the approaching pipette was to monitor the increasing resistance at the electrode tip to detect suitable electroporation conditions.

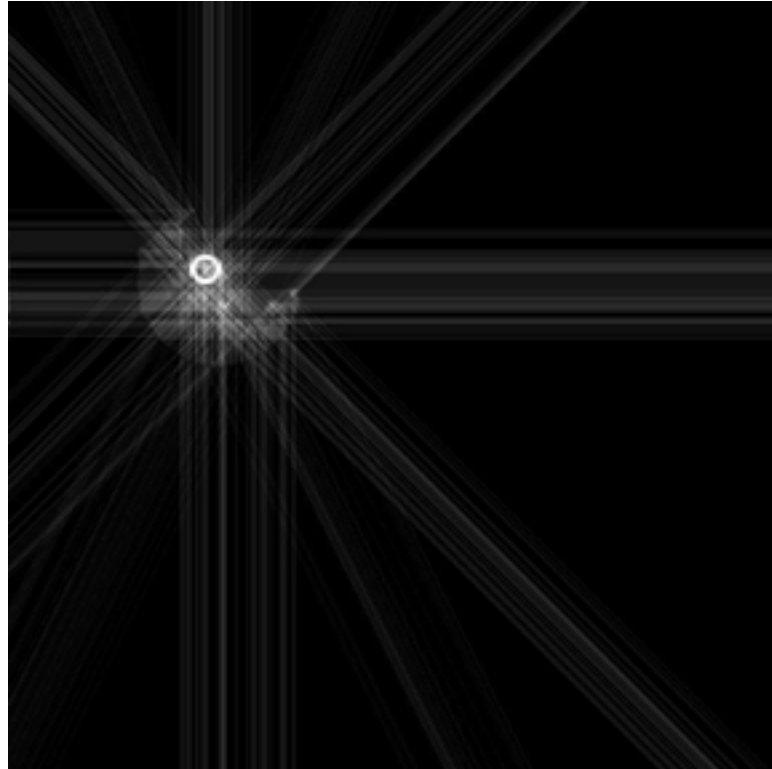
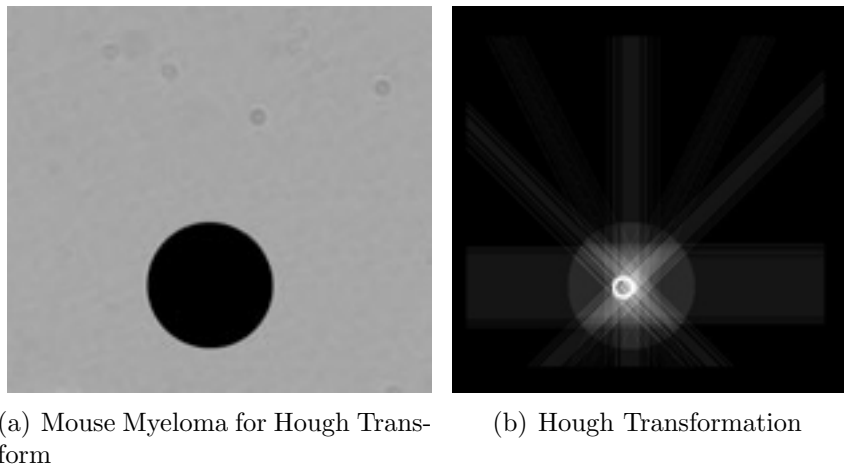


Figure 5.3: DIC Image of mouse myeloma after the Hough transform



(a) Mouse Myeloma for Hough Transform

(b) Hough Transformation

Figure 5.4: A perfect circle in place of the original myeloma cell (a), and the resulting Hough transformation output (b).

5.5.7 Autofocusing

Autofocusing will be accomplished using the normalized variance [71, 72] which is robust to noise and capable of operating after low-pass filter reducing the noise [18].

The normalized variance is defined in eq. (5.23),

$$NV = \frac{1}{\mu hw} \sum_u \sum_v (i(u, v) - \mu)^2 \quad (5.23)$$

where h and w are the height and width of the region, and μ is the average intensity of the region. Autofocusing works by examining the spatial frequencies in an image. Unfocused regions appear blurry and contain low spatial frequencies, whereas more focused areas have sharp edges and contain high-spatial frequencies.

5.5.8 Summary

This chapter has described the process in which the biomanipulator will be able to control the environment. The interface between the environment and the biomanipulator control is obtained through the computer vision processing of localized and segmented image features using techniques such as autofocusing by normalized variance, template matching, and morphological operators. The changes in image features are directly related through the image Jacobian to the changes in joint space coordinates. The weighted error function controls the value of the command sent to the joint-controller allowing the position to be obtained.

Chapter 6

Results

6.1 Overview

The experimental results demonstrate the completion of the five objectives set out in Chapter 1. These include: (i) accurately placing a micropipette tip near a cell membrane with minimal mechanical vibrations, (ii) developing a five degree-of-freedom biomanipulator capable of translating in \hat{x} , \hat{y} , and \hat{z} directions as well as varying the orientation of the micropipette tip about $\hat{\alpha}$ and $\hat{\beta}$ axes, (iii) implementing an optical system to image cells of 10 μm to 20 μm , (iv) implementing automatic control of the integrated mechanical and optical system, which must be capable of identifying a cell moving an end-effector to that target, and finally (v) injecting foreign material into cells by single-cell electroporation (SCE).

6.2 Mechanical Design

A 5 DOF biomanipulator, based on *Configuration 2* in Section 3.3, was designed and implemented. The biomanipulator was designed to minimize vibrations, provide smooth motion, and provide accurate position and velocity. Furthermore, the cantilever beam, in Section 3.6, which supported the Petri dish was designed to minimize deflection. It was not possible to quantify the structure's vibration characteristics or measure the deflection of the cantilever beam. However, countless hours of observed

stability, vibration free motion, and expected mechanical response confirms the success in developing the integrated mechanical system. In addition, visual confirmation of large multi-axis movements confirmed the required accuracy and repeatability.

6.3 Computer Vision

Localization of cells is the action by which the biomanipulator locates a cell in an acquired image. Localization is a prerequisite for the biomanipulator as it must record the location of the cell and move the cell to the end-effector for SCE. Three different computer vision algorithms were investigated for localizing mouse myeloma. The first two methods were based on the LOG and the Canny edge detector followed by thresholding and morphological operations. The second method, which was the most successful of the three, involved grey scale template matching and provided more information regarding a viable cell for electroporation.

6.3.1 Localization using Canny and LOG Algorithms

Initial attempts at localization were made using DIC illumination and the CMOS image sensor on dense cell populations. Exactly 173 unique images were obtained of the cells in unique locations of a 35 mm Petri-dish. The cells were immersed in a 10% Fetal bovine serum (FBS) in Dubelco's Modified Eagle's Medium (DMEM). Initially the Canny edge detector algorithms and the LOG algorithm were applied in attempt to localize the positions of the mouse myeloma. The success of Canny edge detector algorithm scored only 30.1% success in locating all the cells in the images, with a standard deviation of 20.2%. The Laplacian of a Gaussian scored 30.2% success with a standard deviation of 24.2%.

By performing a manual comparison of localization results, on all post-processed images, a common weakness of the vision algorithms was identified. Both the Canny edge detector and LOG based localization techniques were ineffective in localizing cells grouped in clusters. A subset of an image with clustered mouse myeloma cells is

shown in Figure 6.1(a). Gaussian smoothing was applied followed by the Laplacian, automatic thresholding, and finally morphological operators to the image of Figure 6.1(a). The resulting post-processed image is shown in Figure 6.1(b). The resulting image revealed membranes that appear to fuse together (highlighted white in Figure 6.1(b)). Ideally, individually separated shapes representing cells would allow more success in localization. The shadow effect caused by DIC optics, discussed in Section

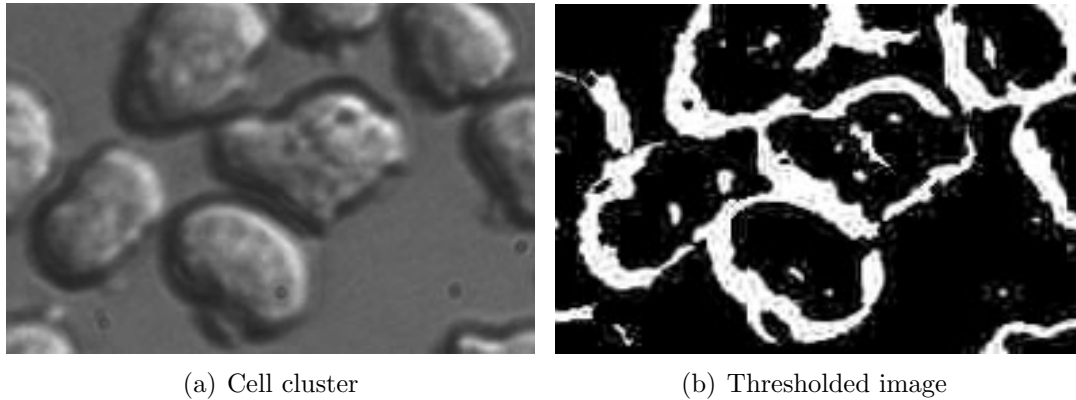


Figure 6.1: Image of a cell cluster images - cell cluster (left). Cell cluster after thresholding and morphology (right). This image is only a subset of the original image to highlight the merged borders after post-processing.

3.4.3, further disrupted localization abilities when using binary template matching. The similarity of intensities of the region where the DIC imaged cell perimeter and the background intensity are the same caused areas of the border of the cell to merge with the background upon thresholding as shown in Figures 6.2(a) and 6.2(b).

The use of morphological operators such as *close* and *dilate* to repair broken image edges was ineffective in providing a consistent shape for binary template matching. This again was primarily due to major disruptions in cell borders or borders of neighboring cells that appeared fused in the post-processed image.

Figures 6.3 and 6.4 display the ratio of located cells per image for both the LOG and Canny localization algorithms. This ratio represents the number of successfully located cells divided by the total number of cells per image. The average number of

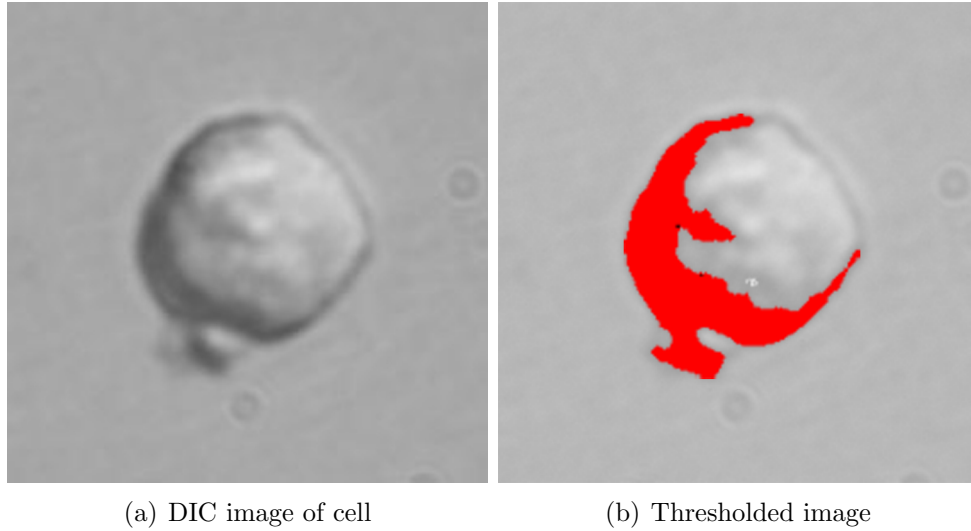


Figure 6.2: DIC image of mouse myeloma with the apparent shadow artifact(left). Thresholded image with the detected dark region highlighted in red (right).

total cells per image was 26.7 cells per image with a standard deviation of 8.77 cells. The similarity in the results between the LOG and Canny algorithms indicated that both algorithms failed in similar locations. Both algorithms achieved a higher ratio of successfully located cells where the cell density was low and the cells were sufficiently spaced apart. Similarly both algorithms failed where cell density was high and cells were packed tightly close together.

An additional problem with these methods that became more apparent to the author once more familiarized in cell characteristics, was in determining cell health. Cells that are less healthy are less likely to be successfully electroporated. Unhealthy cells should be rejected as candidates for SCE by the biomanipulator. The methods that convert greyscale images to binary images for fast processing reduce information regarding cell viability. In general, healthier mouse myeloma cells display several consistent visual features such as a spherical shape, and a smooth texture shown in Figure 6.5 (top-left). Less healthy cells can be deformed and often have a grainy texture as seen in Figure 6.5 (top-right). Figure 6.5 demonstrates the loss in viability information after several post-processing steps were done on the image. In Figure

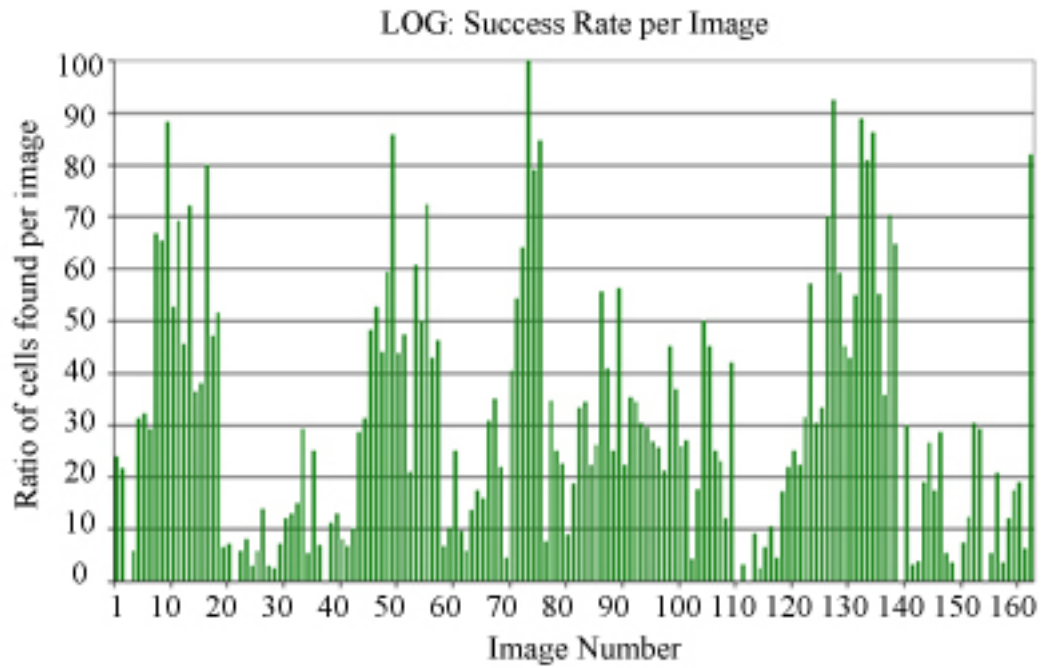


Figure 6.3: Ratio of success of the LOG algorithm after binary template matching

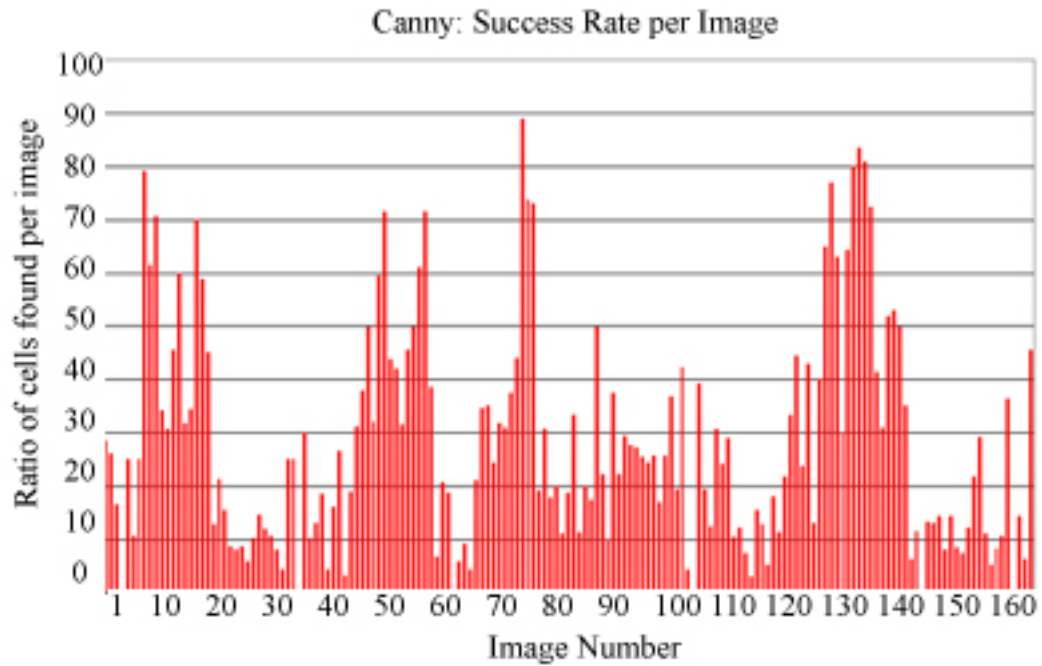


Figure 6.4: Ratio of success of the Canny algorithm after binary template matching

6.5 (middle), the LOG has been applied to the image which displays the detected edges. Figure 6.5 (bottom) concludes the post-processing after a *close* morphological operator was applied and a *fill* operation was done. It is less apparent, due to the lost texture, that the cells differ in appearance, and therefore may result in a unhealthy cell being falsely identified as a candidate for SCE.

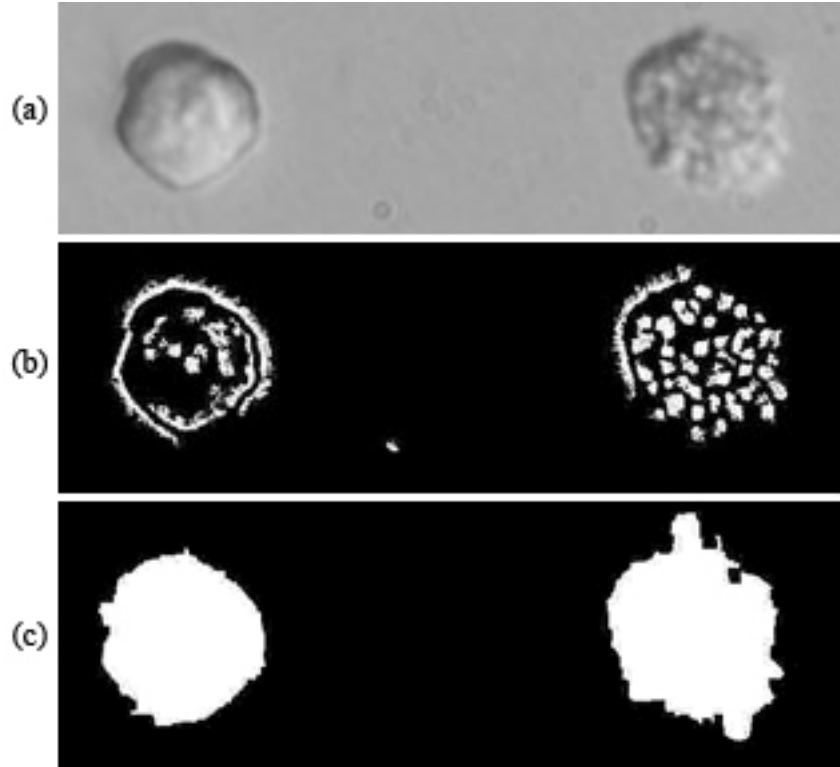


Figure 6.5: Cell viability in images

Due to these three issues, which are: *(i)* cell clusters cause shared borders, *(ii)* lost borders due to the DIC shadow artifact, and *(iii)* loss of cell viability information using binary information, modifications to operational protocols as well as post-processing algorithms were required.

In response to item *(i)*, the cell density was reduced and cells were adhered to the Petri-dish surface using 0.1% gelatin. Figure 6.6 illustrates a cell that is adhered to the Petri-dish. The cell will be slightly deformed if adhered correctly. The deformation of the adhered cell may vary but in general the shape can be thought of as

a partially deflated beach ball. This effectively reduced the number of cells within

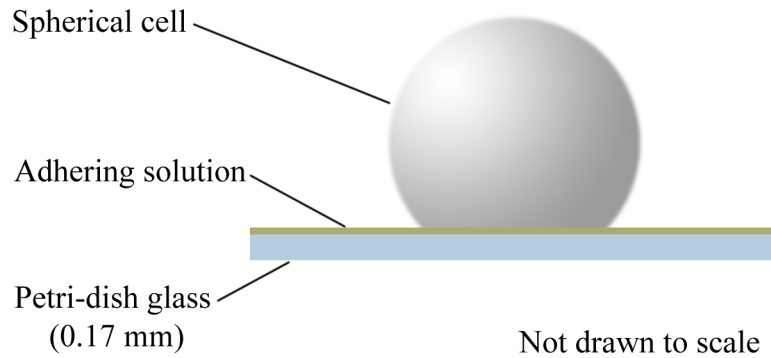


Figure 6.6: Adhered spherical cell

images and further provided benefits during the visual servoing of cells eliminating the need for a suction pipette. However, this method of adherence was not ideal. The cells did not adhere enough to allow the tip of the micropipette to indent the cells. After several trials, the 0.1% gelatin was replaced with poly-L-lysine (Sigma-Aldrich Stock No. P-8920). Poly-L-lysine provided a significant improvement in adhering the cells so that the cell could be significantly deformed (indented) by the micropipette tip. However, it was further discovered that cell viability decreases with the amount of poly-L-lysine used. Furthermore, increasing the amount of adhering chemical increases the noise detected by the image sensor. Other methods of non-toxic adherence are currently being explored, and are mentioned in Chapter 8.

To overcome items (ii) and (iii), greyscale template matching was selected. Template matching on greyscale images eliminated the need to threshold images, and eliminated subsequent morphological operators to correct for lost and merged cell boundaries. Information on cell health can be obtained by matching a hand-picked ideal image of a healthy cell to locate cells within the captured image. However, to decide whether a template match was successful in locating a desired cell that can be injected, a score based on eq. (5.19) was required. Furthermore, a threshold must be imposed such that the score of the located cell will either be classified as either

a suitable target or an unsuitable target. As discussed in Section 5.5.5, eq. (5.19) provides the ratio between the template and the area of the image the template is compared to, and is multiplied by 1000. To determine a reasonable estimate for a suitable score, 351 individual comparisons of imaged mouse myeloma cells were manually verified and scored using a standard image of a typical healthy cell shown in Figure 6.7. The number of healthy cells determined by visual inspection was 130 and number of less healthy and dead cells was 221. The cells in the image were sparse and no image had more than three cells per image due to a low cell density in the Petri dish.

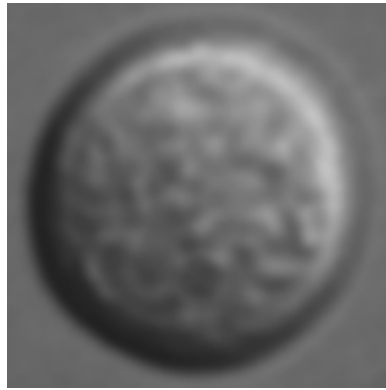


Figure 6.7: Greyscale mouse myeloma template image - The greyscale template of a typical healthy mouse myeloma cell used during greyscale template matching.

The standard mean score for a healthy cell was 670 with a standard deviation of 98, and the standard mean score for an unhealthy cell was 511 with a standard deviation of 84 which are shown in Figure 6.8. The threshold score used to locate all cells both healthy and unsuitable, was selected such that all cells greater than a score of the mean of the unsuitable cells minus two standard deviations could be identified (Score > 343). The purpose of identifying both desirable and undesirable targets is to allow future provisions to reduce collisions between the micropipette tip and the cells, as well as provide statistics on cell culture health.

Once the biomanipulator has determined that a cell is within the field-of-view it

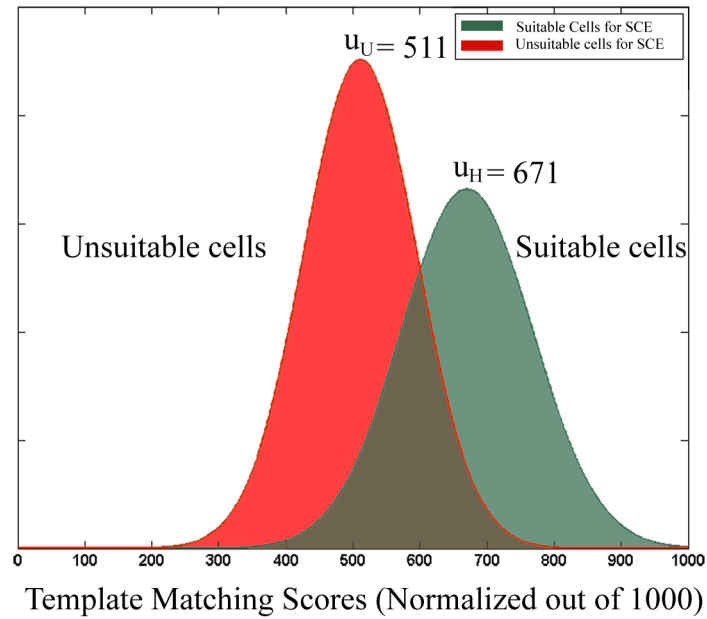


Figure 6.8: Normal distributions of all cells located by greyscale template matching

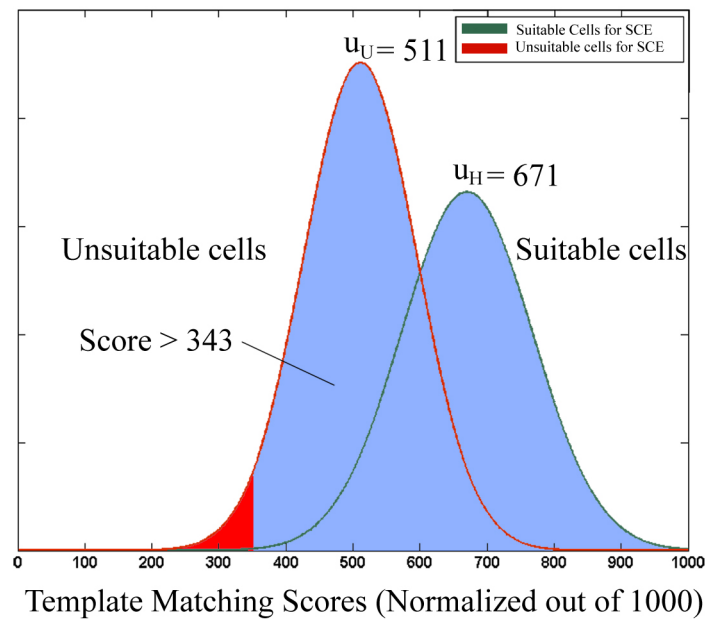


Figure 6.9: Healthy cells identified within image using a high threshold

then determine whether the score is higher than one standard deviation higher than the mean of the healthy cells (Score > 777) shown in Figure 87. If the score meets this

criteria then the cell is selected for SCE, otherwise the cell would be ignored and the biomanipulator will scan for another candidate cell for SCE. A second reason to avoid

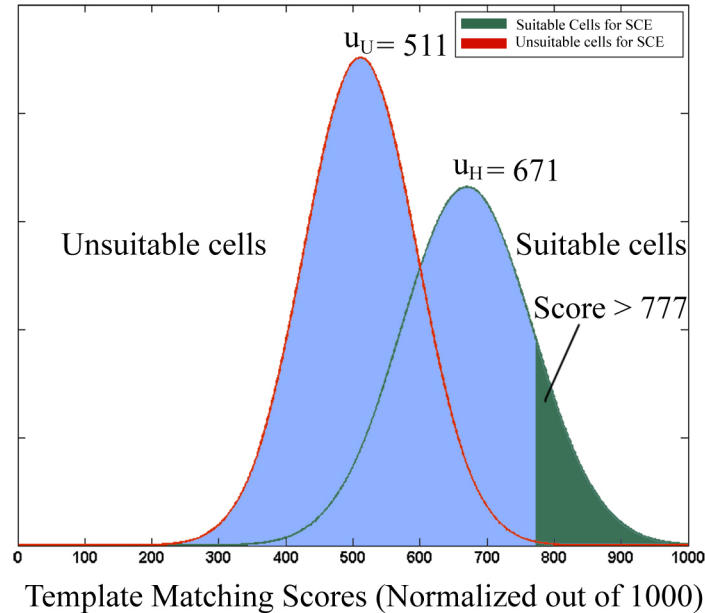


Figure 6.10: Cells identified within image using low threshold

the risk of incorrectly identifying a unhealthy cell and performing the microinjection operation on such a cell. Based on manual attempts at SCE, there is a high risk of halting the biomanipulator operation due to a clogged tip or fusing a membrane to the tip. Therefore, in development of the biomanipulator, the acceptable score for identifying a healthy or unhealthy cell is chosen as two standard deviations less than the standard mean of an unhealthy cell. Once an object has been detected within this region, if the score is larger than two standard deviations greater than the standard mean of all unhealthy cells it is classified as a suitable target.

Therefore, given the results and assuming the population density and cell health density is similar, the score required to successfully detect a healthy or unhealthy cell should be greater than or equal to a score of 343 out of 1000. Secondly, the score in determining whether located cell is suitable for SCE should be greater than or equal to 777 out of 1000. Using these scores, a 36.9% success rate of locating

the healthy cells exists, and less than 1.00% of unhealthy cells will be mistaken as healthy cells.

6.3.2 Segmentation

The Hough transform provided a suitable method of approximating the approximate boundary in a sufficiently spaced cell populations. The flexibility of the mechanical design of the system allowed the tip to be orientated in the direction of the maximum gradient of the DIC shadow existing in the middle of the pie shape boundary. The need to precisely locate the boundary was not necessary as the intent of the final stage of the approaching pipette was to monitor the increasing resistance at the electrode tip to detect suitable electroporation conditions.

6.4 Single-cell Electroporation

SCE is a mysterious, complex and difficult process to implement in practice, and consumed much more time than anticipated in this work. SCE was the intended method for the biomanipulator to delivering exogenous material into cells. This method was intended to provide rapid delivery and eliminate the need to penetrate the membrane, thereby reducing the risk of damaging or destroying the cell. Furthermore, single-cell electroporation has the additional advantage of providing proximity information regarding the location of the tip of the electrode with respect to the cell membrane, by measuring the changes in electric potential as the tip makes contact with the cell membrane.

The initial dye used for SCE injection was Alexa-Fluor 488 with a concentration of 300 μM . This dye is visible using the epi-fluorescence module on the inverted microscope. To verify that this dye would work with mouse myeloma the electroporation was first done using a standard bulk electroporator (Bio-rad Gene Pulser IITM). The settings of the standard electroporator are listed in Table 6.1.

Verification of successful bulk electroporation was confirmed using a CCD camera

Table 6.1: Settings for Bulk Electroporation

Setting	Value
Voltage	100 Volts
Modulation	50%
Frequency	30
Burst Time	4 seconds
No. of Bursts	5

(Hamamatsu Orca ERTM), DIC optics on a Leica microscope with a 40X, and a 0.75 NA Plan Apochromat objective. The electroporated cells were compared to a separate sample of myeloma that was placed within the 300 μ M fluorophore solution that was not electroporated. Within 5 minutes of viewing under the CCD camera, the successfully electroporated cell population was then viewed on the biomanipulator system using the CMOS Pixelink A741TM. However, similar indicators visible on the CCD system were not visible on the biomanipulator optical system. Further investigation revealed that the Alexa 488 fluorophore was not ideal for the CMOS camera whose quantum efficiency was less than half of the quantum efficiency of the CCD camera according to manufacturer specifications. Furthermore, the output spectrum of a mercury lamp is not optimal to excite Alexa 488 at 495 nm, the required excitation wavelength. Subsequently, the optical train had to be changed with different components. This was done with two changes. First, Alexa 568TM, a dye that emits in a region more suitable for the sensitivity of the CMOS sensor was chosen. Alexa 568TM was approximately 33% higher between 600 nm and 700 nm than where the Alexa 488 emits visible light (519 nm). Selecting Alexa Fluor 568TM which emits at 599 nm and is excited at 576 nm. The absorption wavelength, 576 nm, is also an area of elevated illumination from the mercury lamp. Thirdly, an appropriate filter block (ETS 49008, Chroma Technology Corp) was selected to match the excitation and emission bands for the fluorophore.

Using this improved optical train, the bulk electroporation was repeated on the

Bio-rad Gene Pulser II™ using the same parameters in Table 6.1. The electroporation was confirmed on the Leica microscope and the results were imaged with the CCD system shown in Figure 6.11. Within 5 minutes of this, the same electropo-

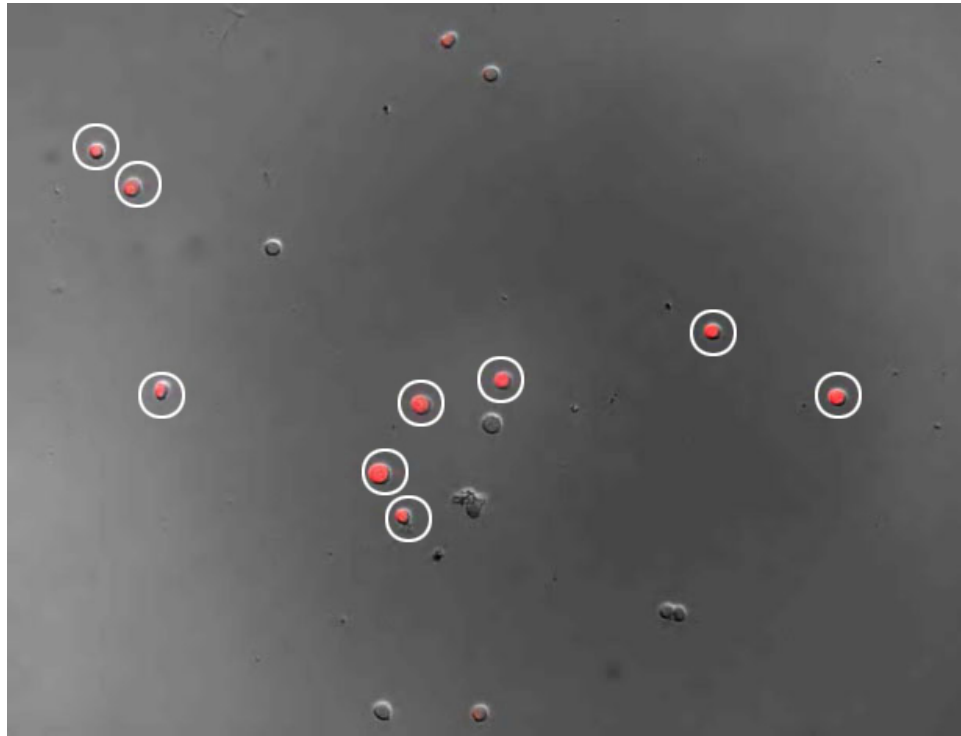


Figure 6.11: Bulk Electroporation of Mouse Myeloma using Alexa Fluor 568 - This is a regular DIC image overlaid by the image of the cells that were successfully bulk electroporated. The image overlay shows the fluorescing electroporated cells growing bright red, and are circled for clarity.

rated cells were again imaged by the biomanipulator and results of viewing the cells under epi-fluorescence illumination are shown in Figure 6.12. In contrast to viewing the fluorophore using the CCD camera, the intensity of the fluorophore diminished (bleached) almost completely within approximately five seconds of exposure to epi-fluorescent illumination.

A successful electroporation of mouse myeloma on the Bio-rad Gene Pulser II™, using Alexa Fluor 568™, demonstrated that the biomanipulator is capable of verifying cells that have been electroporated. The bleaching of the fluorophore occurs rapidly; however, is sufficient for manual verification of successfully electroporated cells.

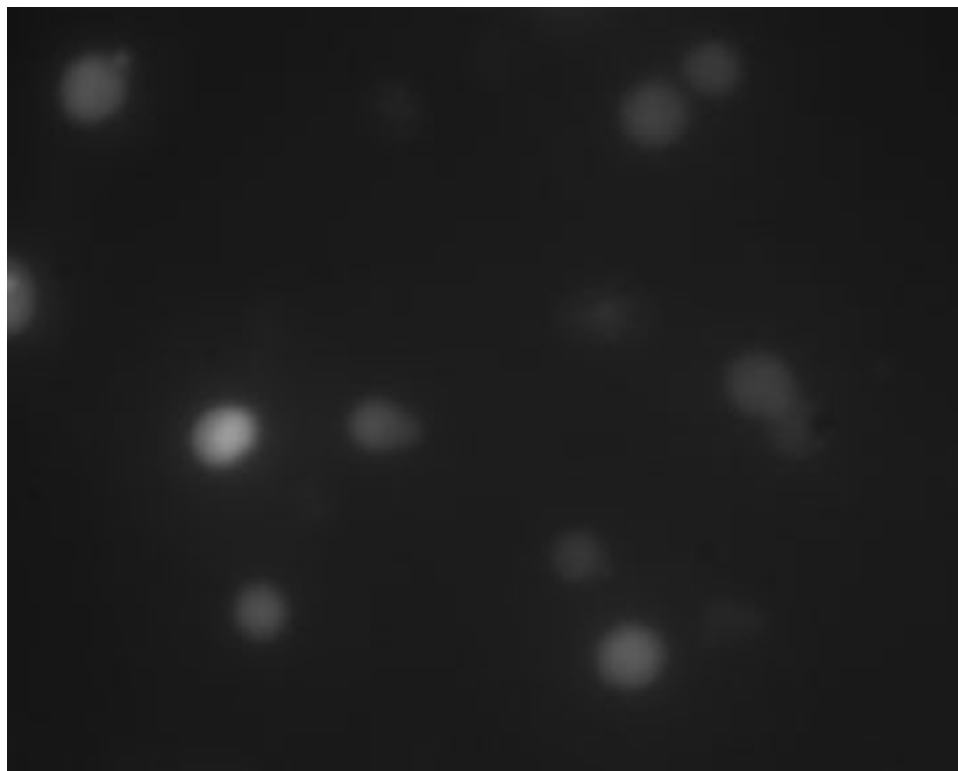


Figure 6.12: This image was captured by the biomanipulator. The fluorophore, Alexa Fluor 568TM, is optimized for mercury lamps and emits light in the sensitive region of the CMOS sensor.

Initial experimental trials of SCE were attempted manually in order to: verify that contact with the cell was being made, verify the cell membrane was being indented, and ensure the cell was healthy. The command voltage applied at the microelectrode was set to -4 V. This command voltage, theoretically, would result in approximately -1 V being delivered across the cell membrane once a 33% increase in cleft resistance was obtained. Other parameters that were based on successful SCE of myocytes by the manufacturer and successful SCE of bovine aortic endothelial cells [13]. These initial parameters include: pulse frequency set to 100 Hz, duty cycle set to 10%, and the initial duration of the pulse train was set to 3 seconds.

During manual experimentation to obtain successful SCE, the total electrode resistance was measured as 5.5 M Ω . Over 100 trials of SCE were attempted; however, no increase in cleft resistance was observed on the Axoprotor 800ATM. Measuring the increase in cleft resistance is a crucial interface between the task of bringing the cell near the micropipette tip and SCE itself.

Voltage, and pulse train duration parameters were modified; however, it was observed, that cells would not tolerate command voltages greater than -4.6 V in magnitude. It is the author's belief that some positive results may have been observed given a faint glow within the cell membrane. Due to rapid bleaching these results remain inconclusive.

It was determined that the current configuration of the biomanipulator requires some modification due to difficulties with cell adherence. This modification is discussed in Section 8, Future Work. Cells were initially adhered with 0.1% gelatin solution, but failed to adhere the cell in place while the micropipette tip was pressed against the membrane. The cell was pushed out of its original position and the 33% increase in cleft resistance was never obtained. This was a key requirement for the biomanipulator to determine when to activate the electric field pulses. Poly-L-lysine, a second adhering solution, was attempted and adhered the cells well, but was highly

toxic to the cells and the cells died within several minutes.

Chapter 7

Conclusions

It was the intention of the author to develop an autonomous biomanipulator with the following objectives: (i) accurately place a micropipette tip near a cell membrane with minimal mechanical vibrations, (ii) develop a five degree-of-freedom robot capable of translating in \hat{x} , \hat{y} , and \hat{z} directions as well as vary orientation of the micropipette tip about $\hat{\alpha}$ and $\hat{\beta}$, (iii) implement an optical system to image cells of 10 μm to 20 μm , (iv) control the integrated mechanical and optical system which must be capable of identifying a target and moving an end-effector to that target using closed-loop control, and finally (v) inject foreign material into cells by single-cell electroporation (SCE).

A high-precision, 5 DOF robot for biomanipulation was successfully constructed and tested in this work. The system makes use of the DIBLM classification of visual servoing, submicron resolution linear motors, and custom designed structural parts to minimize vibrations. With this system a micropipette was successfully automatically placed within five microns of a cell membrane. The 5 DOF biomanipulator provides three degrees-of-freedom of linear motion with submicron precision. This motion was unrestricted in a total of 16.5 mm in any direction and provided a manufacturer specified resolution of 40 nm allowing entire cell-cultures to be scanned. Furthermore, two rotation stages allowed varying injection angles to be achieved about $\hat{\alpha}$ in 360

degrees and $\hat{\beta}$ in about ± 45 degrees to either orientation about the vertical.

An inverted microscope configuration allowed for ample working space above the Petri dish to operate. A differential interference contrast objective with a numerical aperture of 0.70 and a theoretical resolution of 0.56 μm was used to observe mouse myeloma cells. The image was captured using a CMOS image sensor which provided a high frame-rate in comparison to a CCD image sensor with charge coupled device cameras. The CMOS image sensor also decreased computational latency by capturing a region-of-interest, by selectively activating only a window of pixels anywhere within the sensor pixel array.

Initially, there were difficulties in localization due to the shadow effect, a optical artifact of DIC, and clustered cells. Therefore it was determined that simple thresholding techniques are not suitable for localization and segmentation of mouse myeloma. When using thresholding, broken borders in imaged cells, caused by edges merging with similar background intensities, could not be rectified to using morphological operators. Furthermore, reducing the greyscale images to a binary image during post-processing reduces the ability of template matching algorithms to detect a healthy cell. However, the results of simple greyscale template matching on a large mouse myeloma population suggest that greyscale template matching is more effective and able to localize healthy mouse myeloma cells. To solve the clustering issue, limitations were imposed such that the biomanipulator would only operate on sufficiently separated cells that were adhered to the Petri dish. This further reduced difficulties with cell occlusion, but decreased the viability of cells due to the toxic nature of the adhering compound.

Visual servoing was successfully demonstrated by localizing mouse myeloma and using point features detected during template matching. These point features were compared during sequential images, and the observed change between the current and desired position defined the error term. The error was reduced using eq. (5.16)

which was used in a similar experiment carried out by [10] and developed by [34].

Single-cell electroporation of cells was not conclusively achieved during this work. Several variables exist complicating the matter, including material to deliver, cell health, electrode shape, and electric field signal characteristics. We confirmed that mouse myeloma can be successfully bulk electroporated, and confirmed by observing that both Alexa Fluor 488TM and Alexa Fluor 568TM. One of the requirements to achieve the successful electroporation of cells noted in literature was the increase in cleft resistance which occurs when pressing the tip of the micropipette against the cell membrane. The increase in surface tension increases the resistance as well as the potential drop across the membrane. The cleft resistance was not detected using the Axon Axoporation 800ATM, and successful single-cell electroporation was not observed. This measurement is required to complete the final stages in automating SCE, and without it other methods of determining close proximity between the tip and the cell membrane must be devised.

To conclude, good progress has been made toward a fully autonomous biomanipulator system in this work:

1. Given a set of ideal trajectory vectors to a cell, the robot can autonomously achieve the tip placement task,
2. The computer vision system is able to discern any object in the field-of-view and assign a score to determine the suitability for biomanipulation tasks,
3. Finding healthy *versus* less healthy cells is a difficult task. Based on experimental results approximately 37% of all healthy cells can be identified.
4. Autonomously visual servoing a cell to within approximately 5 μm of a micropipette tip and the cell membrane.

This biomanipulator will serve as the testbed for more development and future work in improved methods in single-cell electroporation, and enhanced template

matching/pattern recognition to improve the certainty of finding suitable cells for biomanipulation tasks. The development of the biomanipulator has provided the author with a wealth of knowledge in the areas of microbiology, computer vision, and robotics that were very new to the author. This will assist in further development and exploratory research (see Section 8).

Chapter 8

Future Research Proposed

Two emerging areas of science were explored in this work: automated visual localization and segmentation, and SCE of live cells. The ability to identify an object in a noisy, dynamic background, and non-deterministic environment is a difficult task. The difficulty of developing a generic algorithm to handle any particular situation makes computer vision a tedious and laborious task. It was demonstrated in this work that using simple greyscale template matching by correlation proved more effective than using functions to reduce the greyscale image to a binary one.

Currently, a significant amount of research is involved in methods using statistical pattern recognition to localize objects (*i.e.* cells) within a scene. It is the author's intention to research more sophisticated and more efficient methods of pattern recognition to increase the number of candidate cells for injection. Results from greyscale template matching techniques suggest that more complex methods may provide better results for localization.

SCE has the potential to provide a rapid method of inserting foreign material into a cell. Using SCE reduces the accuracy required by microinjection by micropipette, is less invasive to the cell, and reduces the need to use thin and fragile micropipette tips. SCE was unsuccessful in this work using the current configuration of the biomaniipulator. The need to measure a significant increase in cleft resistance provides two

key indicators: an activation point for the electric field pulses, and an indication of proximity between the membrane and the micropipette tip. Manual SCE of mouse myeloma, shown in Figure 8.1, was believed to be successful using a slightly different approach in one attempt. Instead of moving the cell membrane to the tip of the

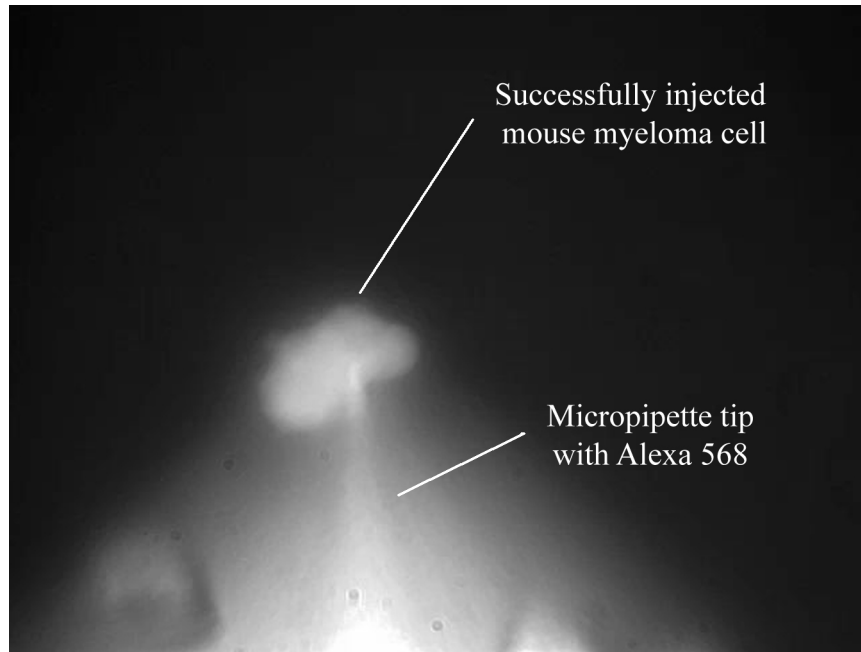


Figure 8.1: Successful SCE of mouse myeloma cells using Alexa Fluor 568™

micropipette using only horizontal motion, the micropipette tip was brought down onto the top of the cell membrane [13]. This involved manually changing the manual z -stage used to calibrate the micropipette tip. The micropipette tip was forced down onto the top of the cell membrane and an approximate 33% increase in cleft resistance was observed. This configuration would involve automating the z -stage holding the SCE. Furthermore, this involves some requirement to rely on positional encoder information and possibly reduced or elimination of visibility of the micropipette tip. However, pre-calibration of the micropipette tip would ensure that the tip would begin at the center of the image.

Bibliography

- [1] M. N. Teruel, T. A. Blanpied, K. Shen, G. J. Augustine, and T. Meyer. A versatile microporation technique for the transfection of cultured cns neurons. *Journal of Neuroscience Methods*, 1999.
- [2] R. L. Atkins and R. D. Burke D. Wang. Localized electroporation: A method for targeting expression of genes in avian embryos. *Biotechniques*, 2000.
- [3] K. Haas, W. C. Sin, A. Javaherian, Z. Li, and H. T. Cline. Single-cell electroporation for *in vivo* neuronal gene expression. *Neuron*, 2001.
- [4] D. Needham and R. H. Hochmuth. Electro-mechanical permeabilization of lipid vesicles. role of membrane tension and compressibility. *Biophysical Journal*, 1989.
- [5] J. Olofsson, K. Nolkrantz, F. Ryttsen, B. A. Lambie, S. G. Weber, and O. Orwar. Single-cell electroporation. *Current Opinion in Biotechnology*, 2003.
- [6] A. C. Sanderson and L. E. Weiss. Image-based visual servo control using relational graph error signals. In *Proceedings of the IEEE International Conference on Robotics and Automation*, pages 1074–1077, July 1980.
- [7] P. I. Corke. *Visual Control of Robots*, chapter Visual servoing, pages 151–170. Research Studies Press Ltd, 1996.
- [8] K. K. Tan and S. C. Ng. Computer-controlled piezo micromanipulation sys-

- tem for biomedical applications. *Journal of Engineering Science and Education*, December 2001.
- [9] F. Arai, K. Morishima, T. Kasugai, and T. Fukuda. Bio-micromanipulation (new direction for operation improvement). In *Proceedings of the 2002 IEEE/RSJ International Conference on Intelligent Robots and Systems*, pages 1766–1771, October 2002.
- [10] Y. Sun and B. J. Nelson. Biological cell injection using an autonomous micro-robotic system. *International Journal of Robotics Research*, October 2002.
- [11] S. Cho and J. Shim. A new micro biological cell injection system. In *Proceedings of 2004 IEEE International Conference on Intelligent Robots and Systems*, pages 1642–1647, September 2004.
- [12] M. Lukkari and P. Kallio. Multi-purpose impedance based measurement system to automate microinjection of adherent cells. In *Proceedings of the IEEE International Symposium on Computational Intelligence in Robotics and Automation*, pages 701–706, June 2005.
- [13] C. Bae and P. J. Butler. Automated single-cell electroporation. *Biotechniques*, October 2006.
- [14] D. Young and A. J. Gray. Template construction and matching for identification in differential interference contrast images. In *Proceedings of the IEEE 3rd Southwest Symposium on Image Analysis and Interpretation*, pages 238–243, 1998.
- [15] A. J. Gray. Detecting cells in dic microscope images using a high level bayesian model and template matching. In *IEEE Colloquium on Applied Statistical Pattern Recognition*, pages 238–243, July 2003.

- [16] P. A. Feineigle, A. P. Witkin, and V. L. Stonick. Processing of 3d dic microscopy images for data visualization. In *IEEE Conference on Acoustics, Speech, and Signal Processing*, pages 2160–2163, May 1996.
- [17] M. R. Arnison, C. J. Cogswell, N. I. Smith, P. W. Fekete, and K. G. Larkin. Using the hilbert transform for 3d visualization of differential interference contrast microscope images. *Journal of Microscopy*, July 2000.
- [18] Y. Sun, S. Duthaler, and B. J. Nelson. Autofocusing algorithm selection in computer microscopy. In *International Conference on Intelligent Robots and Systems*, pages 70–76, March 2005.
- [19] A. Karsson, N. C. Overgaard, and A. Heyden. Automatic segmentation of zona pellucida in hmc images of human embryos. In *Proceedings of the 17th International Conference on Pattern Recognition*, pages 518–521, August 2004.
- [20] F. Ambriz-Colin, M. Torres-Cisneros, J. G. Avina-Cervantes, and J. E. Saavedra-Martinez. Detection of biological cells in phase-contrast microscopy images. In *Proceedings of the Fifth Mexican International Conference on Artificial Intelligence*, pages 68–77, November 2006.
- [21] O. Debeir, P. Van Ham, R. Kiss, and C. Decaestecker. Tracking of migrating cells under phase-contrast video microscopy with combined mean-shift process. *IEEE Transactions on medical imaging*, June 2005.
- [22] F. Lamberti and B. Montrucchio. Tracking endothelial cells using multiframe point correspondance. In *Proceedings of the 28th IEEE International Conference on EMBS*, pages 1964–1967, August 2006.
- [23] S. P. Goff and P. Berg. Construction of hybrid viruses containing sv40 and lambda phage dna segments and their propagation in cultured monkey cells. *Cell*, December 1976.

- [24] J. C. Sanford, T. M. Klein, E. D. Wolf, and N. Allen. Delivery of substances into cells and tissues using a gene bombardment process. In *Journal of Particulate Science and Technology*, pages 27–37, January 1987.
- [25] R. S. Williams, S. A. Johnston, M. Riedy, M. J. DeVit, S. G. McElligott, and J. C. Sanford. Introduction of foreign genes into tissues of living micr by dna-coated microprojectiles. In *Proceedings of the National Academy of Sciences*, pages 2726–2730, April 1991.
- [26] J. Hill and W. T. Park. Real time control of a robot with a mobile camera. In *Proceedings of the 9th Intelligent Society for Intelligent Research*, pages 233–246, March 1979.
- [27] G. Hutchinson, P. I. Hager, and A. Corke. A tutorial on visual servo control. *IEEE Transactions on Robotics and Automation*, October 1996.
- [28] M. Ammi, H. Ladjal, and A. Ferreira. Evaluation of 3d pseudo-haptic rendering using vision for cell micromanipulation. In *Proceedings of the 2006 IEEE International Conference on Intelligent Robots and System*, pages 2115–2120, October 2006.
- [29] A. Pillarisetti, W. Anjum, J. P. Desai, G. Friedman, and A. R. Brooks. Force feedback interface for cell injection. In *Proceedings of the First Joint Eurohaptics Conference and Symposium on Haptic Interfaces for Virtual Environment and Teleoperator Systems*, pages 391–400, March 2005.
- [30] F. Arai, K. Morishima, T. Kasugai, and T. Fukuda. Bio-micromanipulation (new direction for operation improvement). In *Proceedings of the 1997 IEEE/RSJ International Conference on Intelligent Robots and System*, pages 1300–1305, 1997.

- [31] T. C. Lin, C. M. Jen, M. Y. Huang, C. Y. Wu, and X. Z. Lin. Electroporation microchips for continuous gene transfection. *Sensors and Actuators B*, 2001.
- [32] A. Sarkar, B. Mitra, A. Shastry, S. Wadia, R. Mulherkar, and R. Lal. A low voltage single cell electroporator with a microfabricated sense-porate aperture. In *17th IEEE International Conference on Micro Electro Mechanical Systems*, pages 375–378, 2004.
- [33] Y. Huang and B. Rubinsky. Flow-through micro-electroporation chip for high efficiency single-cell genetic manipulation. *Sensors and Actuators A*, 2003.
- [34] N. P. Panikolopoulos, B. J. Nelson, and A. Khosla. Full 3-d tracking using the controlled active vision paradigm. *IEEE International Symposium on Intelligent Control*, October 1992.
- [35] K. Nolkrantz et al. Electroporation of single cells and tissues with an electrolyte-filled capillary. *Analytical Chemistry*, 2001.
- [36] J. L. Rae and A. Levis. Single-cell electroporation. *Pflugers Archiv European Journal of Physiology*, 2002.
- [37] K. Kinoshita and T. Y. Tsong. Voltage induced conductance in human erythrocyte membranes. *Biochimica et Biophysica Acta*, 1979.
- [38] M. W. Davidson. Molecular expressions: Exploring the world of optics and microscopy. -, 2007.
- [39] A. J. Lacey. *Light microscopy in biology: a practical approach*, chapter The principles and aims of light microscopy, pages 1–59. Oxford University Press, 1989.
- [40] P. Healey. *Light microscopy in biology: a practical approach*. Grosset and Dunlap, 1970.

- [41] D. Young and A. J. Gray. Semi-automatic boundary detection for identification of cells in dic microscope images. In *Proceedings of the Sixth International Conference on Image Processing and its Applications*, pages 346–350, July 1997.
- [42] M. H. F. Wilkinson. *Digital Image Analysis of Microbes: Imaging, Fluorometry and Motility Techniques*, chapter Optical Systems for Image Analyzed Microscopy, pages 70–72. John Wiley and Sons, 1998.
- [43] F. Kagalwala and T. Kanade. Reconstruction of specimens using dic microscopes using dic microscope images. In *Proceedings of the 2000 IEEE International Symposium on Bio-informatics and Biomedical Engineering*, pages 307–315, November 2000.
- [44] C. Preza, D. L. Snyder, and J. Conchello. Image reconstruction for three-dimensional transmitted-light dic. In *Proceedings from SPIE on BiOS97; 3D Microscopy: Image Acquisition and Processing IV*, pages 2984–24, February 1997.
- [45] D. Littwiller. Ccd vs. cmos. *Photonics Spectra*, January 2001.
- [46] N. Blanc. Ccd versus cmos - has ccd imaging come to an end. *Photogrammetric Week 01*, 2001.
- [47] A. Basak and A. F. Flores Filho. Investigation of a novel double armature brushless d.c. linear motor: A dc linear motor with sectional armature winding. In *Conference Record of the 1995 IEEE Industry Applications Annual Meeting*, pages 789–795, October 1995.
- [48] R. C. Okonkwo and R. Hanitsch. Development and control of a prototype permanent-magnet dc linear motor. *IET Electric Power Applications*, March 2007.

- [49] Aerotech Incorporated, 101 Zeta Drive, Pittsburgh, PA, 15238, USA. *Aerotech Resource Guide*, 2007.
- [50] E. Neumann, S. Kakorin, and K. Tonsing. Fundamentals of electroporative delivery of drugs and genes. *Bioelectrochemistry and Bioenergetics*, January 1999.
- [51] G. Pucihar and J. Teiddi T. Kotnik. Electropermeabilization of dense cell suspensions. *European Biophysics Journals*, January 2007.
- [52] M. Glogauer and C. A. McCulloch. Introduction of large molecules into viable fibroblasts by electroporation: optimization of loading and identification of labeled cellular compartments. *Elsevier: Experimental Research*, 1992.
- [53] M. Okino and H. Mohri. Effects of high-voltage electrical impulse and an anticancer drug on in vivo growing tumors. *Japan Journal of Cancer Research*, December 1987.
- [54] A. Golthelf, L. M. Mir, and J. Gehl. Electrochemotherapy: results of cancer treatment using enhanced delivery of bleomycin by electroporation. *Cancer Treatment Reviews*, October 2003.
- [55] E. Neumann, M. S. Riddler, Y. Wang, and P. H. Hofschneider. Gene transfer into mouse lyoma cell by electroporation in high electric fields. *European Molecular Biology Organization Journal*, 1982.
- [56] K. Nolkrantz. Electro-permeabilization of cell membranes: effect of resting membrane potential. *European Molecular Biology Organization Journal*, 1990.
- [57] B. Valic et al. Effects of electric field induced transmembrane potential on spheroidal cells: theory and experiment. *European Journal of Biophysics*, 2007.

- [58] P. Ponsaerts et al. Messenger rna electroporation is highly efficient in mouse embryonic stem cells: successful flpe- and cre-mediated recombination. *Gene Therapy*, 2004.
- [59] M. Khine, A. Lau, J. Seo, and L. P. Lee. A single-cell electroporation device with integrated perfusion channels for efficient intracellular delivery. In *Proceedings of the 3rd annual IEEE Engineering in Medicine and Biology Society Special Topic Conference on Microtechnologies in Medicine and Biology*,, pages 225–228, May 2005.
- [60] S. Kakorin, E. Redeker, and E. Neumann. Electroporative deformation of salt filled lipid vesicles. *European Biophysics Journal*, 1998.
- [61] H. P. Schwan. Electrical properties of tissue and cell suspensions. *Advances in Biological and Medical Physics*, 1957.
- [62] E. Teckle, R. D. Astumian, and P. B. Chock. Electro-permeabilization of cell membranes: effect of resting membrane potential. *European Molecular Biology Organization Journal*, 1990.
- [63] J. Teissie B. Gabriel. Direct observation in the millisecond time range of fluorescent molecule asymmetrical interaction with the electropermeabilized cell membrane. *Biophysics Journal*, 1997.
- [64] J. A. Lundqvist, F. Sahlin, M. A. Aberg, A. Strmberg, P. S. Eriksson, and O. Orwar. Altering the biochemical state of individual cultured cells and organelles with ultramicroelectrodes. In *Proceedings of the National Academy of Sciences*, page 1035610360, 1998.
- [65] N. Otsu. A threshold selection method from gray-level histograms. *IEEE Transactions on Systems, Man, and Cybernetics*, 1979.

-
- [66] J. Canny. A computational approach to edge detection. *IEEE Transactions on Pattern Analysis and Machine Intelligence*, November 1986.
- [67] D. A. Forsyth and J. Ponce. *Computer Vision: A Modern Approach*, chapter Edge Detection, pages 165–188. Prentice Hall, 2003.
- [68] D. H. Ballard. Feature extraction and matching. In R. C. Fain R. Kasturi, editor, *Computer Vision: Principles*, chapter 3, pages 177–180. IEEE Computer Society Press, 1991.
- [69] R. O. Duda and P. E. Hart. Use of the hough transformation to detect lines and curves in pictures. *Communications for the Association for Computing Machinery*, January 1972.
- [70] D. H. Ballard. Generalizing the hough transform to detect arbitrary shapes. *Pattern Recognition*, 1981.
- [71] F. Groen, I. T. Young, and G. Ligthart. A comparison of different focus functions for use in autofocus algorithms. *Cytometry*, March 1984.
- [72] T. Yeo, S. O. Jayasooriah, and R. Sinniah. Autofocusing for tissue microscopy. *Computer Vision and Image Understanding*, 1993.

VITAAuthor Information

Surname: SAKAKI
Given Names: Kelly Dean Roy
Place of Birth: Merritt, British Columbia, Canada

Educational Institutions Attended:

Northern Alberta Institute of Technology 1999-2001
University of Victoria 2001-2008

Degrees Awarded:

Bachelor of Engineering University of Victoria 2005

University of Victoria

Partial Copyright License

I hereby grant the right to lend my thesis to users of the University of Victoria Library, and to make single copies only for such users or in response to a request from the Library of any other university, or similar institution, on its behalf or for one of its users. I further agree that permission for extensive copying of this thesis for scholarly purposes may be granted by me or a member of the University designated by me. It is understood that copying or publication of this thesis for financial gain shall not be allowed without my written permission.

Title of Thesis: Development of a Five Degree-of-Freedom Robot for the Manipulation of Biological Cells.

Author: _____

Kelly D. R. Sakaki

August 28, 2007